Studies on structured model nanoparticle surfaces for active site elucidation in heterogeneous catalysis

Thesis Submitted to AcSIR

For the award of the

Degree of Doctor of Philosophy

in

Chemical Sciences

By

Sreedhala S

AcSIR No. 10CC11A26026

Under the guidance of

Dr. Vinod. C. Prabhakaran

CSIR-National Chemical Laboratory,

Pune-411008

August 2016

CERTIFICATE

This is to certify that the thesis entitled *"Studies on structured model nanoparticle surfaces for the active site elucidation in heterogeneous catalysis"* submitted by *Sreedhala S*, for the degree of *Doctor of Philosophy* in *Chemical Sciences* to the Academy of Scientific and Innovative Research (AcSIR), New Delhi was carried out under my supervision at Catalysis and Inorganic Chemistry Division, CSIR-National Chemical Laboratory, Pune, India. Such material obtained from other sources has been duly acknowledged in the thesis.

Date:

Place**:**

Dr. Vinod. C. Prabhakaran

Research Guide

‘

DECLARATION

I hereby declare that the work described in the thesis entitled *"Studies on structured model nanoparticle surfaces for active site elucidation in heterogeneous catalysis"* submitted for the degree of *Doctor of Philosophy* in *Chemical Sciences* to the Academy of Scientific and Innovative Research (AcSIR), New Delhi, has been carried out by me at the Catalysis and Inorganic Chemistry Division, CSIR-National Chemical Laboratory, Pune–411008, India under the supervision of **Dr. Vinod. C. Prabhakaran.** I further declare that the material obtained from other sources has been duly acknowledged in this thesis. The work is original and has not been submitted in part or full by me for any other degree or diploma to this or any other university.

Date:

Place:

Sreedhala S

Research Scholar

Acknowledgements

Dedicated to my parents

Table of contents

List of Figures

List of tables

List of schemes

List of Abbreviations

SEM - Scanning Electron Microscopy

TEM - Transmission Electron Microscopy

XRD - X-ray Diffraction

ICP - Inductively coupled Plasma

DLS - Dynamic Light Scattering

MB - Molecular Beam

GC - Gas chromatography

FID - Flame Ionisation Detector

UV-Vis - Ultraviolet-Visible spectroscopy

FT-IR - Fourier Transform Infrared Spectroscopy

BET - Brauner Emmet teller

TOF - Turn Over Frequency

hcp - Hexagonally Closed Packed

fcc - Face Centered Cubic

bcc – Body Centered Cubic

THH - Tetrahexahedron

TPH - Trapezohedron

TOH - Trisoctahedron

HOH - Hexoctahedron

T_{50} - Temperature of 50% conversion

T_{100} - Temperature of 100% conversion

DFT - Density Functional Theory

WGSR - Water Gas Shift Reaction

TCD- Thermal Conductivity detector

JCPDS- Joint council for Powder Diffraction Studies

TOS- Time on stream

CNC- Concave nanocube

PROX- Preferential oxidation

PEMFC- Proton exchange membrane fuel cells

SERS- Surface Enhanced Raman Spectroscopy

PVP- Poly vinyl pyrrolidone

BEP- Bronsted Evans Polanyi

SPR- Surface Plasmon Resonance

Chapter- 1

Introduction

1.1. Catalysis

A **catalyst** is a substance which accelerates the rate of the chemical reaction by providing lower activation barrier for the reactants to form products. The energy profile diagram showing a reaction going through catalytic and non-catalytic route is shown in Figure 1.1a. The concept of *catalysis* has a long history and one of the early document on this concept was published by Jons Jacob Berzelius as early as 1835.[1] This report reviewed a number of earlier findings on chemical change in both heterogeneous and homogeneous systems. The area of catalysis can be broadly classified into homogeneous and heterogeneous depending on the phase of reactants and catalyst. In homogeneous catalysis both the reactants and catalyst are in same phase and it provides an easy and facile interaction between the molecules. However, a major drawback involves the isolation of products from the homogeneous medium and hence the recyclability. The reaction between persulphate ions and iodide ions in water by Fe(II) or Fe(III) ions is an example for homogeneous catalysis system.[2] The complete recovery can be achieved by the heterogeneous catalyst route where the catalyst is usually metal or metal oxide nanoparticles dispersed on high surface area support and the reactants can be either in liquid, in gas phase, or both. The hydrogenation of carbon-carbon double bond over Ni catalyst,[3] Haber process for the synthesis of ammonia,[4] contact process[5] etc are few examples for industrially important reactions which are carried through heterogeneous catalysis route. Since all the reactions studied in the thesis goes through heterogeneous route, unless otherwise mentioned "catalysis" means heterogeneous catalysis throughout the thesis.

The main catalytic steps includes adsorption and diffusion of reactants, chemical changes involving formation of adsorbed complex, decomposition of adsorbed complex and desorption of products. A conceptual framework about the idea of a optimum catalyst can be explained by **Sabatier Principle.**[6] It states that the best catalyst should bind molecules with an intermediate strength, neither too strong nor too weak to activate the reactants and for easy desorption of the products. This leads to volcano type relationship between activity and bond strength as shown in Figure 1.1b.[7]
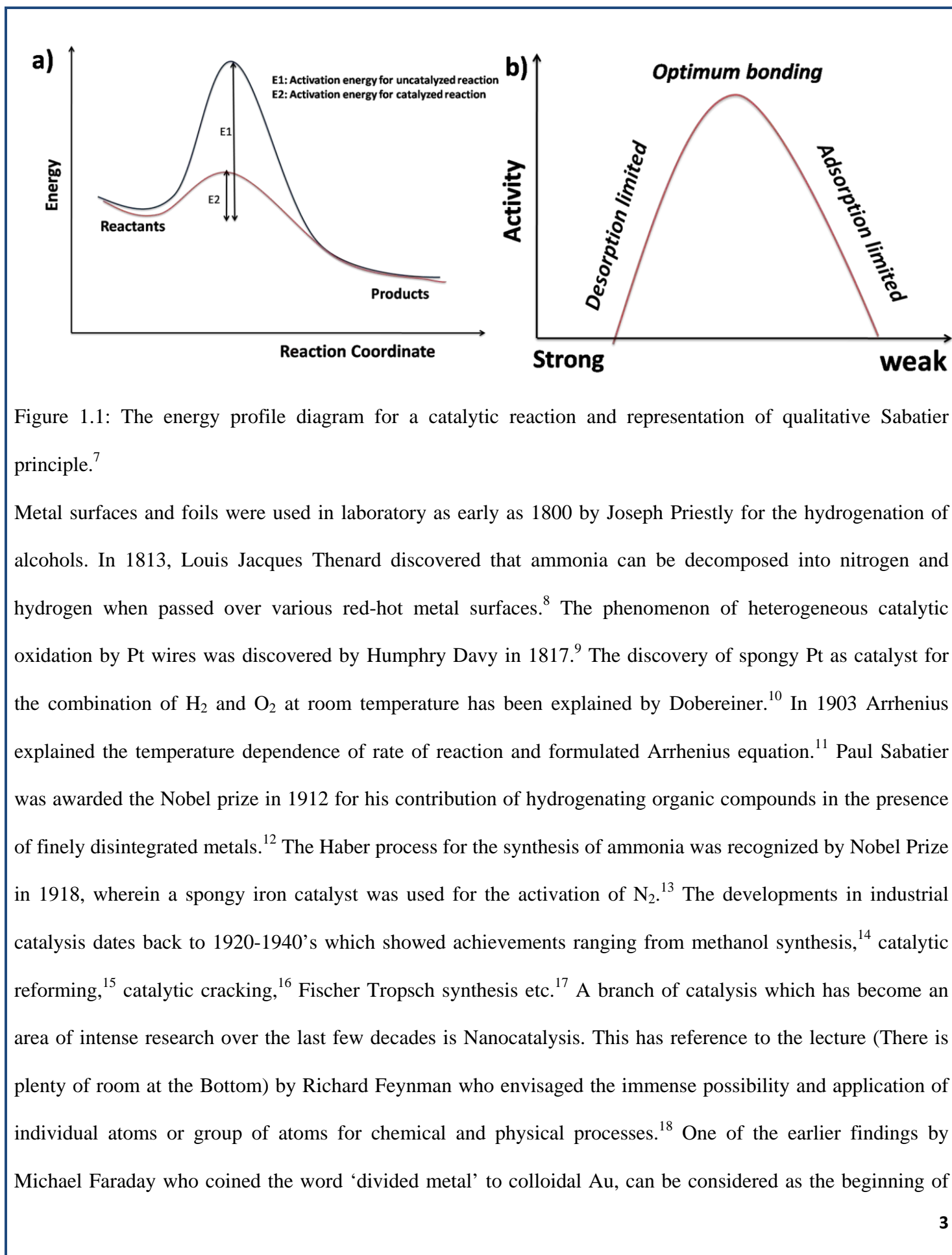
Figure 1.1: The energy profile diagram for a catalytic reaction and representation of qualitative Sabatier principle.[7]

Metal surfaces and foils were used in laboratory as early as 1800 by Joseph Priestly for the hydrogenation of alcohols. In 1813, Louis Jacques Thenard discovered that ammonia can be decomposed into nitrogen and hydrogen when passed over various red-hot metal surfaces.[8] The phenomenon of heterogeneous catalytic oxidation by Pt wires was discovered by Humphry Davy in 1817.[9] The discovery of spongy Pt as catalyst for the combination of H_2 and O_2 at room temperature has been explained by Dobereiner.[10] In 1903 Arrhenius explained the temperature dependence of rate of reaction and formulated Arrhenius equation.[11] Paul Sabatier was awarded the Nobel prize in 1912 for his contribution of hydrogenating organic compounds in the presence of finely disintegrated metals.[12] The Haber process for the synthesis of ammonia was recognized by Nobel Prize in 1918, wherein a spongy iron catalyst was used for the activation of N_2.[13] The developments in industrial catalysis dates back to 1920-1940's which showed achievements ranging from methanol synthesis,[14] catalytic reforming,[15] catalytic cracking,[16] Fischer Tropsch synthesis etc.[17] A branch of catalysis which has become an area of intense research over the last few decades is Nanocatalysis. This has reference to the lecture (There is plenty of room at the Bottom) by Richard Feynman who envisaged the immense possibility and application of individual atoms or group of atoms for chemical and physical processes.[18] One of the earlier findings by Michael Faraday who coined the word 'divided metal' to colloidal Au, can be considered as the beginning of

the area of nanoscience.[19] Nanoparticles derived from the bulk metals, are found to be potential heterogeneous catalysts for several chemical reactions.[20-21] As one moves from bulk to nanoscale, two basic size dependent effects can be observed. A smoothly scalable ones which depends on fraction of atoms on the surface and quantum size effect which is non scalable.[22]

Surface effects induced by fraction of atoms on the surface

Atoms at the surface have lesser number of nearest neighbors as compared to the atom in the bulk. Particles with large number of surface atoms have low mean coordination number. Fraction of atoms at the surface is called dispersion and it scales with surface area to volume ratio i.e. with inverse of radius and also with $N^{-1/3}$ as shown in Figure 1.2a.[23] Atoms at the surface are less stable and this leads to better chemical activity as they bind with adsorbate molecules to minimize their surface energy. For a cubic crystal degree of unsaturation follows the order corner sites > edge > in plane surface atoms > bulk atoms. This means that the activity trend follows the reverse order. Similarly, the lower stability of the surface atom can show interesting physical properties like lowering of melting point of a system. For instance, the melting point of a 2.5 nm Au nanoparticle is found to be 930 K which is much lower than its bulk value of 1336 K.[24]

Quantum size effects

Atoms have atomic orbitals and they overlap to form extended band structures in case of metals and semiconductors. It is known that one electron energy level of atoms splits into two levels when a dimeric molecule is formed from these atoms. So with the increase in the number of atoms in a cluster, energy levels split and merge into a continuous band structure as in bulk. But in case of smaller particles electronic states are not continuous but discrete due to the confinement of electron wave function. Average spacing of such successive quantum levels is called Kubo gap, $a = 4E_f/3N$, where E_f is the Fermi energy of the bulk, N is the No. of atoms in the cluster. The energy level spacing varies inversely with the no. of atoms in the cluster. As we move from bulk to atomic level, Kubo gap goes from smaller to larger values. As the Kubo gap increases, there will be decrease in the density of states at the Fermi level.[25] This results in a shift in the conductive properties

4

from metallic to semiconducting to insulating with decreasing size (as shown in Figure 1.2b) which is a manifestation of electronic structure modification as we move from bulk to nanoregime.[26]
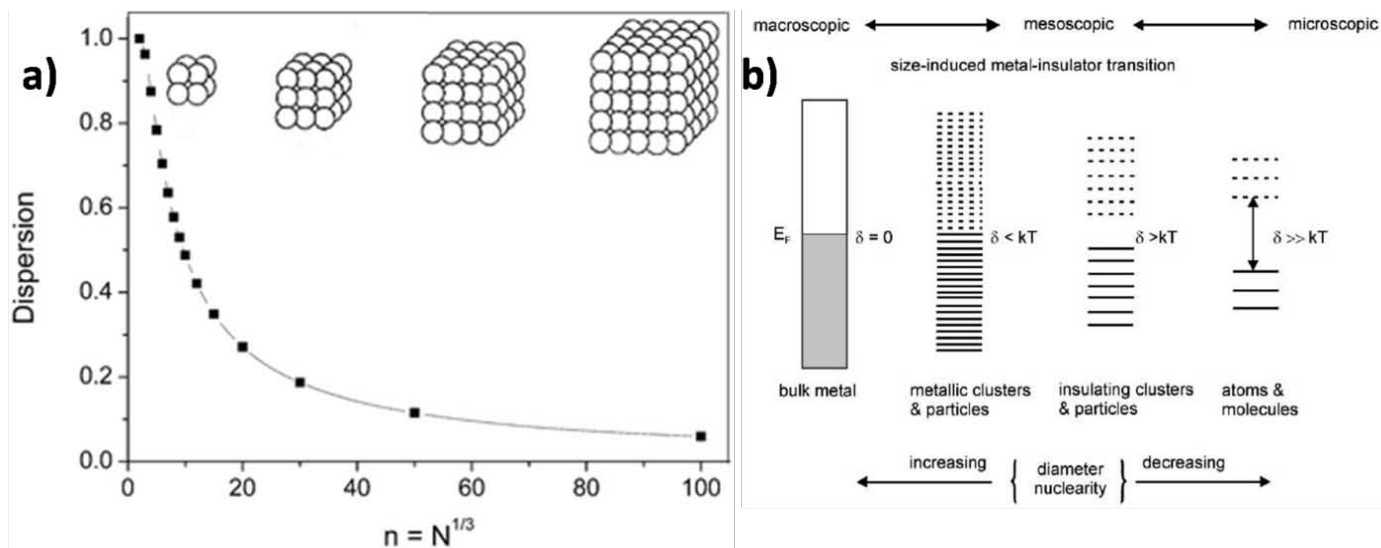
Figure 1.2: Schematic representation of change in surface to volume ratio of a nanoparticle with size and change in the electronic structure of a bulk metal with size.[23,25]

1.2. Structure dependent chemical reactivity

The emerging field of nanoscience has paved a way to investigate the properties that depend on particle size and shape. One of the important properties that depend on size is the chemical reactivity in which bonds are broken or formed on the surface of nanoparticles. Decreased particle size may increase, decrease or have no effect on the reaction rates. Boudart was the one to classify the reactions as structure sensitive and insensitive reactions.[27] In this report, he describes structure sensitive reactions as demanding reactions and insensitive ones as facile reactions. A facile reaction can be defined as one for which the specific activity is independent of the surface structure. The activity per metal atom towards hydrogenation of benzene on metals like Pt, Pd, Ni supported on silica, silica-alumina, silica magnesia were found to be independent of metal dispersion and support used.[28] Demanding reactions are those which depend on surface structure. van Santen has recently reviewed molecular level description for three classes of structure sensitivity.[29] In the particle size regime between 2 nm and 20 nm three types of reactivity can be distinguished as shown in Figure 1.3.[30] The rate of some reaction is found to increase with decrease in particle size, some are independent of particle size, and

some decreases with decrease in size. The nature of the substrate bond activated determines which surface atom rearrangement provides the lowest activation barrier. Class I structure sensitivity behavior occurs for reactions where rate limiting step involves the formation or dissociation of π type bond. Ex: dissociation of CO or N_2. The activation of σ bond such as CH bonds in methane falls in class II category which shows a uniform increase in reaction rate with decreasing particle size. The reverse reaction of adsorbed hydrogen recombining with adsorbed alkyl is independent of particle size and shows class III structure sensitivity behavior.
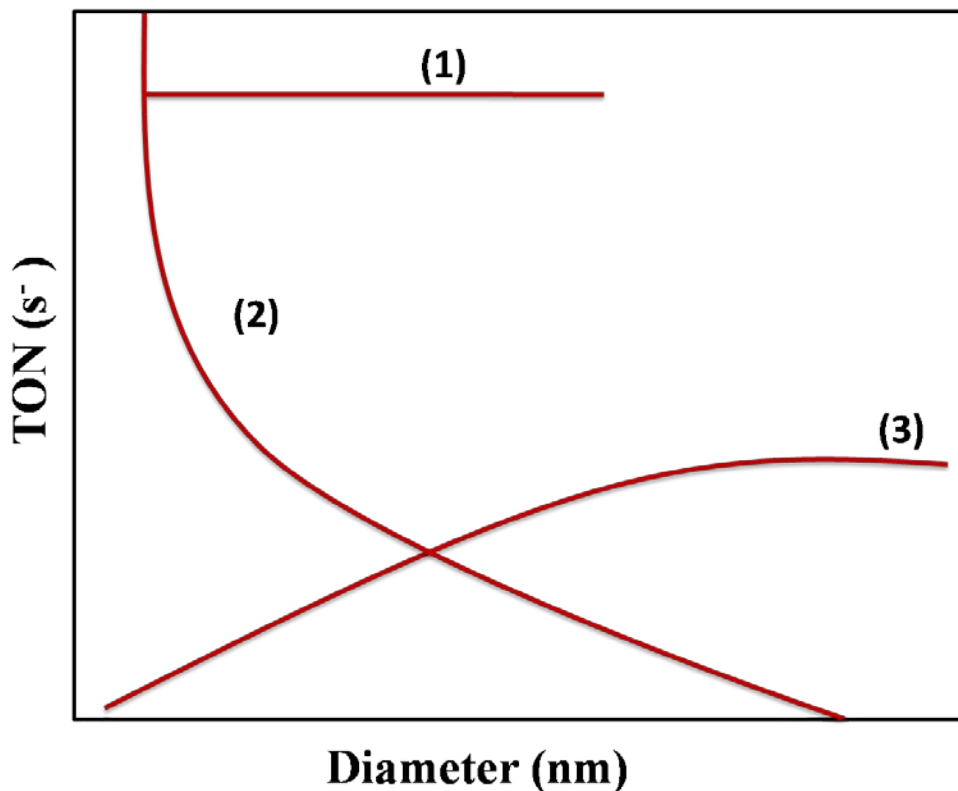
Figure 1.3: The three different kinds of structure sensitivity-particle size relationship plotted as turnover number for selected reactions versus particle size.[30]

The investigation of structure dependency have led to several surface science single crystal studies notably by Somorjai[31] and Yates.[32] With the advent of scanning probe microscopes, Ertl and coworkers demonstrated the first direct STM visualization of the active sites for the dissociation of NO over atomically resolved Ruthenium surfaces.[33] The distribution of N_2 atoms after the dissociation helped for the identification of active sites which are low coordinated top metal atom on step sites. The activity of step atoms is proposed to

be due to the change in local electronic structure.[33] Up to recent years, a majority of structure-activity correlation studies were made through model surface science studies where high end surface science tools were employed to look at single crystal surfaces or thin film metal nanoparticle/metal oxide thin film surfaces.[34-35] The advances made in the synthesis have helped to tune the size and shape of the nanoparticles.[36-37] The size dependent catalytic activity can be due to the geometrical and electronic modification that occurs on particles in nanosize regime which alter the way the reactants gets activated. The enhanced activity can be also attributed to the arrangement of atoms on the exposed facet. One way to change the surface structure is to change the particle size and in nanocatalysis, Haruta et al reported in their classic papers which described the size effect in catalysis by gold.[38] They proved that gold (Au) which is inert in the bulk form, were found to be active for CO oxidation when finely divided into small particles below 5 nm. The presence of under coordinated atoms, change in the electronic structure (metal to non-metal transition),[39] metal-support interaction[40] can be attributed reasons for this enhanced activity in "nano" regime.

Apart from size, the particle morphology is also found to influence the catalytic behavior. The adsorption and desorption of molecules is strongly dependent on the crystallographic facets.[41] If the activity or selectivity is tuned by the facet exposed then such reactions are termed facet dependent reactions.

1.3. Surface structure

Catalytically important transition metals falls in face centered cubic (fcc), body centered cubic (bcc) or hexagonally closed packed (hcp) crystal structures. A nanoparticle surface commonly exposes low index facets like {100}, {111} or {110} to minimize the surface energies (see Figure 1.4). These facets differ in their co-ordination number. For example on a {100} plane, each atom is surrounded by 8 other atoms, and for a {111} facet the co-ordination number is 9 and 7 for a {110} plane. The most stable surface is {111} and {110} is a more open surface. These surfaces provide different adsorption sites for molecules viz on top sites, bridging sites and hollow sites and are low energy surfaces. The class of high energy surfaces is termed high index

faceted structures. They are vicinal surfaces consisting of terraces separated by atomic step. For example {331} surface is found to be composed of 2 atom wide {111} terrace followed by {110} monoatomic step.[42]
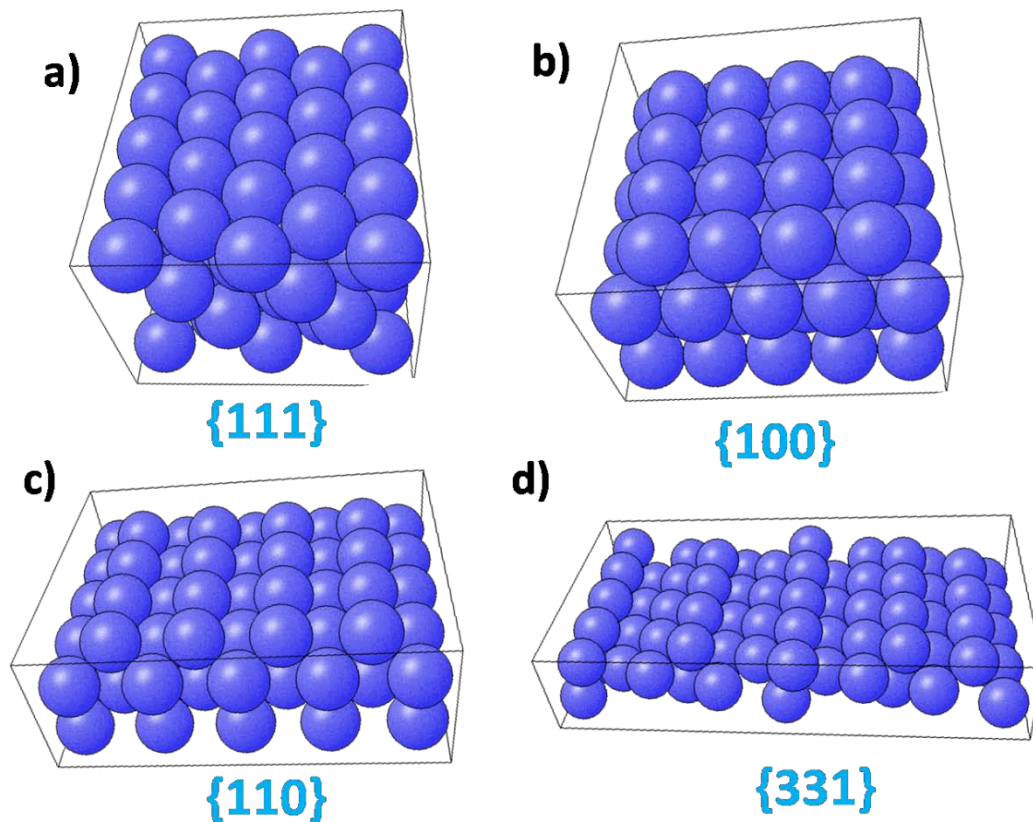
Figure 1.4: The figure showing the atomic model for different facets for a fcc metal (generated by Surface Explorer *www .surfexp.fhi-berlin.mpg.de*)

El-sayed and coworkers were one of the first groups to show shape dependent chemical activity on Pt nanoparticles.[43] They were successful in synthesizing Pt cubes, spheres and tetrahedras and showed the electron transfer reaction between thiosuphate and hexacyanoferrate to be facet dependent. They observed that Pt tetrahedrons were found to show highest activity when compared to Pt cubes and the activity was co-related to the fraction of surface atoms exposed on the corners and edges of the Pt nanoparticles. In another report, Somorjai and coworkers found that the hydrogenation of benzene over Pt nanoparticles was morphology dependent.[44] They concluded that cyclohexane was the only product in case of Pt nanocubes while both

cyclohexene and cyclohexane were formed on a cubooctahedron which exposes both {100} and {111} facets.[44] The selective hydrogenation of α,β unsaturated aldehydes on supported Pt catalysts was found to be facet dependent. For instance, the selective hydrogenation of crotonaldehyde to crotyl alcohol is achieved on Pt nanoparticles of larger size (2.3-17 nm) than smaller ones (1.8 nm).[45] The larger fraction of {111} facets on a bigger Pt nanoparticle is concluded to favor the adsorption of crotonaldehyde via carbonyl bond favoring its hydrogenation. But on the surface of smaller nanoparticle both unsaturated bonds (C=O and C=C) get activated owing to the presence of under coordinated sites leading to complete hydrogenation. Similar structure dependence was also observed for the hydrogenation of 2-butyne-2,4-diol, styrene epoxide,[46] 2-methyl-3-buten-2-ol,[47] and nitrobenzene[48] by Pd nanoparticles. Tetrahedral Rhodium nanoparticles which exposes {111} planes were found to selectively hydrogenate anthracene to the desired product.[49] In the hydrogenation of aromatic nitrocompounds to amines, the activity of Au nanoparticles followed the order nanospheres > nanoprisms > nanorods.[50] It is also reported that the epoxidation of ethylene and styrene on silver nanoparticles is structure sensitive.[51-52] Ru[53-54] and Co[55] catalysed reactions are also found to be morphology dependent. Such model nanoparticle surfaces can bridge the gap between single crystal surfaces and real world catalyst and can be potential candidates for validating the hypothesis of active sites in heterogeneous catalysis.

1.4. Structure Sensitivity: Theoretical Background

Bronsted Evans Polanyi (BEP) relations

A supported metal nanoparticle in a high surface area catalyst exposes different atoms with different local geometries viz planes, edges, corners, steps, kinks etc. These sites are independent of each other in their activity.[56] The nature of active sites and catalytic activity has been debated in the literature.[27,29,33,57-61] The surface structure is found to affect the reactivity in two ways.

   I.   Geometric

  II.   Electronic

Surface metal atoms in different environments will have different electronic structures (d-band center) and they interact differently with the adsorbate molecules.[62-64] For instance late transition elements tend to have a high lying d-band center and they are found to interact strongly with the molecules. Similarly different surface geometries can provide different atomic configuration to the molecule for bonding and this can be the geometrical effect. For example, a step atom has higher lying d-states as well as new surface atom configuration (low coordination) which can result in interaction with reactant molecules and thereby exhibits a different reactivity. To probe which is the exact factor whether geometric or electronic a linear relationship between activation energy and reaction energy called Bronsted Evans Polanyi lines have been theoretically formulated.[65] To explain this, activation energies of surface reactions are often found to be roughly linear to the reaction energies. For instance, BEP plot for dissociation of methane and N_2 is shown in Figure 1.5.[66-67]
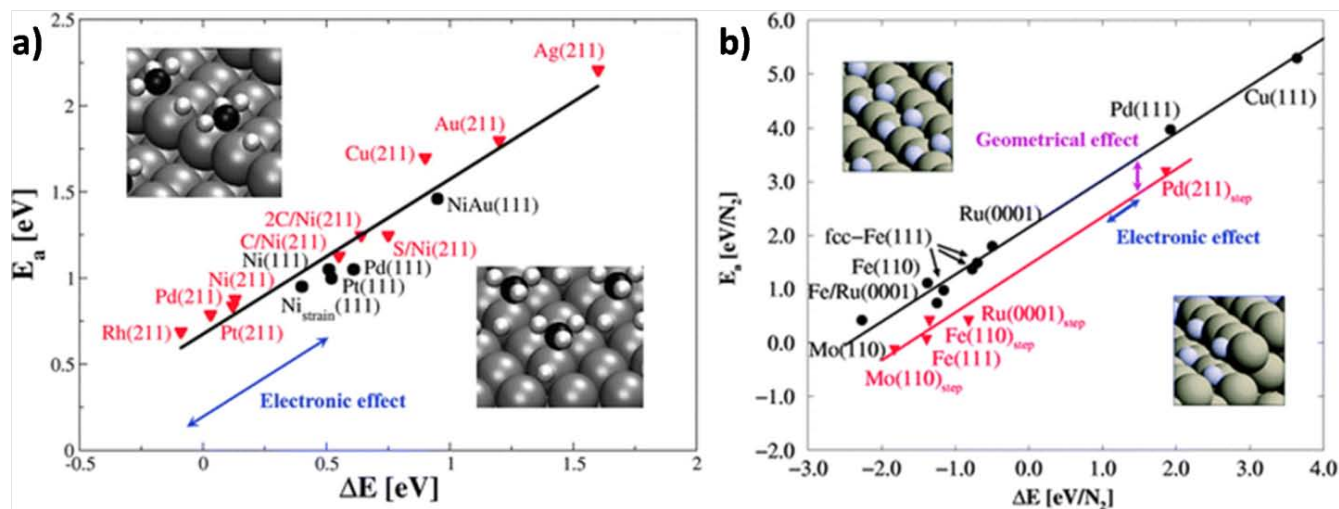
Figure 1.5: The BEP relations for dissociation of a) methane and b) N_2 over stepped and closed packed surfaces of different metals.[56,66,68]

The Figure 1.5 shows the BEP lines for dissociation of methane and N_2 on different crystal structures. For dissociation of methane a linear relation is found, still there can be electronic effects which can change the reaction energy. From the Figure 1.5a it can be seen that Ni {221} is shifted to left when compared to Ni {111}. This can be attributed to the concept of d band. The step atom is under coordinated and have high lying d band center which can interact with adsorbate strongly. This electronic effect causes the displacement in BEP lines.

Considering the dissociation of N_2, there is large shift in BEP lines of different geometries. It is found that stepped and open surfaces have low lying BEP lines. This shows that if the point of a given metal changes on the x-axis when geometry changes, the effect is purely electronic and if the reaction energy is fixed and the Ea changes then the effect is purely geometrical. Thus both these effects can be separated. Three classes of structural dependence of surface reactivity have been concluded by BEP analysis method namely strong structural effects (due to geometrical effects), weak structural effect (electronic effect) and no structural effects. This can theoretically provide an idea about the nature of active sites in heterogeneous catalysis at a molecular level. How the BEP relations determine the trends in catalytic activity from one metal to the next has been explained through the so-called volcano relationships.[56]

1.5.   Elucidation of active sites

The presence of under coordinated atoms on the surface of a nanoparticle makes it active for a chemical reaction. Such atoms or group of atoms which can activate reactant molecules and which can change the course of a chemical reaction can be termed as 'Active sites' as proposed by Taylor in 1925.[57] The concept of such ensemble of atoms in the form of B5 sites on Ru nanocluster[69] and C7 sites on Fe {111} single crystal surface[70] and their role of increasing the activity towards ammonia synthesis has been reported by Dahl et.al[69] and Spencer et.al.[70] The elucidation of active sites responsible for catalytic activity is an area of immense interest and has paved way for several reports from UHV studies on single crystal surfaces to real world nanocatalysts.

1.5.1.   Model single crystal surfaces

Catalysis at the surface is found to be sensitive to the size and arrangement of atoms at the interface where the reaction occurs. This structure-activity relationship has been elucidated on single crystal surfaces and has motivated the synthesis of shape controlled nanoparticle systems. The development of surface science techniques to model nanoparticle surfaces is summarized in Figure 1.6. The extensive use of UHV techniques for studying the interaction of molecules with surface of metals have led to further understanding of properties of a surface under operating conditions. The conditions used in UHV techniques are highly ideal, the pressures

used is several magnitude of orders less (10^{-10} mbar) when compared to a real world catalytic system which operates at high pressures (1-100 bar). This can be termed as Pressure Gap in surface science. Moreover a catalyst is a metal in nanoregime most commonly supported on high surface area support; these metal nanoparticles are polycrystalline and exposes rough surfaces of different low energy facets. But the single crystal surfaces used in surface science studies exposes a single facet which is smooth on an atomic scale. This is termed Material Gap in surface science. Due to the much idealized nature of the surface science UHV studies, its relevance to the real world catalysis phenomena should be established. Recently, experimental systems are developed where a high pressure reactor system is combined with a UHV chamber.[71] The kinetics of the reaction can be obtained from reactor system and the understanding of catalytic system before and post reaction can be done in the UHV analysis chamber.

Figure 1.6: The developments in surface science ranging from UHV techniques to nanoparticle systems.[72]

The importance of defect sites catalyzing chemical reactions has been well appreciated in surface chemistry and catalysis. It has been proved that a stepped or kinked surface can change the course of a chemical reaction by lowering the activation barrier for bond breaking and making when compared to a terrace site. The production rate of ammonia was found to depend on the facet exposed and the formation rate followed the order

Fe {111} >> Fe {100} > Fe {110}.[70,73-74] Another report showed that a stepped surface Fe {211} was more active than Fe {210} for ammonia production. Single crystal surface science studies on Pt crystals have shown that only cyclohexane was formed during benzene hydrogenation on {100} facet while mixture of cyclohexane and cyclohexene is formed on {111} facets and this was experimentally proved by Somorjai on shape controlled nanoparticle surfaces.[75-77] The dissociation of N_2 was found to be totally dominated by steps than on terrace sites by DFT and Molecular Beam (MB) techniques by Chorkendorff and coworkers.[60] A theoretical study also proved that the adsorption and activation of molecules like O_2 and CO is more favorable on step sites than on terrace.[78] Surface science studies on stepped single crystal surface have contributed immensely to the understanding of defect chemistry. The step sites on Au {310} surface were found to decompose small molecules like NO and methanol as reported by Vinod and coworkers.[79] The general trend in the activity of small molecules on nanoparticles has been presented recently and highly recommended for further reading.[79-82]

1.5.2. Model Nanoparticle systems

The size, morphology and composition dependent catalytic activity studies have been pursued over the past decade. The shape of the nanoparticle determines the anisotropy, crystallinity and exposed facets of the material. Facets are the flat faces of a particular polyhedron. Based on the arrangement of atoms on the exposed planes, faceted nanomaterials are of two categories low index and high index faceted nanoparticles and can be denoted by miller index values.[83]

1.6. Low index faceted nanoparticles

Low index facet is one where the sum of all the three components {hkl} is small. If the growth of a facet is under thermodynamic control, such nanomaterial will be bound by low index facets viz {111}, {100}, {110} depending on their surface energy. For fcc metals the surface energy of the nanoparticle follow the order γ{111} < γ{100} < γ{110} < γ{hkl}.[84-85] For noble metal commonly observed shapes are octahedrons, truncated octahedrons, cubes, cubooctahedron with different propotions of {111}/ {100}/ {110} facets (see Figure 1.7).These morphologically controlled transition metal nanoparticles have found potential applications as

catalyst for Suzuki reactions,[86-87] CO oxidation,[88] styrene oxidation,[89] hydrogenation[44,90-92] and electrocatalytic reaction.[93-94]
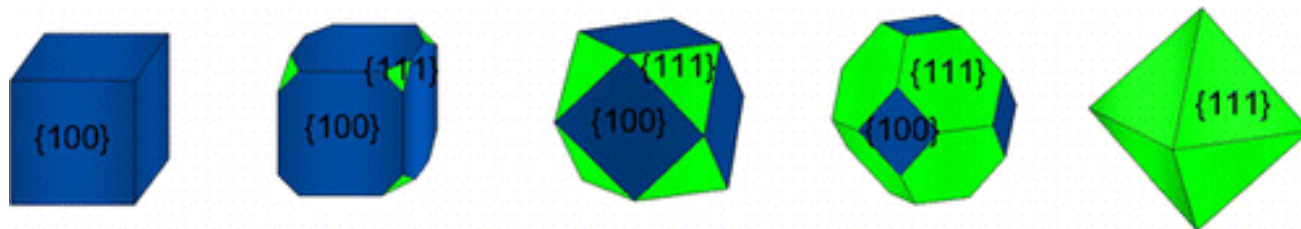
Figure 1.7: The morphology of different low index faceted nanostructures which can be obtained by changing the {111} to {100} facet ratio.[95]

1.7. High Index faceted nanoparticles

High index faceted nanoparticles are denoted by a set of miller indices {hkl} value where one of the values is greater than unity.[37] They expose open surfaces with atoms of under co-ordination. These under coordinated atoms can serve as active centers for a chemical reaction. Due to this they exhibit better catalytic activity when compared to their low index counterparts. The high index facets grow faster to minimize the surface energy. Apparently it is a challenge to synthesise such high energy surfaces.

1.7.1. Determination of high index facets

A direct relationship between the surface plane and polyhedral profile can be deduced from the unit stereographic triangle as shown in Figure 1.8.[96] In this graph, the three vertices of the triangle represent the three low index polyhedra: a cube with 6 {100} facets, an octahedron with 8 {111} facets and a rhombic dodecahedron with 12 {110} facets. In contrast the polyhedrons lying along the edges and inside the triangle represents high index faceted polyhedras namely Tetrahexahedron {hk0} (THH) which exposes 24 ($h > k > l = 0$) high index facets, Trapezohedron TPH by 24 {hkl} ($h > k = l > 0$), Trisoctahedron TOH by 24 {hkl} ($h = k > l > 0$), and Hexooctahedron HOH by 48 {hkl} ($h > k > l > 0$) facets. An increasing number of such facets increase the number of under coordinated sites such as steps and kinks. A high indexed polyhedron lying along the edge can be geometrically viewed as an integration of two low index faceted polyhedral lying along the two ends at its sideline. For instance, THH is integration between a cube and a rhombic dodecahedron. All the

14

polyhedras presented in the triangle are convex structures. For example THH can be considered as a cube with each face "pulled out" to form a square pyramid. In contrast to them, concave polyhedra enclosed by the same group of high-index facets are also achievable by "pushing in" the centers of the desired facets.
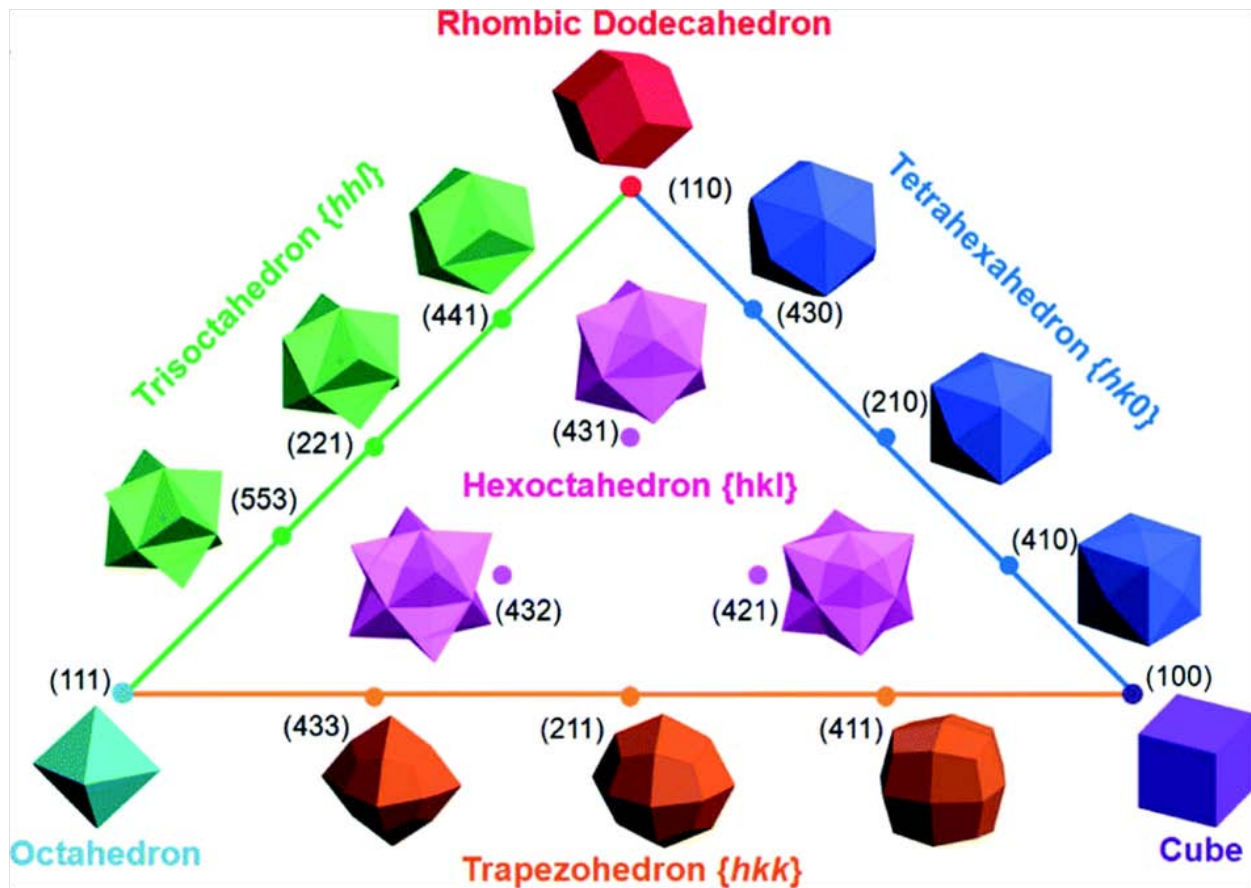
Figure 1.8: Unit stereographic triangle showing different high index faceted nanoparticle systems.[37,96]

In this graph, the three vertices of the triangle represent the three low index polyhedra: a cube with 6 {100} facets, an octahedron with 8 {111} facets and a rhombic dodecahedron with 12 {110} facets. In contrast the polyhedrons lying along the edges and inside the triangle represents high index faceted polyhedras namely Tetrahexahedron {hk0} (THH) which exposes 24 (h > k > l = 0) high index facets, Trapezohedron TPH by 24 {hkl} (h > k = l> 0), Trisoctahedron TOH by 24 {hkl} (h = k > l > 0), and Hexooctahedron HOH by 48 {hkl} (h > k > l > 0) facets. An increasing number of such facets increase the number of under coordinated sites such as steps and kinks. A high indexed polyhedron lying along the edge can be geometrically viewed as an integration of two low index faceted polyhedral lying along the two ends at its sideline. For instance, THH is integration

between a cube and a rhombic dodecahedron. All the polyhedras presented in the triangle are convex structures. For example THH can be considered as a cube with each face "pulled out" to form a square pyramid. In contrast to them, concave polyhedra enclosed by the same group of high-index facets are also achievable by "pushing in" centers of the corresponding surfaces. For example, a concave cube could be viewed as a cube with centers of the six square faces "pushed in" to generate square pyramid-shaped depressions. THH, TOH and TPH which lie along the edges of the triangle corresponds to $\{001\}$, $\{01\bar{1}\}$ and $\{1\bar{1}0\}$ crystallographic zone axis and the facets expose characteristic step-terrace geometry.

1.7.2. Microfacet notation for denoting stepped surfaces
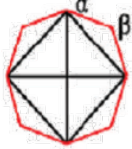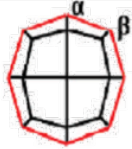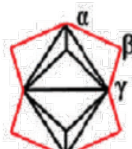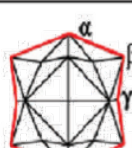
High-indexed polyhedron	Zone	Surface facets	Miller index (n≥2)	Microfacet notation	Projection direction	Projection image	Projection angel /degree
Tetrahexahedron (THH)	[001]	{hk0}$_{24}$ (h>k>0)	(n,n-1,0)	n(110)x(100)	[001]		$a = 2\,\mathrm{arctan}\left(\dfrac{h}{k}\right)$
			(n,1,0)	n(100)x(110)			$\beta = 270-\alpha$
Trapezohedron (TPH)	[01$\bar{1}$]	{hkk}$_{24}$ (h>k>0)	(n+1,n-1,n-1)	n(111)x(100)	[001]		$a = 2\,\mathrm{arctan}\left(\dfrac{h}{k}\right)$
			(2n-1,1,1)	n(100)x(111)			$\beta = 270-\alpha$
Trisoctahedron (TOH)	[1$\bar{1}$0]	{hhl}$_{24}$ (h>l>0)	(n+1,n+1,n-1)	n(111)x(110)	[110]		$\alpha = 2\,\mathrm{arctan}(\dfrac{\sqrt{2}h}{h-l})$ $\beta = 90-(\alpha/2)+(\gamma/2)$
			(2n-1,2n-1,1)	n(110)x(111)			$\gamma = 2\,\mathrm{arctan}(\dfrac{\sqrt{2}h}{l})$
Hexoctahedron (HOH)		{hkl}$_{48}$ (h>k>l>0)			[110]		$\alpha = 2\,\mathrm{arctan}(\dfrac{\sqrt{2}h}{h-l})$ $\beta = 90-(\alpha/2)+(\gamma/2)$ $\gamma = 2\,\mathrm{arctan}(\dfrac{k+h}{\sqrt{2}l})$

Table 1.1: The table showing the crystallographic facets of different classes of high index faceted polyhedras and projection method to evaluate their microfacet notation.[37]

A microfacet notation of the form $n(h_t k_t l_t) \times (h_s k_s l_s)$ has been developed by Somorjai and coworkers to visualize the high index stepped surface on Pt nanoparticle.[97] The notation means there is n atom wide $(h_t k_t l_t)$

terrace followed by atomic $(h_s k_s l_s)$ steps. It can be easily deduced from the table 1.1, the notation for specific polyhedra. For example, {331} facets on TOH can be expressed as 2(111) X (110), indicating a stepped surface composed of a terrace in two atomic width of (111) symmetry, separated by a monatomic step of (110) symmetry as shown in Figure 1.9.[42]
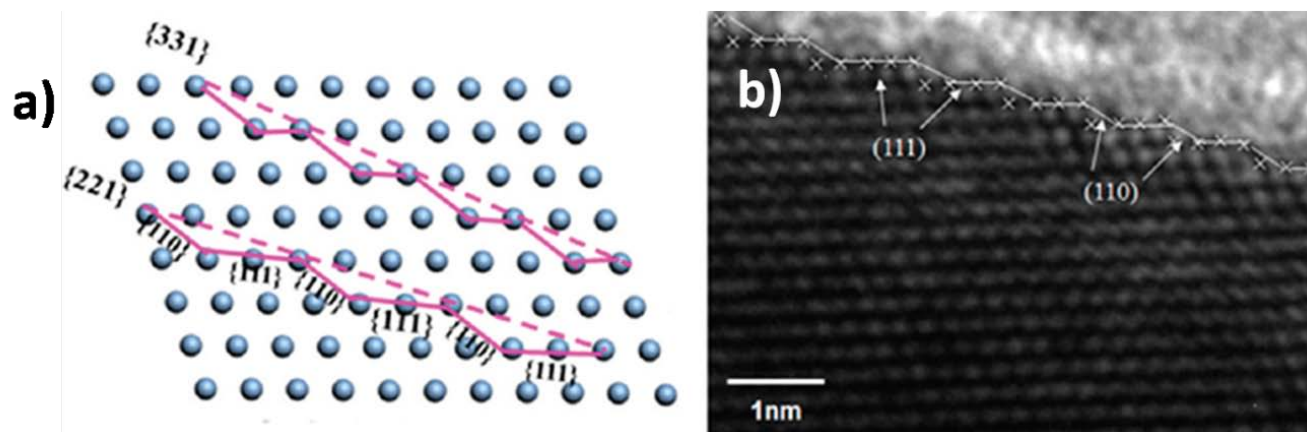
Figure 1.9: The HRTEM image of a trisoctahedral Au nanoparticle showing the step terrace geometry along the edge and the atomic model of the same.[42]

1.7.3. Projection angle method for the identification of high index facets

Angle {hkl}	α	β	γ
{221}	141°	90°	141°
{331}	129.5	102°	153.5°
{441}	124°	108°	160°
{332}	153.5°	78°	129.5°
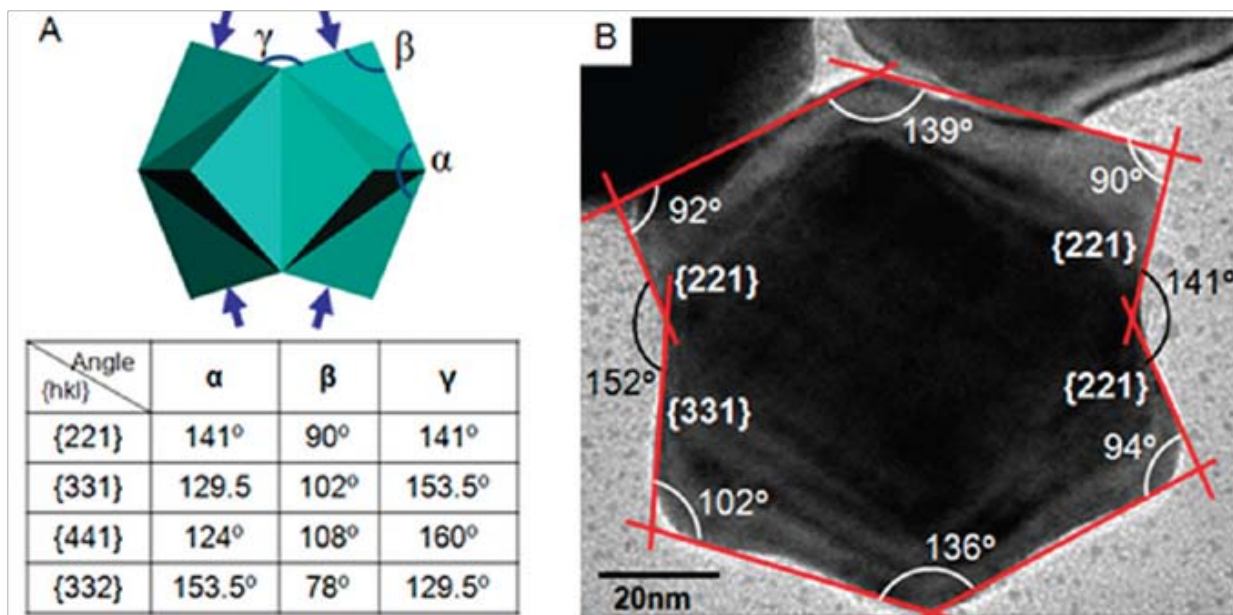
Figure 1.10: The model of trisoctahedra along with the theoretically calculated projection angles and TEM image of the same showing the experimentally derived angles for the determination of high index facets.[42]

This is another simple and efficient way to visualize a high index facet by measuring the projection angle along an appropriate crystallographic zone axis. For example from the table 1.1 we can deduce that a trisoctahedra can be best viewed as octagons along [110] projection direction projecting angles α and β and γ which can be calculated using appropriate equations as shown in the table 1.1 and the TEM image showing the experimentally derived angles (see Figure 1.10).[42]

1.7.4. Morphologically controlled high index faceted structures and their reactivity

The developments made in the synthesis strategy have paved way for the numerous numbers of reports on high index faceted nanoparticles and their enhanced chemical activity.[37,84] In the following section we discuss the reactivity of specific high index planes.

{hk0} facets:

Na Tian and co-workers synthesized Platinum nanocrystals of Tetrahexahedral shape from Platinum nanospheres by applying a square wave potential.[98] The single crystals were enclosed by 24 high index facets such as {730}, {210} and {520} which have large number of dangling bonds and atomic steps. They showed enhanced chemical activity in electro oxidation reaction.[98] Xia and coworkers were able to synthesise Platinum concave nanocubes enclosed by {510}, {720}, {830} by the simple reduction of Pt precursor in aqueous solution.[99] Han et al developed a facile yet effective seed-mediated method which produced a high yield of Au NPs with a well defined truncated ditetragonal prism (TDP) shape at room temperature. [100] The monodisperse Au TDP NPs are single crystals enclosed by 12 high-index {310} facets. Electro deposition method to fabricate THH Pd NCs enclosed by {730} high-index facets were reported and they exhibited 4-6 times higher catalytic activity than commercial Pd black catalyst.[101] Fivefold twinned Pd nanorods bound by high-index facets of {hk0} or {hkk} prepared by an electrochemical method were found to show high activity for ethanol oxidation.[102] Xia et al reported a simple procedure based on seeded growth to the synthesis of Pd concave nanocubes bound by high index {730} facets, where Pd nanocubes were used as seeds for the reduction of a Pd precursor in an aqueous solution.[103] These Pd concave nanocubes were found to exhibit a high catalytic activity towards Suzuki reaction. Nanocatalysts with high index facets exposed were found to improve the rate of

oxygen reduction reaction (ORR). For example, it was reported that the specific activity toward ORR on {720} bound Pt concave nanocubes was higher than that of low-indexed Pt nanocubes and Pt nanocuboctahedra respectively of similar size.[99]

{hhl} facets:

As a successful example in solution phase synthesis of high-indexed nanopolyhedra, Au TOH NCs with a size of larger than 100 nm were prepared, and their surface planes were ascribed to 24 {221} facets.[42] Subsequently concave trisoctahedral (TOH) gold nanocrystals (NCs) enclosed by {221} and {331} facets with uniform and customizable sizes were synthesized by a seed-mediated growth method CTAC as the capping agent by Lu etal.[40, 104] Taking {221} as an example, it can be described as 3(111) X (110) based on micro facet expression, in which the atomic arrangement is periodic with three atomic widths of (111) terraces, followed by one atomic width of a (110) steps.[42] These structures were found to exhibit distinct optical properties.

{hkk} facets:

Zhou and coworkers synthesized a trapezohedra TPH Pd exposing 24 {hkk} facet by electrochemical method and they were found to show enhanced chemical activity towards oxidation of small organic fuels.[105] Zheng et.al described a synthesis strategy for {hkk} facet bound Pd octapods. These octapods were found to expose {411} facets.[106-107] High index {hkk} facets has been also observed for Pd fivefold twinned nanorods and Pt tripod structures.[102,108]

{hkl} facets:

Hexoctahedron (HOH) is a representative polyhedral exposing 48 {hkl} facets. This polyhedron can be viewed as trisoctahedra with each edge bending outward from the center or a tetrahexahedra with each edge bending inward from the center. Platinum nanocrystals with HOH morphology were first synthesized by Zhou et al and is found to catalyze formic acid oxidation effectively.[105] HOH Au nanoparticles were also reported and were found to show enhanced SERS activity.[109] The representative microscopic images of high index faceted nanoparticle systems are shown in Figure 1.11.
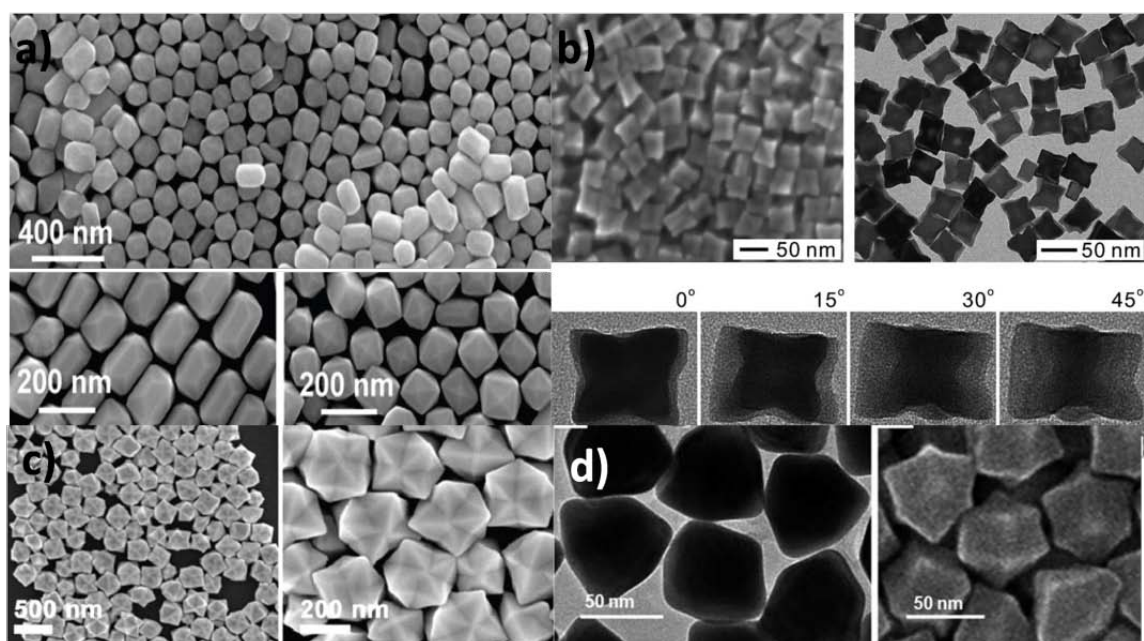
Figure 1.11: Microscopic details of different high index faceted nanostructures showing a) tetrahexahedron Au,[110] b) Pd concave cubes,[111] c) ditetragonal Au prism,[100] and d) spindle shaped Au nanoparticles.[112]

1.8. Analytical Methods

Morphology controlled nanoparticles can be characterized by various analytical tools. The following section gives a brief introduction to these techniques and also the equipments used in this thesis for studying catalysis by these materials.

1.8.1. UV-Visible spectroscopy

UV-Visible spectroscopy is an analytical technique used to quantify the amount of absorbed and scattered light by a sample. The sample of interest is placed between a light source and a photo detector, and the intensity of a beam of light is measured before and after passing through the sample. These measurements are compared at each wavelength to quantify the sample's wavelength dependent extinction spectrum. The data is typically plotted as extinction as a function of wavelength. Each spectrum is background corrected using a "blank". This method has been used to characterize metal nanoparticles in colloidal solution Metal nanoparticles in solution absorbs light in the UV-Vis region of the electromagnetic spectrum and will give a broad absorption spectra; typically gold, silver and copper nanoparticles in the visible region. These absorptions

are due to the phenomenon of Surface Plasmon Resonance (SPR). The SPR can be described as the collective oscillation of the conductive electrons in a solid stimulated by incident light. The origin of SPR in noble metal nanoparticle has been discussed by El sayed and coworkers.[113]
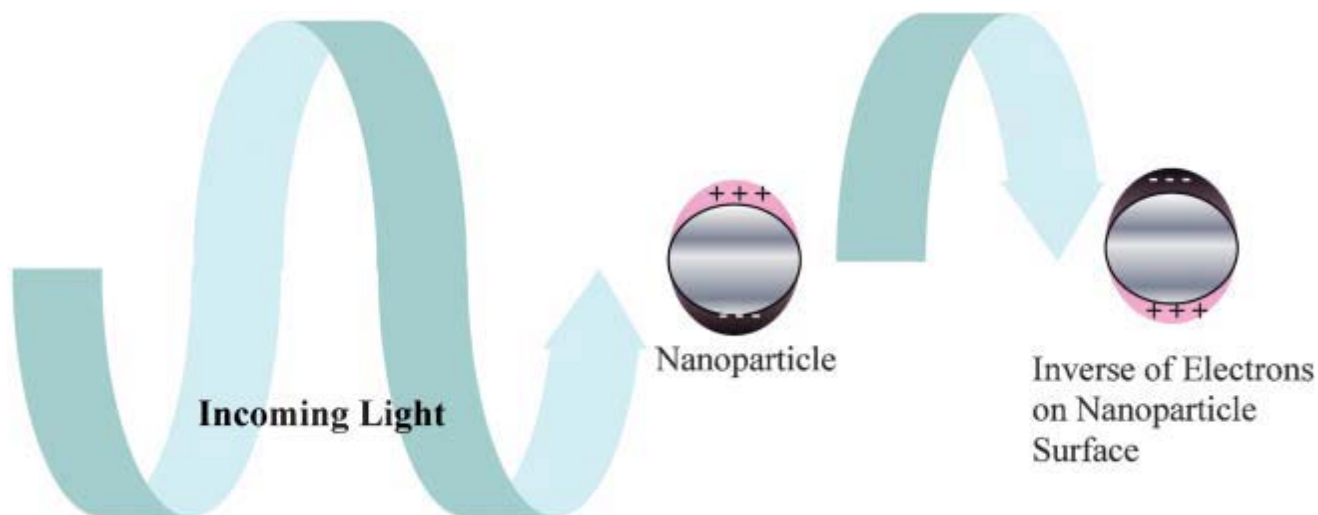
Figure 1.12: Schematic representation of origin of surface Plasmon Resonance by the interaction of conduction band electrons with light.[113]

The free d electrons with approximate mean free path of 50 nm in case of gold and silver are mobile on a nanoparticle surface. When the nanoparticle size is less than this mean free path, no scattering occurs and when the wavelength of incident light is much larger than the nanoparticle size, it can set up oscillation of surface electrons as shown in Figure 1.12. As the wave front of the light passes, the electron density in the particle is polarized to one surface and oscillates in resonance with the light's frequency causing a standing oscillation. The resonance condition is referred to as the surface plasmon resonance, since it is located at the surface. The resonance depends on size, shape, solvent, dielectric constant etc.

1.8.2. X-ray diffraction

Powder X-ray diffraction is extensively used for the characterization of synthesized crystalline materials. It is used mainly for the identification of unknown materials and to characterize the crystallographic structure, crystallite size (grain size), and preferred orientation in polycrystalline or powder solid samples. The XRD

method involves the interaction between the incident monochromatized X-rays (like Cu Kα or Mo Kα source) with the atoms of a periodic lattice. X-rays scattered by atoms in an ordered lattice interfere constructively in directions given by Bragg's law:

$$n\lambda = 2d \sin \theta$$

Where, λ is the wavelength of the X-rays, d is the distance between two lattice planes, θ is the angle between the incoming X-rays and the normal to the reflecting lattice plane and n is an integer known as the order of reflection.

Bragg peaks are measured by observing the intensity of the scattered radiation as a function of scattering angle 2θ. The angles of maximum intensity enable one to calculate the spacing's between the lattice planes and allow phase identifications while the width of diffraction peaks carries information on the dimensions of the reflecting planes. The width of the diffraction lines can be further used to estimate the crystal size by the Debye-Scherrer formula: $D_{hkl} = \frac{\alpha \kappa \lambda}{\beta \cos \theta}$ where $Dhkl$, λ, β and θ are the volume averaged particle diameter, X-ray wavelength, full width at half maximum (FWHM) and diffraction angle, respectively, and k is a constant, often taken as 1.[114]

A major limitation of XRD is that this technique requires samples, which possess sufficient long-range order. Amorphous phases and small particles give either broad or weak diffraction lines or no diffraction at all, which makes them virtually invisible for XRD.

1.8.3. Transmission Electron Microscopy

Transmission electron microscope is a powerful analytical tool for nanomaterial science. The atomic details can be analyzed by looking at the interaction between the sample and high energy electrons which are incident on a thin layer of sample. TEM works on the principle of optical microscope but uses electrons instead of light. Since the wavelength of accelerated electrons is small, (~ 2.24 pm at 300 keV) one can get the finest internal structure even the individual atoms.[115-116] A coherent beam of accelerated electrons from the field emission or thermionic emission is focused onto specimen using a condenser lens. Depending on the thickness and electron transparency of the sample, the electrons are transmitted through the sample.
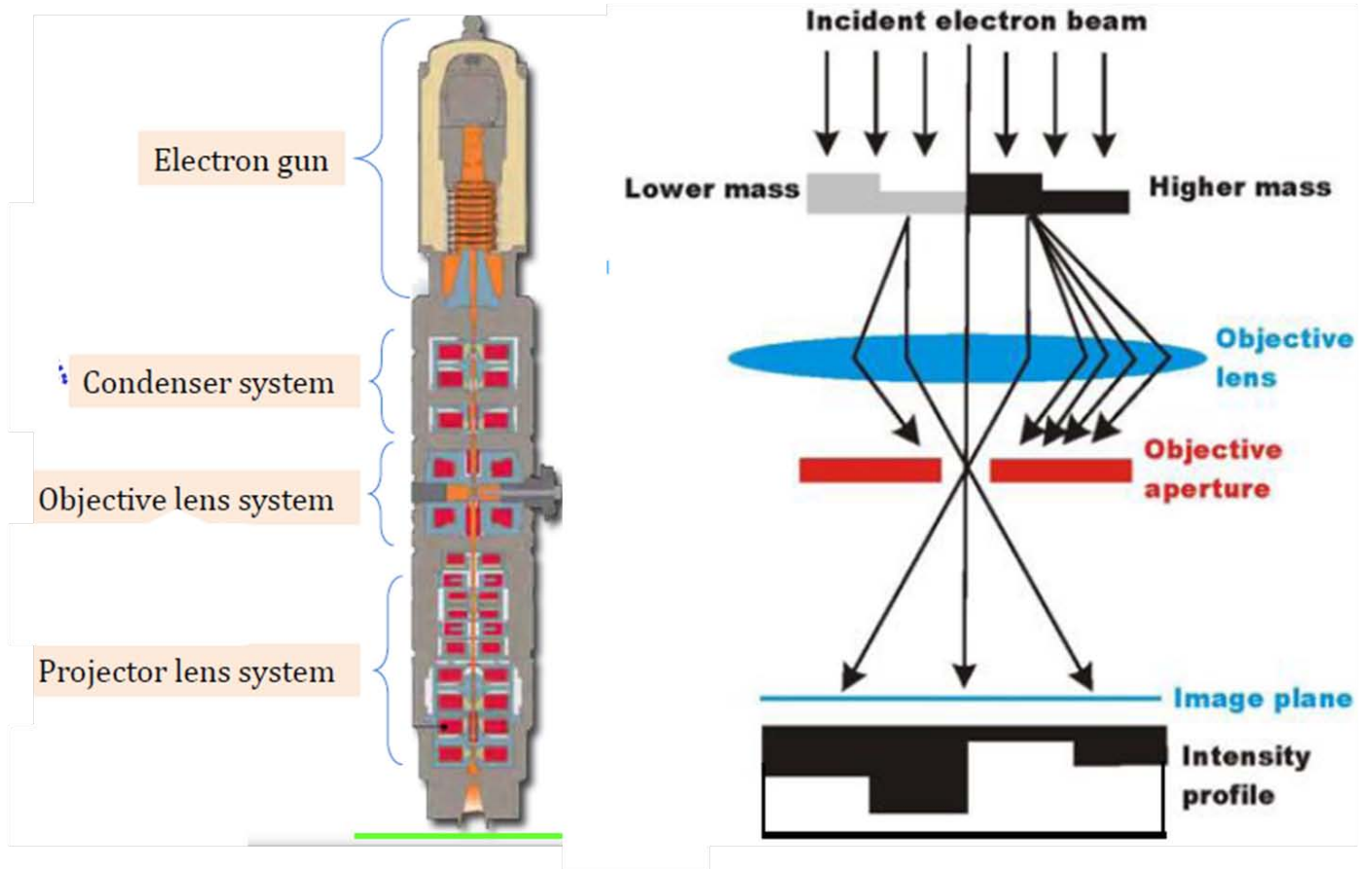
Figure 1.13: The schematic representation of transmission electron microscope.

These transmitted electrons are directed to phosphor screen or charge coupled device using a objective lens Objective apertures are used to enhance the contrast by filtering out high-angle diffracted electrons. The image is enlarged and the contrast is found to depend on atomic number The areas having dark contrast shows that fewer electrons are transmitted (higher atomic number) while lighter areas represent those areas where there are fewer electrons on the sample. The Figure 1.13 shows a schematic representation of path of electron beam from electron gun to phosphor screen or CCD camera.

1.8.4. Inductively coupled Plasma (ICP) spectroscopy

Inductively coupled plasma spectroscopy, is an analytical technique used for the detection of the trace metals. It is a type of emission spectroscopy that uses the inductively coupled plasma to produce excited atoms and ions that emit electromagnetic radiations at wavelengths characteristic of a particular element. The intensity of this emission is indicative of the concentration of the element within the sample.Plasma is an electrically

conducting gas of cations and free electrons in significant concentration. Argon is the most commonly used gas for generating the plasma as the argon ions formed are capable of absorbing energy to attain high temperatures of the order of 10,000 K and sustain the plasma for prolonged periods, almost indefinitely by further ionization.

1.8.5. Gas Chromatography

Gas Chromatography is a analytical tool to measure the concentration of components present in a sample. The method is based on the selective adsorption and desorption of sample on to a stationary phase. This means that the solutes are continuously partitioned between the adsorbent and the mobile phase either a gas or a solvent mixture. The stronger the interaction of the solute with stationary phase, the slower the solute will progress. The motion of the solute and solvent through the stationary phase in called elution. GC is carried out using an instrument containing a long but very thin metal tube filled with an inert support (usually silica) as the stationary phase and a stream of carrier gas as the mobile phase. The coiled tube, the "column" is heated in a thermostatically controlled oven. A dilute solution of the liquid sample is typically prepared in a volatile solvent such as diethyl ether. A small amount of this sample solution is then injected onto the column and is carried forward by the helium carrier gas. The oven temperature is typically gradually increased up to about 270 ^{o}C over a 10 to 20 minute period. In general, the lower the boiling point of the liquid, the quicker it will be carried through the column (so it has a short retention time). When the sample exits the column, the liquid is detected by the detector and the amount of liquid is measured, this information is usually plotted as a "trace" with x axis as time and the y axis the response of the detector as the abundance (i.e. the amount detected). The detectors are of different types like Flame Ionsiation detector, thermal conductivity detectors, Electron capture detector, Photo ionization detector etc. The carrier gas can be Nitrogen, helium or argon and should be chemically inert.

1.8.6. N$_2$ Physisorption

The most common method of measuring surface area and textural characteristics of catalytic materials is that based on the theory developed by Brunauer, Emmett and Teller (BET), considering the multilayer adsorption. The BET equation can be represented as:

$$p/v_{(p_0-p)} = 1/V_{mc} + [(c-1)cV_m]p/p_0$$

where, p is adsorption equilibrium pressure, po is saturation vapour pressure of the adsorbate at the experimental temperature, V is volume of N_2 adsorbed at pressure p, Vm is volume of adsorbate required for monolayer coverage and c, a constant that is related to the heat of adsorption and liquefaction. A linear relationship between $p/v_{(p_0-p)}$ and p/p_0 is required to obtain the quantity of nitrogen adsorbed. The monolayer volume, V_m is given by $1/{S+I}$, where S is the slope and is equal to $C-1/{cV_m}$ and I is the intercept equal to $1/{cV_m}$ The surface area of the catalyst is related to Vm, by the equation, $SA = \left(V_m/22414\right)N_a\sigma$ where Na is Avogadro number and σ is mean cross sectional area covered by one adsorbate molecule. The σ value generally accepted for N_2 is 0.162 nm^2. Several computational procedures are available for the derivation of pore size distribution of mesoporous samples from physisorption isotherms. Most popular among them is the Barrett-Joyner-Halenda (BJH) model, which is based on speculative emptying of the pores by a stepwise reduction of p/po, and allowance being made for the contraction of the multilayer in those pores already emptied by the condensate. The mesopore size distribution is usually expressed as a plot of $\Delta V_p/\Delta r_p$ versus r_p, where V_p is the mesopore volume, and r_p is the pore radius.

1.8.7. Dynamic Light scattering

Small particles in suspension undergo random thermal motion known as Brownian motion. This random motion is modeled by the Stokes-Einstein equation. Below the equation is given in the form most often used for particle size analysis.[117]

$$D_h = kB_T/3\pi\eta D_t$$

where D_h is the hydrodynamic diameter of the particle, D_t is the translational diffusion coefficient, k_B Boltzmann constant, T- temperature, η is the dyanamic viscosity.

Light from the laser light source illuminates the sample in the cell. The scattered light signal is collected with one of two detectors, either at a 90 degree (right angle) or 173 degree (back angle) scattering angle. The

provision of both detectors allows more flexibility in choosing measurement conditions. Particles can be dispersed in a variety of liquids. Only liquid refractive index and viscosity needs to be known for interpreting the measurement results.
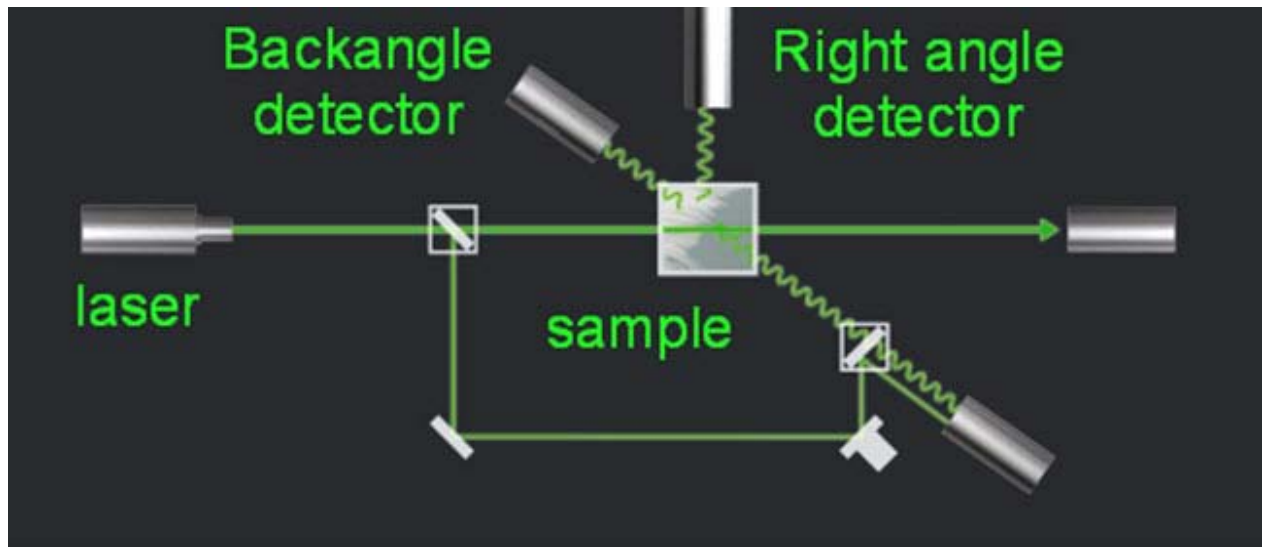
Figure 1.14: The Schematic representation of dynamic light scattering experiment.

The obtained optical signal shows random changes due to the randomly changing relative position of the particles. The signal can be interpreted in terms of an autocorrelation function. Incoming data is processed in real time with a digital signal processing device known as a correlator and the autocorrelation function as a function of delay time, τ, is extracted. For a sample where all of the particles are the same size, the baseline subtracted autocorrelation function, C, is simply an exponential decay of the following form:

$$\mathcal{C} = \exp(-2\Gamma\zeta)$$

The decay constant is proportional to the diffusion coefficient. Γ is readily derived from experimental data by a curve fit. The diffusion coefficient is obtained from the relation $\Gamma = D_t q^2$ where q is the scattering vector, given by $= \left(\frac{4\pi n}{\lambda}\right) \sin \frac{\theta}{2}$. The refractive index of the liquid is n. The wavelength of the laser light is λ, and scattering angle, θ. Inserting D_t into the Stokes-Einstein equation above and solving for particle size is the final step.

1.8.8. Raman spectroscopy

Raman spectroscopy is based on the inelastic scattering of photons which lose energy by exciting vibrations in the sample.[118] When monochromatic light of frequency υ_o falls on a sample, majority of the photons are elastically scattered and termed as Rayleigh scattering or inelastically in which a vibration is excited (stokes band with frequency($\upsilon_0 - \upsilon_{vib}$) or a vibrationally excited mode in the sample is deexcited (anti stokes band with frequency ($\upsilon_0 + \upsilon_{vib}$). The spectrum is that of the light scattering by the sample. Stokes lines are at lower energy while the anti-Stokes lines are at energy greater than the Rayleigh peak. The positions of Raman lines are expressed in $^-\bar{\upsilon}_s$ terms of Raman shift, $\Delta\upsilon$ which is defined as per the following equation, $\Delta\upsilon = (\bar{\upsilon}s - \bar{\upsilon}o)$ cm^{-1} Where, $\bar{\upsilon}_s$ and $\bar{\upsilon}o$ are the wave numbers of the source (or incident) radiation and the observed scattered lines respectively. It is obvious that the Raman shifts of the Stokes lines would be positive while for anti-Stokes lines, these would be negative.

1.8.9. Fourier Transform Infrared Spectroscopy (FTIR)

Absorption in the infrared region results in changes in vibrational and rotational status of the molecules.[118] A molecule will absorb infrared light only if the absorption causes a change in the dipole moment. IR spectroscopy is the technique widely used for elucidating the structure of molecules as well as determining the purity of compounds. An IR spectrum is commonly obtained by passing IR radiation through a sample and determining what fraction of the incident radiation is absorbed at a particular energy. The energy at which any peak in an absorption spectrum appears corresponds to the frequency of a vibration of a part of a sample molecule. In an FT-IR spectrometer, the radiation emerging from a source is passed through an interferometer to the sample before reaching a detector. Upon amplification of the signal, in which high frequency contributions have been eliminated by a filter, the data are converted to a digital form by an analog-to digital converter and transferred to the computer for Fourier transformation. Here the entire spectrum is obtained for each scan the interferometer makes, with the result that the total collection time needed to measure a spectrum is much lower.

1.9. Scope and objectives of the thesis work

Determination of active sites is an extremely important area of research in heterogeneous catalysis. The synthesis of new functional nanomaterials with improved activity, selectivity and stability rely on the identification of 'active sites'. Understanding and elucidating the concept of active sites on a real catalyst surface by adopting ideas from model single crystal surface science studies is attempted. To develop synthesis protocols for well defined model nanostructures of gold, palladium and ruthenium metals which carry the periodic active centers in the form of steps or kinks has been attempted. The main objective of the thesis is to use such morphology controlled nanostructures for studying and validating the structure versus activity correlations in catalysis.

1.10. Organization of thesis

The thesis is divided into 5 chapters. An abstract of each chapter is given below.

Chapter 1: This chapter gives an introduction to nanocatalysis, single crystal surface science studies, model nanoparticle systems which expose low and high index facets, structure-sensitivity or facet dependent chemical activity and theoretical background for structure sensitivity. This chapter also discusses the analytical methods for the characterization of catalyst and tools used for analyzing catalytic reaction. It gives an outline about the objective of the thesis.

Chapter 2: This chapter deals with the elucidation of active sites on Au nanoparticles in oxidation catalysis. Briefly, the role of under coordinated step atoms, the presence of active metal-oxide interface and confinement effects are probed using supported large trisoctahedral (TOH) Au nanoparticles towards catalyzing CO oxidation. The trisoctahedral Au nanostructures which are found to expose periodic under coordinated step sites which potentially activate molecules. They are supported on suitable supports and tested for benchmark CO oxidation reaction. The proposed active metal-oxide perimeter model is elucidated by making an inverse system i.e. TOH Au decorated by suitable metal oxide and by testing for CO oxidation. Further to this, the trisoctahedral and the inverse system are confined in a porous shell, and the effect of this confinement on the

chemical reactivity is probed. This chapter proves that Au can be made catalytically active in a size regime it was previously demonstrated not to be active thereby proving the role of under coordinated atoms and role of metal support interfaces.

Chapter 3: In this chapter, Palladium which is a good candidate for many hydrogenation, oxidation and coupling reaction is tested for its structure sensitivity towards gas phase and liquid phase reactions. A seed mediated synthesis protocol for the formation of Pd concave cubes and nanoflowers which exposes high index facets like {310} and {311} that carries periodic defective centers is made. These nanoparticles in colloidal form are used to catalyse Suzuki and Heck coupling. An attempt to correlate structure-activity relations is made by comparing the activity of these high index faceted nanostructures with their low index counter parts. The efficiency of these high index faceted structures in catalyzing gas phase reaction like CO oxidation reaction is also probed and reported in this chapter.

Chapter 4: This chapter explains the catalytic activity of a self assembled Ruthenium nanostructure. The area of self assembled nanostructures has gained importance as they can bridge the gap between nano and macro size regime. Briefly, the chapter deals with the synthesis of Ru nanochains using a surfactant assisted seed mediated protocol under mild conditions. They are found to possess corrugations and furrows on their surface which can act as active centers. They are demonstrated to outperform small spherical Ru nanoparticles in CO oxidation reaction.

Chapter 5: This chapter summarizes the conclusions drawn upon the investigations done on different structured nanoparticle systems catalyzing reactions of industrial importance. The importance of under coordinated atoms which can act as active centers in a chemical reaction is elucidated by adopting ideas from surface science studies. Such model nanoparticle surfaces are closer to the real world catalysts and can be excellent materials for bridging the material gap in surface science.

1.11. References

(1)   Berzelius, J. J. *Annls.Chim.Phys,* **1836**, 146.

(2)   King, C. V.; Steinbach, O. F. *J Am Chem Soc,* **1930**, *52*, 4779.

(3)   Nishimura, S. *Handbook of heterogeneous catalytic hydrogenation for organic synthesis*; Wiley New York etc, 2001.

(4)   Jennings, J. R. *Catalytic ammonia synthesis: fundamentals and practice*; Springer Science & Business Media, 2013.

(5)   Twigg, M. V.; Twigg, M. *Catalyst handbook*; CSIRO, 1989.

(6)   Chorkendorff, I.; Niemantsverdriet, J.; Wiley-VCH Verlag GmbH & Co. KGaA:1997.

(7)   Medford, A. J.; Vojvodic, A.; Hummelshøj, J. S.; Voss, J.; Abild-Pedersen, F.; Studt, F.; Bligaard, T.; Nilsson, A.; Nørskov, J. K. *J.Catal,* **2015**, *328*, 36.

(8)   Robertson, A. *Platinum Metals Rev,* **1975**, *19*, 64.

(9)   Davy, H. *Philosophical Transactions of the Royal Society of London*, **1817**, *107*, 77.

(10)   Lindström, B.; Pettersson, L. J. *CatTech,* **2003**, *7*, 130.

(11)   Arrhenius, S. *Nobel Lecture* **1903**.

(12)   Sabatier, P. *Nobel Lectures in Chemistry* **1901**, *1921*.

(13)   Van Rooij, A. *History and technology* **2005**, *21*, 345.

(14)   Klier, K. *Adv.catal,* **1982**, *31*, 243.

(15)   Little, D. M. Catalytic reforming, **1985**.

(16)   Wojciechowski, B. W.; Corma, A. Catalytic cracking:catalysts,chemistry and Kinetics **1986**.

(17)   Anderson, R. B.; Kölbel, H.; Rálek, M. *The Fischer-Tropsch Synthesis*; Academic Pr, 1984.

(18)   Feynman, R. P. *Eng sci,* **1960**, *23*, 22.

(19)   Faraday, M. *Experimental Relations of Gold (and other Metals) to Light*, 1857.

(20)   Philippot, K.; Serp, P. *Nanomaterials in Catalysis, First Edition* **2013**, 1.

(21)   Polshettiwar, V.; Asefa, T. *Nanocatalysis: Synthesis and Applications*, 2013.

(22)   Roduner, E. *Chem Soc Rev,* **2006**, *35*, 583.

(23)   Roduner, E. *Nanoscopic materials: size-dependent phenomena*; Royal Society of Chemistry, 2006.

(24)   Koga, K.; Ikeshoji, T.; Sugawara, K.-i. *Phys Rev Lett,* **2004**, *92*, 115507.

(25)   Edwards, P. P.; Johnston, R. L.; Rao, C. *Metal clusters in chemistry,* **1999**, 1454.

(26)   Vinod, C. P.; Kulkarni, G. U.; Rao, C. N. R. *Chem Phys Lett,* **1998**, *289*, 329.

(27)   Boudart, M. *Adv. Catal,* **1969**, *20*, 153.

(28)   Aben P C, P. J. C., Stouthamer B *Proc.4th International Cong Catal, Moscow* **1968**.

(29)   van Santen, R. A. *Acc Chem Res,* **2008**, *42*, 57.

(30)   Che, M.; Bennett, C. O. *Adv catal,* **1989**, *36*, 55.

(31)   Blakely, D.; Somorjai, G. *J Catal,* **1976**, *42*, 181.

(32)   Yates Jr, J. T. *J Vac Sci & Technol A,* **1995**, *13*, 1359.

(33)   Zambelli, T.; Wintterlin, J.; Trost, J.; Ertl, G. *Science,* **1996**, *273*, 1688.

(34)   Bobaru, S. C., Leiden University, 2006.

(35)   Henry, C. R. *Surf Sci Rep,* **1998**, *31*, 231.

(36)   Semagina, N.; Kiwi-Minsker, L. *Catal Rev,* **2009**, *51*, 147.

(37)   Quan, Z.; Wang, Y.; Fang, J. *Acc Chem Res,* **2012**, *46*, 191.

(38)   Haruta, M.; Tsubota, S.; Kobayashi, T.; Kageyama, H.; Genet, M. J.; Delmon, B. *J Catal,* **1993**, *144*, 175.

(39)   Valden, M.; Lai, X.; Goodman, D. W. *Science,* **1998**, *281*, 1647.

(40)   Comotti, M.; Li, W.-C.; Spliethoff, B.; Schüth, F. *J Am Chem Soc,* **2005**, *128*, 917.

(41)   Li, Y.; Liu, Q.; Shen, W. *Dalton Trans,* **2011**, *40*, 5811.

(42)   Yu, Y.; Zhang, Q.; Lu, X.; Lee, J. Y. *J.Phys Chem C,* **2010**, *114*, 11119.

(43)   Narayanan, R.; El-Sayed, M. A. *Nano Lett,* **2004**, *4*, 1343.

(44)   Bratlie, K. M.; Lee, H.; Komvopoulos, K.; Yang, P. D.; Somorjai, G. A. *Nano Lett,* **2007**, *7*, 3097.

(45)   Englisch, M.; Jentys, A.; Lercher, J. A. *J Catal,* **1997**, *166*, 25.

(46)   Telkar, M.; Rode, C.; Chaudhari, R.; Joshi, S.; Nalawade, A. *Appl Catal A,* **2004**, *273*, 11.

(47)   Ma, R.; Semagina, N. *J Phys Chem C,* **2010**, *114*, 15417.

(48)   Watt, J.; Cheong, S.; Toney, M. F.; Ingham, B.; Cookson, J.; Bishop, P. T.; Tilley, R. D. *ACS Nano,* **2009**, *4*, 396.

(49)   Park, K. H.; Jang, K.; Kim, H. J.; Son, S. U. *Angew Chem Int Ed,* **2007**, *46*, 1152.

(50)   Kundu, S.; Lau, S.; Liang, H. *J Phys Chem C,* **2009**, *113*, 5150.

(51)   Chimentao, R.; Kirm, I.; Medina, F.; Rodriguez, X.; Cesteros, Y.; Salagre, P.;Sueiras, J. *Chem Commun,* **2004**, 846.

(52)   Christopher, P.; Linic, S. *J Am Chem Soc,* **2008**, *130*, 11264.

(53)   Watt, J.; Yu, C.; Chang, S. L. Y.; Cheong, S.; Tilley, R. D. *J Am Chem Soc,* **2012**,*135*, 606.

(54)   Yin, A.-X.; Liu, W.-C.; Ke, J.; Zhu, W.; Gu, J.; Zhang, Y.-W.; Yan, C.-H. *J Am Chem Soc,* **2012**, *134*, 20479.

(55)   Scariot, M.; Silva, D. O.; Scholten, J. D.; Machado, G.; Teixeira, S. R.; Novak,M. A.; Ebeling, G.; Dupont, J. *Angew Chem Int Ed,* **2008**, *47*, 9075.

(56)   Nørskov, J. K.; Bligaard, T.; Hvolbæk, B.; Abild-Pedersen, F.; Chorkendorff, I.; Christensen, C. H. *Chem Soc Rev,* **2008**, *37*, 2163.

(57)   Taylor., H. S. *Pro R Soc Lond Ser A,* **1925**, *108*, 105.

(58)   Somorjai, G. *Wiley, New York* **1994**.

(59)   Somorjai, G. A.; Carrazza, J. *Industrial & engineering chemistry fundamentals*,**1986**, *25*, 63.

(60)   Dahl, S.; Logadottir, A.; Egeberg, R. C.; Larsen, J. H.; Chorkendorff, I.; Törnqvist, E.; Nørskov, J. K. *Phys Rev Lett,* **1999**, *83*, 1814.

(61)   Vang, R. T.; Honkala, K.; Dahl, S.; Vestergaard, E. K.; Schnadt, J.; Lægsgaard, E.; Clausen, B. S.; Nørskov, J. K.; Besenbacher, F. *Nat Mater,* **2005**, *4*, 160.

(62)   Hammer, B.; Norskov, J. *Nature,* **1995**, *376*, 238.

(63)   Hammer, B.; Nørskov, J. *Surf sci,* **1995**, *343*, 211.

(64)   Hammer, B.; Nørskov, J. K. *Adv catal,* **2000**, *45*, 71.

(65)   Nørskov, J. K.; Bligaard, T.; Logadottir, A.; Bahn, S.; Hansen, L. B.; Bollinger, M.; Bengaard, H.; Hammer, B.; Sljivancanin, Z.; Mavrikakis, M. *J.Catal,* **2002**, *209*, 275.

(66)   Munter, T. R.; Bligaard, T.; Christensen, C. H.; Nørskov, J. K. *Phys Chem Chem Phys,* **2008**, *10*, 5202.

(67)   Nilsson, A.; Pettersson, L. G.; Norskov, J. *Chemical bonding at surfaces and interfaces*; Elsevier, 2011.

(68)   Dahl, S.; Logadottir, A.; Jacobsen, C. J. H.; Nørskov, J. K. *Appl Catal A,* **2001**, *222*, 19.

(69)   Honkala, K.; Hellman, A.; Remediakis, I.; Logadottir, A.; Carlsson, A.; Dahl, S.; Christensen, C. H.; Nørskov, J. K. *Science,* **2005**, *307*, 555.

(70)   Spencer, N.; Schoonmaker, R.; Somorjai, G. *J Catal,* **1982**, *74*, 129.

(71)   Hendriksen, B. L. M.; Bobaru, S. C.; Frenken, J. W. M. *Surf Sci,* **2004**, *552*, 229.

(72)   Musselwhite, N.; Somorjai, G. A. *Top Catal,* **2013**, *56*, 1277.

(73)   Strongin, D.; Somorjai, G.; Jennings, J. *Plenum Publishing Company* **1991**.

(74)   Strongin, D.; Bare, S.; Somorjai, G. *J.Catal,* **1987**, *103*, 289.

(75)   Bratlie, K. M.; Flores, L. D.; Somorjai, G. A. *J Phys Chem B,* **2006**, *110*, 10051.

(76)   Bratlie, K. M.; Kliewer, C. J.; Somorjai, G. A. *J Phys Chem B,* **2006**, *110*, 17925.

(77)   Bratlie, K. M.; Montano, M. O.; Flores, L. D.; Paajanen, M.; Somorjai, G. A. *J Am Chem Soc,* **2006**, *128*, 12810.

(78)   Mavrikakis, M.; Stoltze, P.; Nørskov, J. K. *Catal Lett,* **2000**, *64*, 101.

(79)   Vinod, C. P.; Niemantsverdriet Hans, J. W.; Nieuwenhuys, B. E. *Appl Catal A,***2005**, *291*, 93.

(80)   Carabineiro, S. A. C.; Nieuwenhuys, B. E. *Surf Sci,* **2003**, *532–535*, 87.

(81)   Carabineiro, S. C.; Nieuwenhuys, B. *Gold Bull,* **2009**, *42*, 288.

(82)   Carabineiro, S. C.; Nieuwenhuys, B. *Gold Bull,* **2010**, *43*, 252.

(83)   Pal, J.; Pal, T. *Nanoscale,* **2015**, *7*, 14159.

(84)   Zhou, Z.-Y.; Tian, N.; Li, J.-T.; Broadwell, I.; Sun, S.-G. *Chem Soc Rev,* **2011**, *40*, 4167.

(85)   Wang, Z. *J Phys Chem B,* **2000**, *104*, 1153.

(86)   Yang, C.-W.; Chanda, K.; Lin, P.-H.; Wang, Y.-N.; Liao, C.-W.; Huang, M. H. *J Am Chem Soc,* **2011**, *133*, 19993.

(87)   Zhang, Q.; Xu, J.; Yan, D.; Li, S.; Lu, J.; Cao, X.; Wang, B. *Catal Sci& Technol,* **2013**, *3*, 2016.

(88)   Wang, R.; He, H.; Liu, L.-C.; Dai, H.-X.; Zhao, Z. *Catal Sci Technol,* **2012**, *2*, 575.

(89)   Xu, R.; Wang, D.; Zhang, J.; Li, Y. *Chem An Asian J,* **2006**, *1*, 888.

(90)   Xu, Z.-N.; Sun, J.; Lin, C.-S.; Jiang, X.-M.; Chen, Q.-S.; Peng, S.-Y.; Wang, M.-S.; Guo, G.-C. *ACS Catal,* **2012**, *3*, 118.

(91)   Crespo-Quesada, M.; Yarulin, A.; Jin, M.; Xia, Y.; Kiwi-Minsker, L. *J Am Chem Soc,* **2011**, *133*, 12787.

(92)   Kiwi-Minsker, L.; Crespo-Quesada, M. *Top Catal,* **2012**, *55*, 486.

(93)   Lu, C.-L.; Prasad, K. S.; Wu, H.-L.; Ho, J.-a. A.; Huang, M. H. *J Am Chem Soc,* **2010**, *132*, 14546.

(94)   Wang, J.; Gong, J.; Xiong, Y.; Yang, J.; Gao, Y.; Liu, Y.; Lu, X.; Tang, Z. *Chem.Commun.* **2011**, *47*, 6894.

(95)   Zhang, J.; Feng, C.; Deng, Y.; Liu, L.; Wu, Y.; Shen, B.; Zhong, C.; Hu, W. *Chem Mater,* **2014**, *26*, 1213.

(96)   Yu, Y.; Zhang, Q.; Liu, B.; Lee, J. Y. *J Am Chem Soc,* **2010**, *132*, 18258.

(97)   Van Hove, M.; Somorjai, G. *Surf Sci,* **1980**, *92*, 489.

(98)   Tian, N.; Zhou, Z.-Y.; Sun, S.-G.; Ding, Y.; Wang, Z. L. *Science,* **2007**, *316*, 732.

(99)   Yu, T.; Kim, D. Y.; Zhang, H.; Xia, Y. *Angew Chem Int Ed,* **2011**, *50*, 2773.

(100) Lu, F.; Zhang, Y.; Zhang, L.; Zhang, Y.; Wang, J. X.; Adzic, R. R.; Stach, E. A.;Gang, O. *J Am Chem Soc,* **2011**, *133*, 18074.

(101) Tian, N.; Zhou, Z. Y.; Yu, N. F.; Wang, L. Y.; Sun, S. G. *J Am Chem Soc,* **2010**,*132*, 7580.

(102) Tian, N.; Zhou, Z.-Y.; Sun, S.-G. *Chem Commun,* **2009**, *0*, 1502.

(103) Jin, M.; Zhang, H.; Xie, Z.; Xia, Y. *Angew Chem Int Ed,* **2011**, *50*, 7850.

(104) Ma, Y.; Kuang, Q.; Jiang, Z.; Xie, Z.; Huang, R.; Zheng, L. *Angew Chem* **2008**, *120*, 9033.

(105) Zhou, Z.-Y.; Tian, N.; Huang, Z.-Z.; Chen, D.-J.; Sun, S.-G. *Faraday discuss,* **2009**, *140*, 81.

(106) Tian, N.; Zhou, Z.-Y.; Sun, S.-G. *J Phys Chem C,* **2008**, *112*, 19801.

(107)   Huang, X.; Zhao, Z.; Fan, J.; Tan, Y.; Zheng, N. *J Am Chem Soc,* **2011**, *133*,4718.

(108)   Maksimuk, S.; Teng, X.; Yang, H. *Phys Chem Chem Phys,* **2006**, *8*, 4660.

(109)   Hong, J. W.; Lee, S.-U.; Lee, Y. W.; Han, S. W. *J Am Chem Soc,* **2012**, *134*, 4565.

(110)   Ming, T.; Feng, W.; Tang, Q.; Wang, F.; Sun, L.; Wang, J.; Yan, C. *J Am Chem Soc,* **2009**, *131*, 16350.

(111)   Jin, M.; Zhang, H.; Xie, Z.; Xia, Y. *Angew Chem Int Ed,* **2011**, *50*, 7850.

(112)   Yu, Y.; Zhang, Q. B.; Xie, J. P.; Lu, X. M.; Lee, J. Y. *Nanoscale,* **2011**, *3*, 1497.

(113)   Eustis, S.; El-Sayed, M. A. *Chem Soc Rev,* **2006**, *35*, 209.

(114)   West, A. R. *Solid state chemistry and its applications*; John Wiley & Sons, 2007.

(115)   Hirsch, P. B.; Howie, A.; Nicholson, R.; Pashley, D.; Whelan, M. J. *1965, 549 P.butterworth inc., 7300 pearl street, washington, d. c. 20014* **1966**.

(116)   Williams, D. B.; Carter, C. B. *New York, NY* **1996**.

(117)   Berne, B. J.; Pecora, R. *Dynamic light scattering: with applications to chemistry,biology, and physics*; Courier Corporation, 1976.

(118)   Hollas, J. M. *Modern spectroscopy*; John Wiley & Sons, 2004.

Chapter-2
Oxidation catalysis by large trisoctahedral Au nanoparticles: Probing the role of step atoms, interfaces and confinement effects. [#]

2.1. Introduction

Gold is a catalytically inert material in the bulk form and this inertness has been explained in terms of d-band model by Norksov and co-workers.[1] When it is finely divided as small particles with size less than 5 nm, it is demonstrated to show excellent activity towards various chemical reactions.[2-3] The major factors for this enhanced activity includes the size of the nanoparticles,[4] support effect,[5] electronic modifications,[6] charge transfer from support to metal,[7] presence of under co-ordinated atoms on the surface, presence of metal-oxide interface[4,8-9] and stability of the catalyst towards sintering.[10] The enhanced activity of a nanoparticle surface can be attributed to the active sites proposed by Taylor in 1925[11] which can change the course of chemical reaction. The quantification of such sites is challenging and is an area of considerable research interest. The concept has been validated by several surface science studies. One of the earlier works by Dahl and co workers with molecular beam experiments and DFT calculations proved that the dissociation of N_2 on a stepped Ru surface is 9 times higher than on a terrace site.[12] The surface science studies on Au {310} surface showed that this surface was capable of decomposing small molecules like methanol and NO.[13] A detailed calculations by Norskov and co workers showed that activation of O_2 and CO is more favourable on step sites relative to a terrace sites.[14] The developments made in the synthesis strategies have opened up a way for validating the reactivity of such sites (step sites) on a nanoparticle surface.[15]

Nanoparticles which expose high index facets possess atoms of under coordination and such particles can be model testing ground for validating the hypothesis of such active sites. To probe the role of under coordinated atoms, a high index faceted Au nanostructure namely Trisoctahedron was chosen which was anticipated to potentially activate molecules. A trisoctahedron can be considered as an octahedron with each of its facet capped by triangular bipyramid. This polyhedron exposes 24 high index facets having miller index {hhl} where h > l. Synthesis and high resolution TEM characterization of trisoctahedral nanoparticles of gold reported recently have shown that these particles have periodic (110) step sites bound on {221}, {331} and or {441} facets.[16] The catalytic performance of Au nanoparticles also depends on the strong metal-support

interaction where a reducible support was found to enhance the chemical activity of Au nanoparticles towards CO oxidation even at low temperature.[8] The concept of active oxide-metal perimeter and its effect on the activity of gold based catalysis has been demonstrated by several research groups and the presence of metal-oxide interface is found to be an essential criterion for the enhanced activity. The studies focusing on the controlled formation of Au-oxide interface has been pursued to understand the role of metal-oxide interface. Such systems are generally called inverse catalyst systems. A schematic representation of real and inverse catalyst system is shown in Figure 2.1.
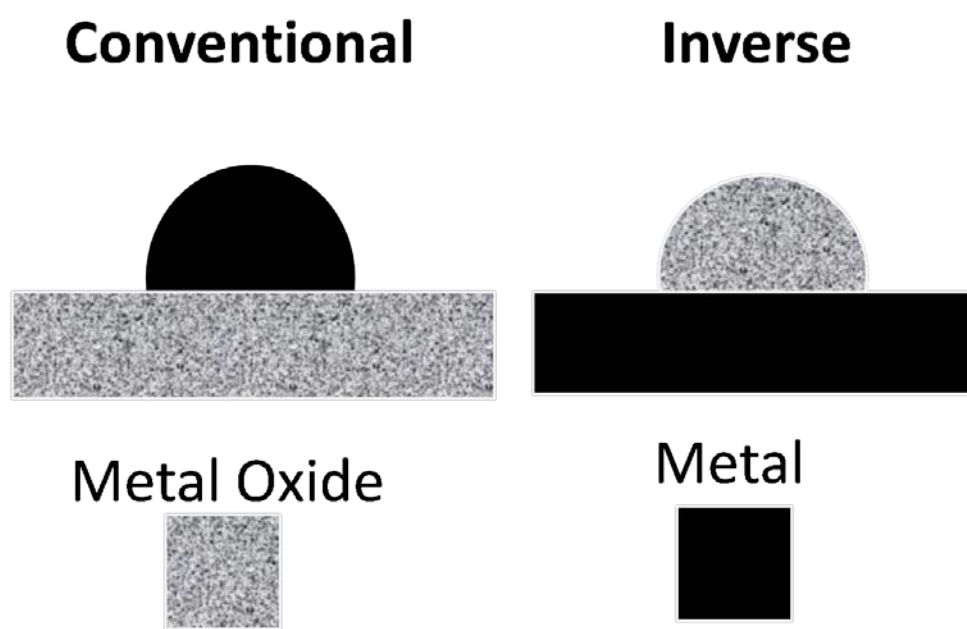
Figure 2.1: The schematic representation of a conventional and inverse catalyst system.

Guczi and co-workers have studied model systems like gold/iron oxide and gold/titania interface on SiO_2/Si (100).[17] There are some literature reports on the study of the effect of oxide decoration on thin films. Weiss et al created CeO_x/Pt (111) interface and showed that the CeO_x nanoislands have great impact on the catalytic activity of Pt (111) surface.[18] Rodriguez and co-workers have demonstrated that Au (111) when decorated with CeO_x and TiO_x nanoislands showed enhanced catalytic activity for WGS reaction and the activity was found to depend on oxide coverage.[19] The interaction of carbon monoxide and oxygen with inverse titania/Au (111) model catalyst was studied and found that CO do not adsorb on neither Au nor titanium dioxide at 200 K but on

Au-oxide interface.[20] The key role of gold-support interface in CO oxidation was clearly shown experimentally for Au/CeO$_2$ system, by the design of a set of ceria "nanotowers" with the same surface area for Au and CeO$_2$ but with different interfacial lengths.[21] Another interesting class of "nano"gold is nanoporous Au which are unsupported with highly interconnected gold ligaments and pores of the order of few tenths of nanometer, typically of 30-40 nm.[22] They are stable and thus are not prone to immediate deactivation. Nanoporous Au is proved to be active for many reactions and the activity is mainly attributed to the presence of residual Ag left behind after the dealloying process of Au-Ag alloy.[23] Baumer et al recently demonstrated that the activity and stability of gold catalyst system can be dramatically improved by reversing the classical situation in a catalytic system, i.e. by decorating high surface area nanoporous Au with oxides like PrO$_x$ and TiO$_2$.[24] Biener et al reported the atomic layer deposition of Al$_2$O$_3$ and TiO$_2$ on the inner surface of nanoporous gold which showed enhanced stability and catalytic activity.[25] Even though gold shows high size dependency towards chemical reactions, bulk gold was recently demonstrated to catalyse aerobic oxidation of alcohols,[26] amines and isocyanides[27] and aqueous phase oxidation of CO in presence of NaOH.[28]

Sintering, which is a major hindrance in gold based catalysts and search for stable and active catalysts have led to the synthesis of sinter resistant gold nanoparticles. Various strategies like confinement of nanoparticles in mesoporous materials and on oxide supports were adopted. For instance, Dai and co-workers presented a unique deposition precipitation method for the synthesis of mesoporous silica supported gold catalysts by using cationic gold precursors. These mesporous supports have uniform nanopores which can confine nanoparticles and possess thick wall structures and are thermally stable. The Au supported mesoporous silica catalyst were found to be stable at 500 °C with particle size between 3.7 and 3.9 nm.[29] Another way to prevent sintering is to encapsulate nanoparticles inside porous shells as reported by Somorjai and co-workers etc.[30] They were successful in synthesising core-shell structured Pt@mSiO$_2$ nanoparticles as high-temperature model catalysts. The Pt@mSiO$_2$ nanoparticles maintained their core-shell configurations up to 750 °C and exhibited high catalytic activity for ethylene hydrogenation and CO oxidation. In another report, Schuth et al proved that the isolation of nanoparticles by hollow sphere encapsulation does indeed allow stabilization of the

catalyst against sintering by developing high temperature (800 °C) stable Au @ ZrO$_2$ catalysts.[31] Several reports suggest that encapsulating metal nanoparticles inside a porous shell can prevent the sintering and thereby the deactivation of catalyst even after several cycles of reaction.[10,32]

Thus to garner insights to the reactivity of under coordinated atoms, to address size dependency, Trisoctahedral (TOH) Au nanoparticles were synthesised with different sizes above the regime (optimum being 3-5 nm) where gold is found to be active. The role of active-metal oxide interfaces were studied by decorating nano oxides on TOH Au nanoparticles. These decorated TOH -nano-oxide systems were also encapsulated inside silica shell and tested for CO oxidation reaction to probe the role of confinement effects.

2.2. Experimental Section

2.2.1. Reagents

HAuCl$_4$.3H$_2$O (99.9%), (Sigma Aldrich), Cetyltrimethylammonium bromide, CTAB (98%), Ascorbic Acid, AA (99%) (Spectrochem), Ethanol, Titanium Isopropoxide (Merck), Cetyl trimethylammonium chloride, CTAC (96%) (Alfa Aesar), H$_2$SO$_4$ (Merck), Anatase TiO$_2$ and DarcoG60, (Sigma Aldrich) were purchased and used as received. Ultrapure Millipore water was used in all experiments.

2.2.2. Synthesis of trisoctahedral (TOH) gold NCs

The synthesis of trisoctahedral nanoparticles of size 45 nm, 70 nm, 110 nm were carried out using a modified seed mediated procedure reported in literature.[16] In a typical synthesis, 20 mM 46 µL HAuCl$_4$ solution was added to 75 mM 7 mL CTAB solution. Then 420 µL of ice cold 0.01 M NaBH$_4$ was injected rapidly into the mixture under vigorous stirring resulting in a brown solution. Stirring continued to remove excess NaBH$_4$. To a solution of 125 µL HAuCl$_4$ (20 mM) mixed with 9 mL of CTAC (22 mM) was added 3 mL of 38.8 mM ascorbic acid and 50 µL of diluted (100 fold) seed solution and mixed thoroughly producing 45 nm TOH gold NCS. To prepare 70 nm TOH gold particles, 6 mL of as prepared 45 nm TOH gold colloid was added as seed to 9 mL of CTAC (22 mM) followed by the addition of 3 mL of AA (38.8 mM) and 125 µL of 20 mM HAuCl$_4$ solution. To prepare 110 nm TOH gold particles, 2 mL of the as prepared 45 nm TOH gold NCS were added as

seed to 9 mL of 22 mM CTAC followed by the addition of 3 mL of AA and 125 µL of 20 mM $HAuCl_4$ solution. The as synthesized TOH gold NCS were supported on SBA-15 and TiO_2 by the following procedure. Typically, 12.5 mL of 45 nm TOH gold colloidal solution was added to 50 mg of SBA-15 and acidified by sulphuric acid (pH maintained at 1) to obtain 1 wt% of the catalyst. The slurry was stirred for 2 h after which it was filtered, washed (till mother liquor becomes neutral), dried at 120 ºC for 4 h followed by calcination at 300 °C for 3 h. The H_2 treatment was done at 400 °C for 1 h at flow rate of 12 ml/min with ramping rate of 2 °C/min. To obtain supported TOH (110 nm) catalyst 14 mL of the sol was added to the 50 mg of the SBA-15. By this way the metal loading was kept at 1 wt%. The same procedure was used for supporting TOH Au on TiO_2.

2.2.3. Synthesis of nanorods, nanotriangles and nanocubes

Seed synthesis

About 0.6 mL of $NaBH_4$ was added to a mixture of 0.25 mL of 0.01 M $HAuCl_4$ and 7.5 mL CTAB in a 200 mL standard flask and mixed by rapid inversion for two minutes. The resultant seed solution was kept for one hour.

Synthesis of nanoparticles of nanorods, nanotriangles and nanocubes

About 12.8 mL of 0.1 M CTAB, 1.6 mL of 0.01 M $HAuCl_4$ and 7.6 mL of 0.1 M ascorbic acid were added sequentially into 64 mL deionised water in a 200 mL flask. About 40 µL of the seed solution was mixed by gentle inversion for 10 seconds and kept overnight. The solution centrifuged at 10,000 rpm for 10 minutes and was used for TEM analysis and for supporting with titania. The gold nanoparticles of different shapes were supported on titania following the same procedure used for supporting trisoctahedral nanoparticles.

2.2.4. Synthesis of Inverse catalyst

Trisoctahedral (TOH) Au nanoparticles were synthesised as discussed above. To the colloidal solution required amount of titanium isopropoxide (to obtain 4 to 10 wt% with respect to gold) dissolved in ethanol was added and stirred magnetically for 30 minutes followed by the addition of support (SBA-15 or titania). In a typical synthesis of 5 wt% titania doped inverse catalyst, 0.63 µL of titanium isopropoxide was dissolved in 3 mL of ethanol and then added to 18 mL of TOH Au colloidal solution which was then stirred for 30 minutes followed by the addition of 72 mg of SBA-15. The solution was acidified to a pH of ~ 1-2. After 2 h of stirring, the slurry

was washed with water till the mother liquor becomes neutral. The slurry was then centrifuged and dried at 80 °C till water is evaporated and calcined at 600 °C for 5 h. The above procedure resulted in 5 wt% titania doped TOH Au/SBA-15 (1 wt%). To obtain titania doped TOH Au/TiO$_2$ instead of SBA-15, titania was added in the synthesis stage. The titania doped TOH Au nanoparticles supported on SBA-15 and titania catalysts were named as ATS and ATT respectively These catalysts were pre-treated under mild conditions in H$_2$ atmosphere at 400 °C for 1 h prior to the CO oxidation reaction.

2.2.5. Synthesis of silica encapsulated TOH gold nanoparticle, TOH Au@ SiO$_2$

The TOH Au colloid was encapsulated with silica by following the route of Graf et al and Schuth et al.[31,33] Briefly, synthesised TOH gold colloid was centrifuged and the supernatant was removed. The volume of the concentrated colloid was then adjusted to 6 mL by dilution with water. The colloid was vigorously stirred for 5 min, followed by the addition of 500 µL of ammonia premixed with 10 mL ethanol. Immediately afterwards, a solution of 700 µL Tetraethyl orthosilicate (TEOS) in 8 mL of ethanol was added. The reaction mixture was stirred for 12 h at room temperature. The resultant colloid was centrifuged (10000 rpm; 10 min) and washed twice with water and twice with absolute ethanol to remove the excess of capping agents. The catalyst Au@SiO$_2$ (AS) was obtained and calcined at 500 °C for 5 h and reduced in H$_2$ atmosphere at 400 °C for 1 h.

2.2.6. Synthesis of TOH gold nanoparticle decorated with ceria and encapsulated in silica spheres, Au/CeO$_2$@SiO$_2$

The TOH colloid was made in 5 batches containing 3.6 mg of Au and the synthesised TOH gold colloid was centrifuged and the supernatant was removed and washed thoroughly with ethanol to remove excess surfactants. The volume of the concentrated colloid was then adjusted to 6 mL by dilution with water. The colloid was vigorously stirred for 5 min, 55 µL of aqueous solution of 20 mM Ce(NO$_3$)$_3$ was added to the Au sols at 60 °C and stirred for 4 h so as to obtain ceria decoration. After this, the colloid was centrifuged and the volume of the concentrated colloid was then adjusted to 6 mL by dilution with water. Further, silica encapsulation was done by the above procedure. Washed, dried catalyst, TOH gold decorated with ceria encapsulated in silica, Au/CeO$_2$@SiO$_2$ was calcined at 500 °C for 5 h and reduced in H$_2$ atmosphere at 400 °C for 1 h.

2.2.7. Synthesis of TOH gold nanoparticle decorated with titania and encapsulated in silica spheres, Au/TiO$_2$@SiO$_2$

The TOH colloid was made in 5 batches containing 3.6 mg of Au and the synthesised TOH gold colloid was centrifuged and the supernatant was removed. The volume of the concentrated colloid was then adjusted to 6 mL by dilution with water. The colloid was vigorously stirred for 5 min, and 675 µL Titanium isopropoxide solution in 2 mL of ethanol was added to Au sols at room temperature and stirred for 4 h so as to obtain TiO$_2$ decorated samples. After this, the colloid was centrifuged and the volume of the concentrated colloid was then adjusted to 6 mL by dilution with water. Further, silica encapsulation was done by the above procedure. Washed, dried catalyst, TOH gold decorated with ceria encapsulated in silica, Au/TiO$_2$@SiO$_2$ was calcined at 500 °C for 5 h and reduced in H$_2$ atmosphere at 400 °C for 1 h. The loading of oxide was controlled to 1, 3, 5, 7 wt% by varying the amount of precursors in the solution.

2.3. Characterization techniques

X-ray Diffraction Analysis: Powder X-ray diffraction (XRD) was measured on a PANalytical X'pert Pro dual goniometer diffractometer working under 40 keV and 30 mA. The Cu Kα (1.5418 Å) radiation was used with a Ni filter.

UV-Visible Spectroscopy: UV/Vis spectra were acquired by using a Varian Cary 50 Conc UV/Vis spectrophotometer with a dual beam source.

Transmission Electron Microscopy (TEM): TEM images were recorded by FEI Tecnai TF-30 and TF-20 electron microscope, operating at 300 keV and 200 keV.

The Inductively coupled Plasma analysis was done using Spectro Arcos ICP-OES.

FTIR spectroscopy analysis of the pelletized samples was performed with a Bruker Tensor 27 FTIR spectrophotometer with a DTGS detector at room temperatures by using KBr as an internal standard

Nitrogen adsorption/desorption isotherms were collected by using Autosorb 1C Quantachrome, USA. The program consisted of both adsorption and desorption branches and typically ran at 196 °C after samples were

degassed at 250 °C for 3 h. The specific surface area was calculated by the BET model at a relative pressure of $P/P_0 = 0.06$–0.3. The total pore volume was estimated from the uptake of the adsorbate at a relative pressure of $P/P_0 = 0.99$.

2.4. Catalyst Testing: CO oxidation

The catalytic activity of TOH NCS for CO oxidation was measured in a fixed bed reactor under atmospheric pressure using 100 mg catalyst. The total flow rate was 50 ml/min with a ratio of (1:5:19 $CO:O_2:N_2$) with a temperature range of 300 K to 573 K. The calculated GHSV was 30000 $cm^3/g_{cat}/h$. The reactor was placed in a tubular furnace and temperature of the furnace controlled by Radix6400 temperature controller. The catalyst bed temperature was measured by a K-type thermocouple. The effluent gases were analysed online by gas chromatograph equipped with online gas sampling valve and a TCD detector. The activity was examined by looking at the CO conversion.

2.5. Results and Discussions

2.5.1. Trisoctahedral Au nanoparticles

a. Transmission Electron Microscopy
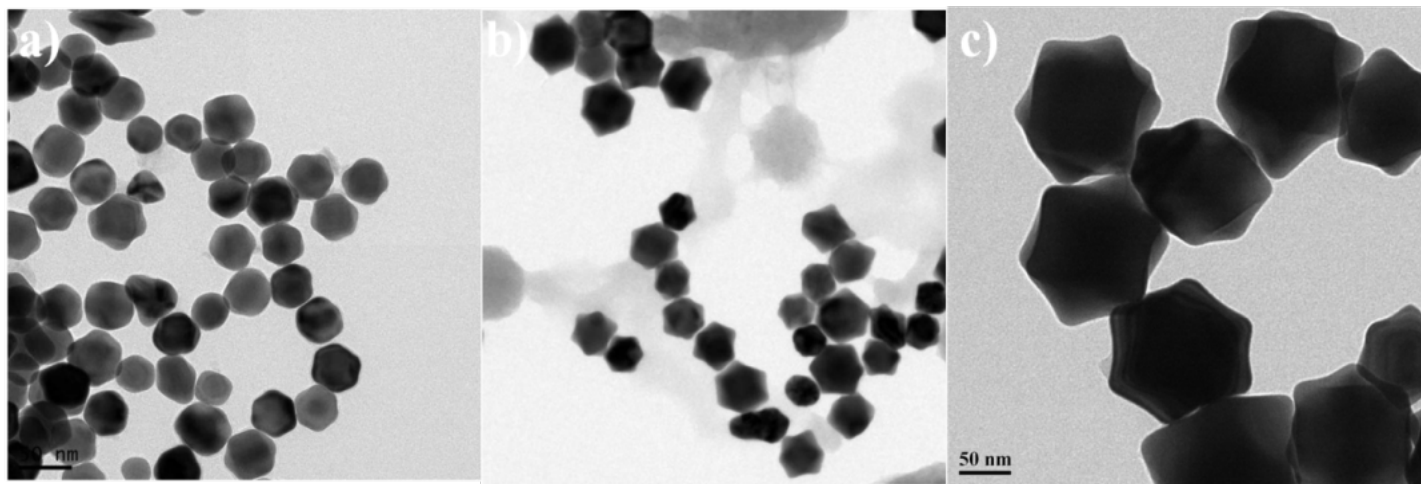
Figure 2.2: TEM image of trisoctahedral (TOH) gold nanoparticles of different sizes a) ~ 45 nm b) ~ 70 nm and c) ~ 110 nm.

The synthesis of trisoctahedral nanoparticles of size 45 nm, 70 nm and 110 nm were carried using a seed mediated procedure reported in literature.[34] Figure 2.2 shows the TEM image trisoctahedral particles of different sizes obtained during the synthesis. The histogram showed that the particles falls in a narrow size distribution (see Figure 2.3).
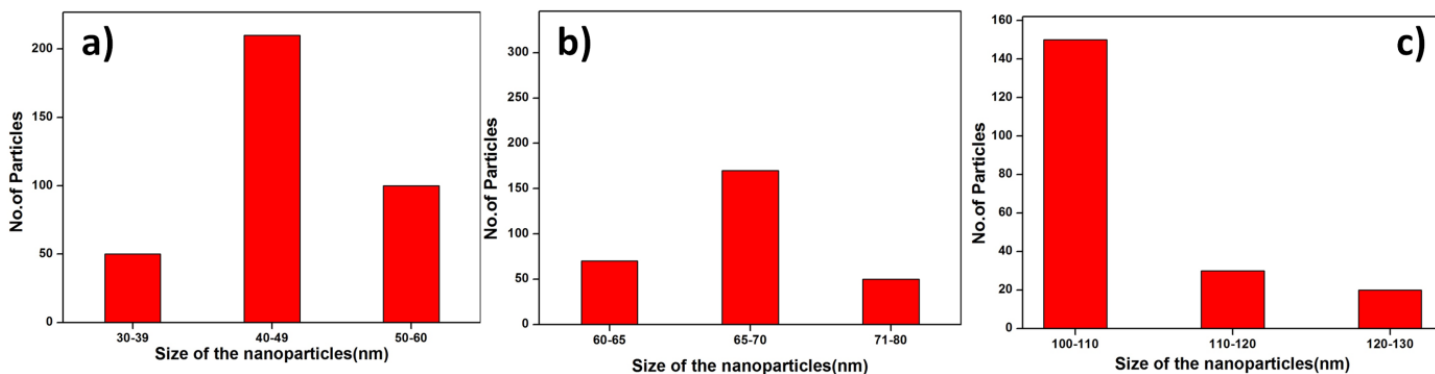
Figure 2.3: The histograms showing the particle size distribution of the as synthesised TOH nanopartilces a) 45 nm b) 70 nm and c) 110 nm.

The morphology of the particles obtained during our synthesis clearly showed the reproducibility of the procedure which was adopted from the literature and also the availability of the defect structure on the particle as shown in Figure 2.4. The line profile analysis shown in Figure 2.4b gave a d spacing of 0.48 nm which corresponds to 3 atom wide terrace.
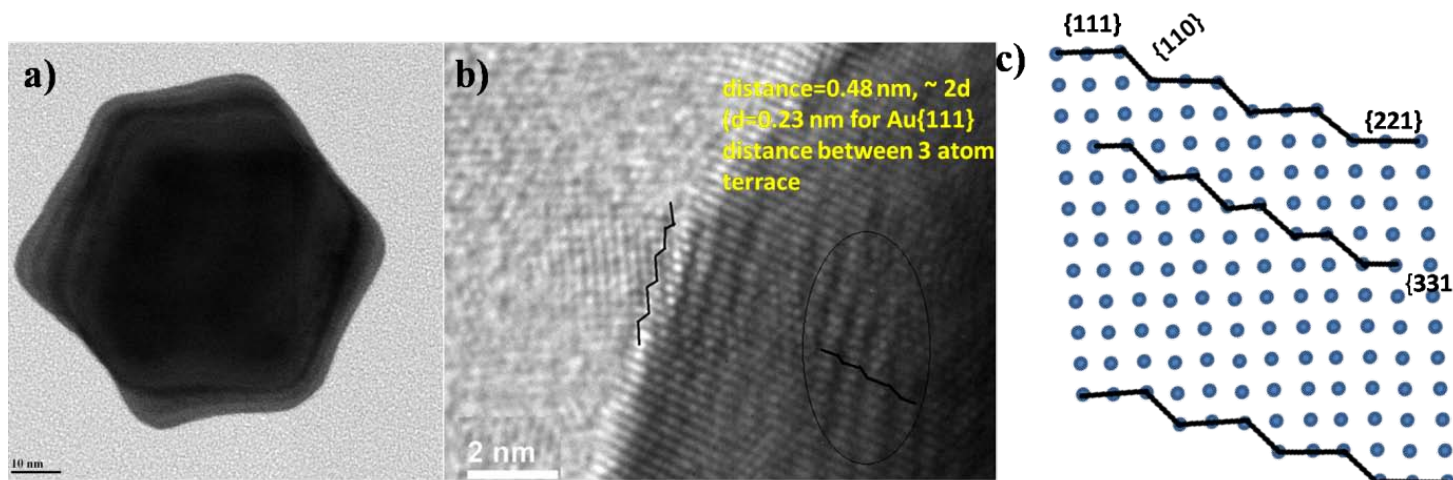
Figure 2.4: a) TEM image of a) single TOH Au b) HRTEM image showing the step terrace geometry along the edge of titania decorated sample, the line profile on the surface of TOH Au nanoparticle with a distance of 0.48

nm which corresponds to the distance between 3 atom wide terrace c) atomic model of {221} and {331} high index facets.

b. X-ray diffraction
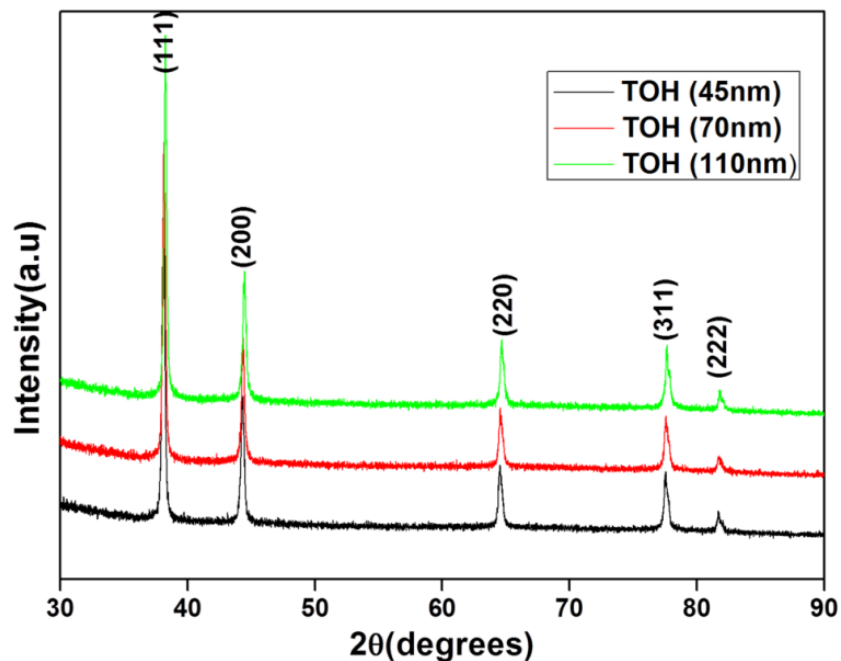
Figure 2.5: XRD pattern of as synthesised TOH nanoparticles showing the reflections of fcc Au crystal lattice.

Figure 2.5 shows the XRD reflections from pristine TOH Au nanoparticles of different sizes. The characteristic reflections from Au {111}, {200}, {311} and {220} planes were observed. The crystallite size calculated by Debye Scherrer formula gave an average values of 42 nm for TOH (45 nm), 62 nm for TOH (70 nm). The sizes for TOH 110 nm are not reported here as the XRD peaks were very sharp and were not used for particle size calculation.

c. UV-Visible Spectroscopy

The UV-Vis spectrum obtained during the synthesis of trisoctahedral particles showed strong surface plasmon bands at 552 nm (45 nm), 570 nm (70 nm) and 590 nm (110 nm) respectively as shown in Figure 2.6. It is clear that an increase in the nanoparticle size results in a red shift in the plasmon peak.
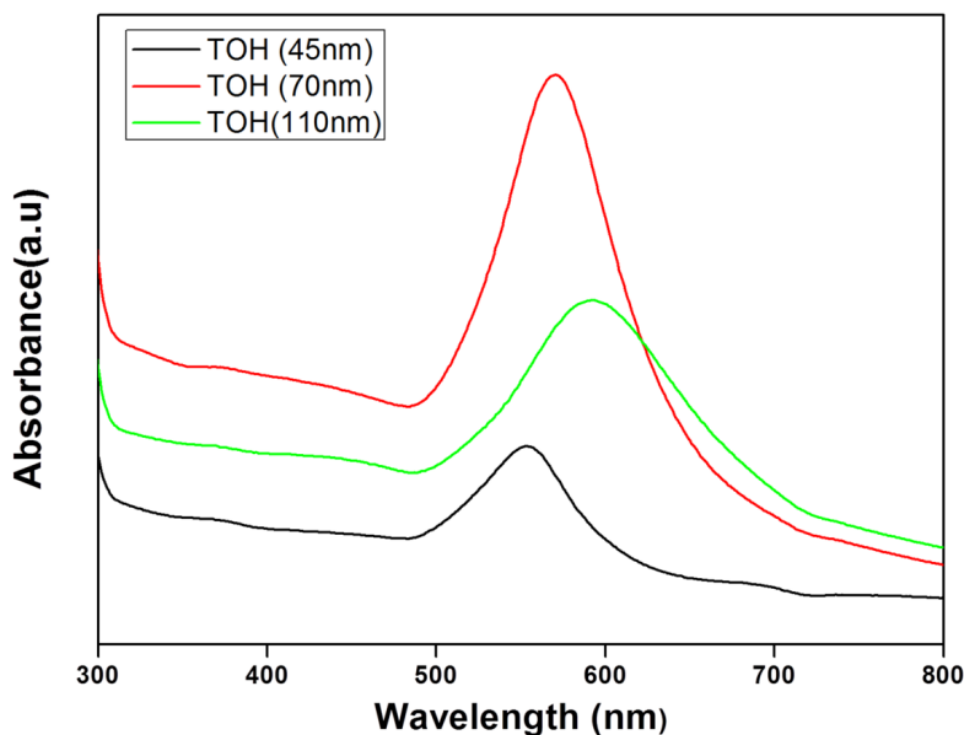
Figure 2.6: The UV-Vis spectrum obtained during synthesis of 45 nm, 70 nm and 110 nm TOH nanoparticles.

2.5.2. Supported TOH Au nanoparticles: Real and Inverse systems

a. Transmission Electron Microscopy
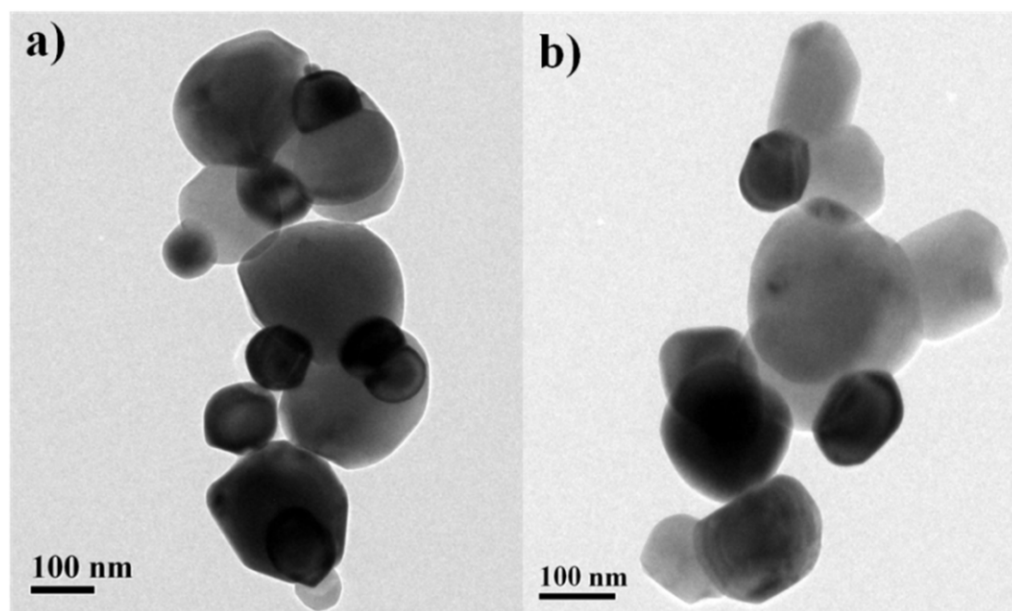
Figure 2.7: The TEM images of a) TOH (110 nm)/TiO$_2$ and the b) inverse ATT-5 wt% (70 nm) after calcination and reduction step which shows that the particle morphology is retained.

For catalytic applications, these nanoparticles were supported on different oxides like TiO_2 and SBA-15 and tested for CO oxidation reaction. The TEM image in Figure 2.7 shows that the particle morphology was more or less retained after supporting. Furthermore, to probe the role of interfaces, inverse catalyst (i.e. titania decorated on TOH Au nanocrystals) were synthesized. The titania doping was varied from 4-10 wt% with respect to gold. These titania doped gold nanoparticles were then supported on TiO_2 (see Figure 2.7b) and SBA-15 and thoroughly characterized.
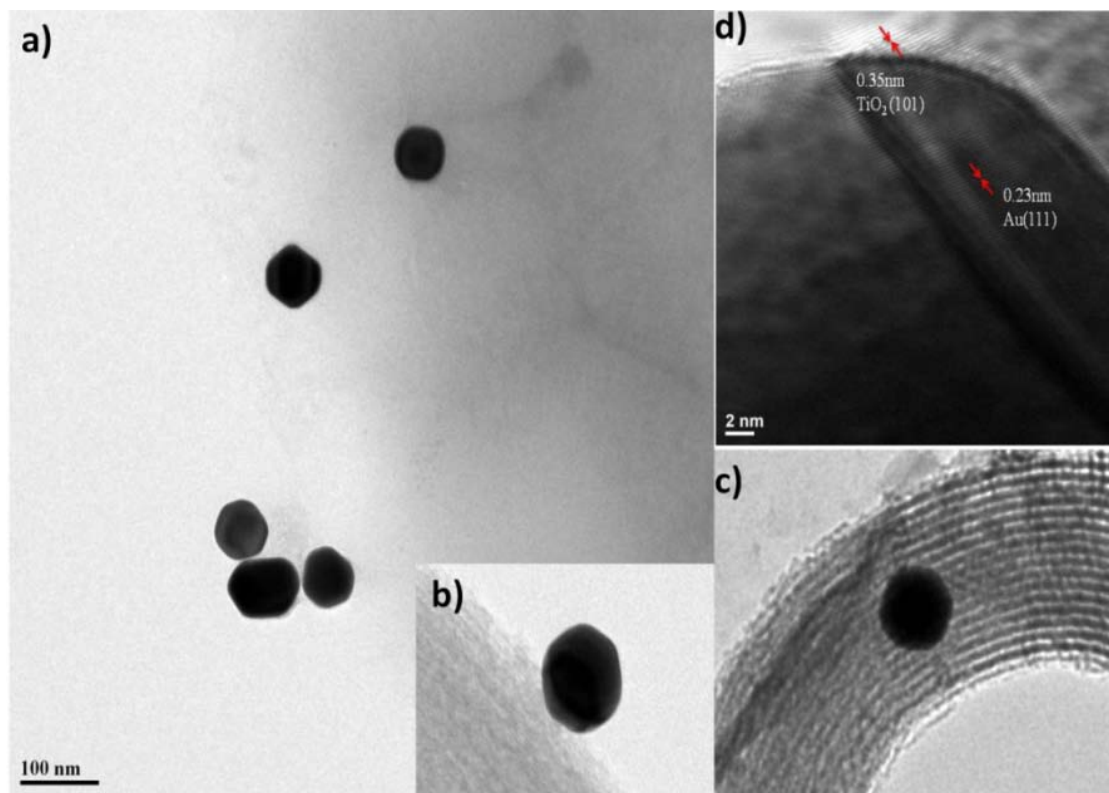
Figure 2.8: a) The TEM image of ATS (45 nm) 5 wt% catalyst after calcination at 600 °C, b) and c) TEM image of a single TOH Au after treatment with H_2 showing the retention of morphology and d) HRTEM image of a single Au nanocrystal decorated with TiO_2 showing the presence of anatase TiO_2 lattice.

The TEM image shown in Figure 2.8 represents ATS (45 nm) 5 wt% where TOH gold is decorated with titania and supported on SBA-15 and calcined at 600 °C. The HRTEM image shown in Figure 2.8d gave evidence for interface formed by TiO_x with TOH gold. The d spacing of this titania layer was found to be 0.35 nm which corresponds to the (101) plane of anatase phase (JCPDS-21-1272).

b. X-ray diffraction

In Figure 2.9a the XRD reflections from anatase supported TOH Au is shown. The reflection from anatase TiO_2 and the inset shows the reflection from Au. The diffractions were very weak and this can be attributed to the lesser loading in the catalyst. The XRD pattern collected from inverse ATS (45 nm) 5 wt% catalyst also showed the presence of anatase phase along with the reflections of TOH Au as shown in Figure 2.9b.
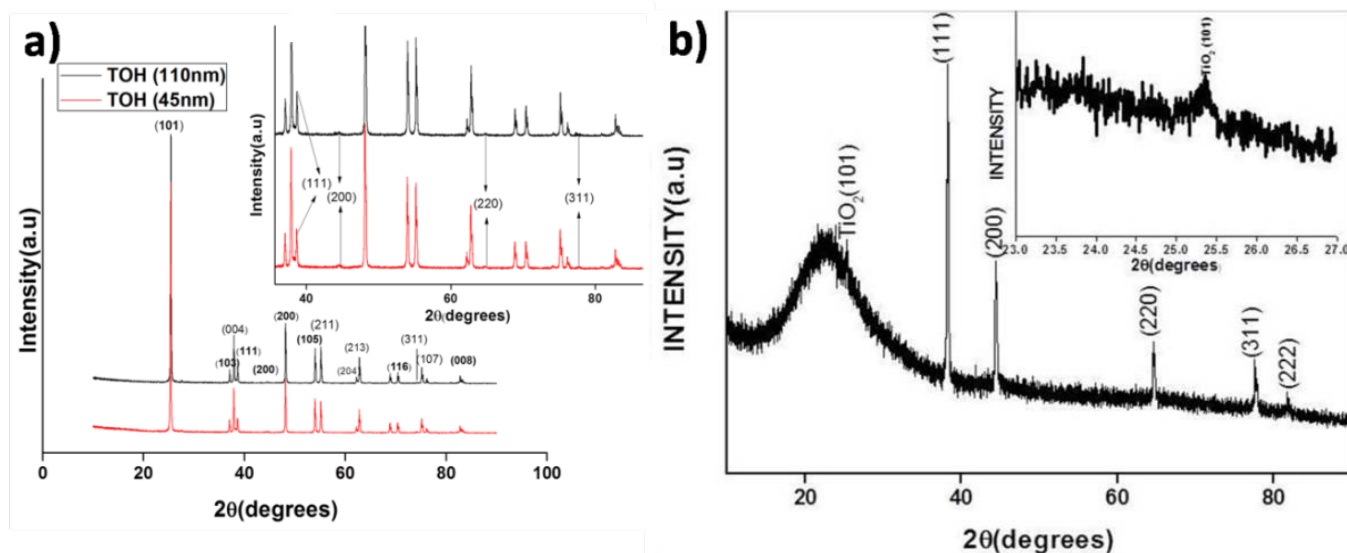
Figure 2.9: XRD pattern of a) TOH nanoparticles supported on anatase TiO_2 and the inset shows the reflection of Au marked by arrows and b) AST (45 nm) 5 wt% (inverse system) which clearly shows the presence of anatase phase along with the reflections of TOH Au.

2.5.3. Encapsulated system

a. Transmission Electron Microscopy

A trisoctahedral Au nanoparticle can be viewed as an octahedron whose each facet is capped by a triangular pyramid.[16] These nanoparticles were decorated with TiO_2 or CeO_2 and were then encapsulated in silica to prevent particle mobility. In Figure 2.10a the representative TEM image of TiO_2 decorated and silica encapsulated TOH Au catalyst is shown. The magnified image in Figure 2.10b shows a TOH Au core and a silica shell with thickness of around 180 nm. This gives a clear indication that the trisoctahedral morphology is retained even after silica encapsulation followed by calcination reduction steps involved in catalyst synthesis.

The HRTEM image of the titania and ceria decorated TOH Au nanoparticle is shown in Figure 2.10c and 2.10d. The image clearly showed that the active metal-oxide is formed between Au and nano oxide. In Figure 2.10c and 2.10d the lattice fringes of titania and ceria with d spacing of 0.35 nm {JCPDS 86-1157} and 0.31 nm {JCPDS 81-0792} respectively is shown. The close proximity of TOH Au nanoparticles with titania and ceria creating a strong interface is also visible from the TEM image.
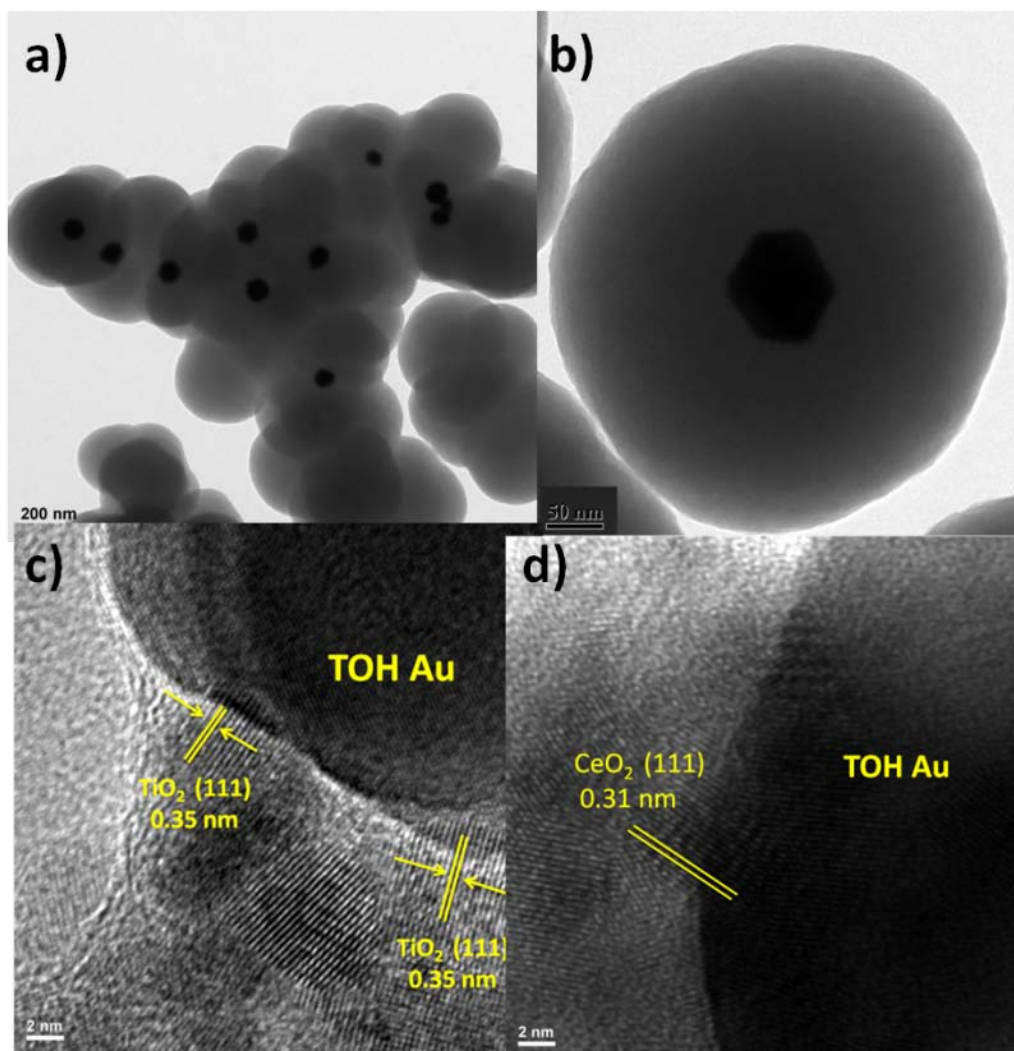
Figure 2.10: The TEM of a) low and b) high magnification images of TiO_2-Au@SiO_2 catalyst c) and d) high resolution images of TOH Au decorated with TiO_2 and CeO_2 respectively.

b. X-ray diffraction
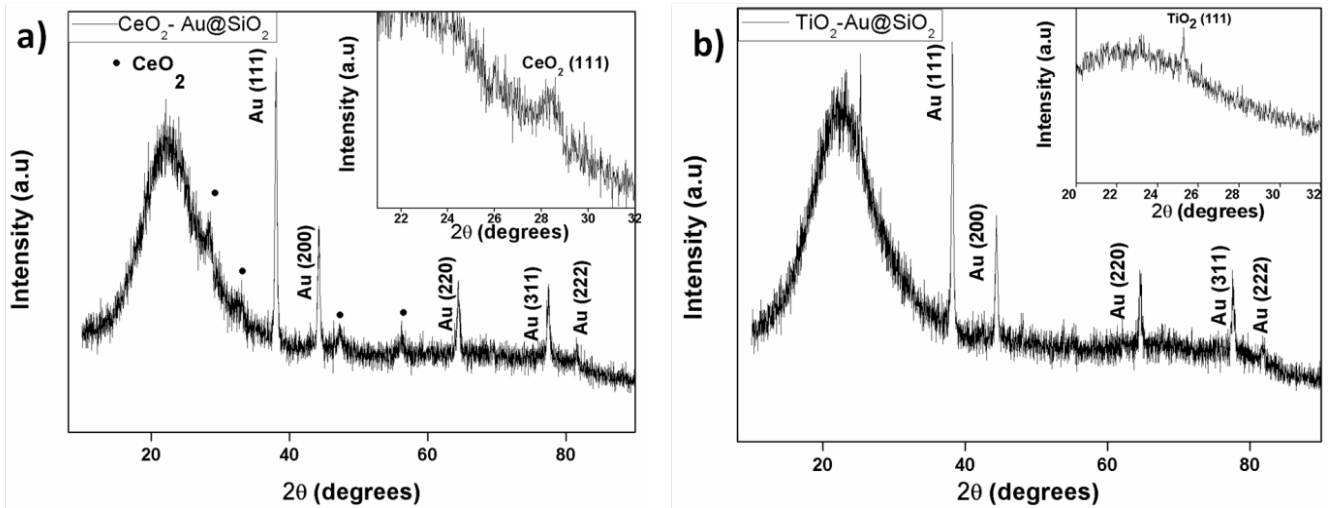
Figure 2.11: The XRD reflections for CeO_2-Au@SiO_2 and TiO_2-Au@SiO_2 catalysts. The inset image shows the reflection from ceria and titania respectively.

Figure 2.11 shows the XRD analysis of the catalysts CeO_2-Au@SiO_2 and TiO_2-Au@SiO_2 and gave typical reflections of the components of the catalysts. The XRD showed the diffraction of Au fcc crystal lattice and the inset in Figure 2.11a showed the reflections from CeO_2 {111} plane and in Figure 2.11b shows the peak from TiO_2 {101} facet. On increasing the loading the intensity from the reflection of the oxide was found to increase as seen from Figure 2.12.
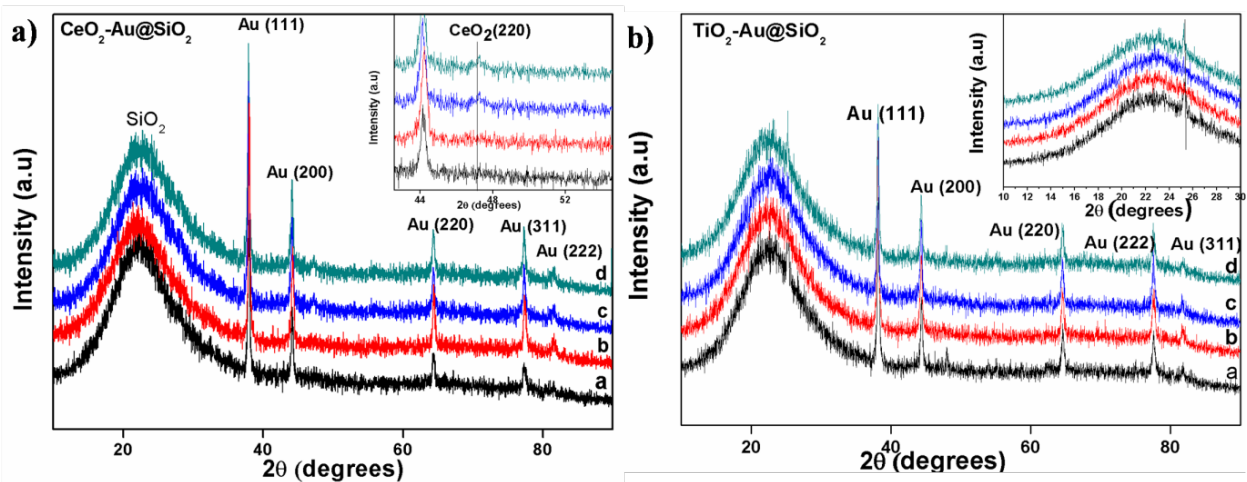
Figure 2.12: The XRD reflections of TOH Au decorated with ceria and titania of a) 1 wt% b) 3 wt% c) 5 wt% d)

7 wt% encapsulated in silica catalyst, the loading of Au is ~ 2 wt%. The inset shows the zoomed in reflections from ceria and titania.

c. UV-Visible spectroscopy
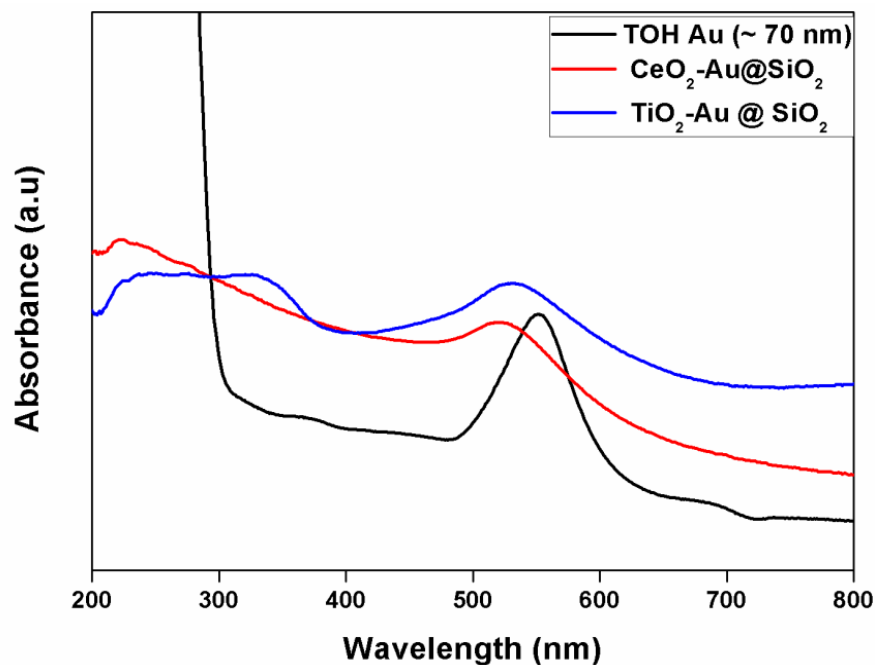
Figure 2.13: The solid state UV-Visible spectrum of CeO_2-Au@SiO_2 and TiO_2-Au@SiO_2 and SPR absorbance of pristine TOH (~ 70 nm) is also shown.

The solid state UV-Visible spectrum shown in Figure 2.13 revealed that the as synthesized colloidal TOH Au (~ 70 nm) nanoparticles have a strong surface plasmon resonance at 550 nm. The position of this band is sensitive to the size, shape and the electronic and optical properties of the surrounding medium. The silica encapsulated and oxide decorated catalyst CeO_2-Au@SiO_2 and TiO_2-Au@SiO_2 showed a blue shift in their surface plasmon resonance band relative to pristine TOH Au nanoparticles. When the silica shell thickness is very large (~ 180 nm) as in our case, scattering phenomena become significant and results in a strong absorbance at shorter wavelength.[35] This effect promotes a blue shift in SPR band. The UV-Vis spectrum shown here is another strong indication that the Au nanoparticles are encapsulated inside silica shell. The UV -visible spectrum of TiO_2 -Au@SiO_2 shows an absorbance between 300 and 400 nm which can be assigned to the absorbance of titania species.[36]

d. Surface area analysis
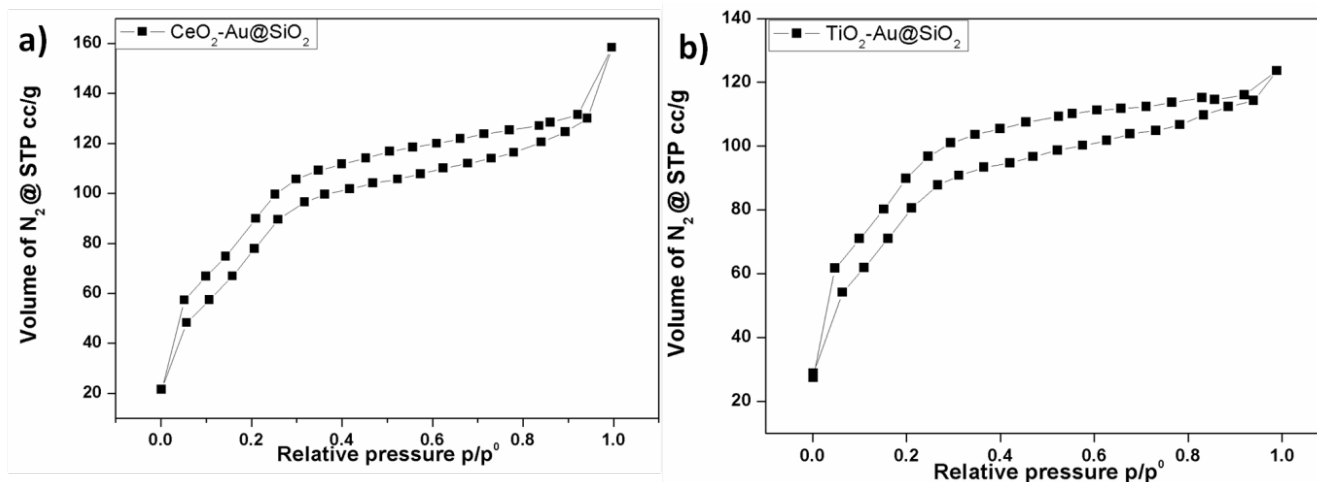
Figure 2.14: The surface area plot for CeO_2-Au@SiO_2 and TiO_2-Au@SiO_2 catalysts.

The textural and compositional properties of the catalysts were characterised using N_2 adsorption desorption analysis and by ICP analysis. The results are summarized in Table 2 1. The catalysts CeO_2-Au@SiO_2 and TiO_2-Au@SiO_2 catalysts were found to show a surface area of 315 m^2/g and 291 m^2/g respectively with a pore size of approximately 2.6 nm (See Figure 2.14 for Isotherm). Thus, the mesoporous nature of the support was confirmed by surface area analysis. The porous nature of silica facilitates easy diffusion of reactants towards the Au core. The amount of ceria and titania with respect to gold was ~ 5 wt% with a Au loading of approximately 2 wt% in both the catalyst as given by ICP analysis 2 wt% in both the catalyst as given by ICP analysis.

No	Catalyst	Surface Area (m²/g)	Mean Pore Volume (cc/g)	Average pore size (nm)	ICP Analysis		
					Au (wt%)	CeO₂ or TiO₂ (wt %)	CeO₂ or TiO₂ to Au ratio
1	CeO₂-Au@SiO₂	315	0.24	2.6	1.8	0.1	0.051
2	TiO₂-Au@SiO₂	291	0.19	2.6	1.7	0.11	0.045

Table 2.1: The table shows surface area/ pore size/ pore volume and ICP analysis value for CeO_2-Au@SiO_2 and

TiO$_2$-Au@SiO$_2$ catalysts.

e. Infrared spectroscopy
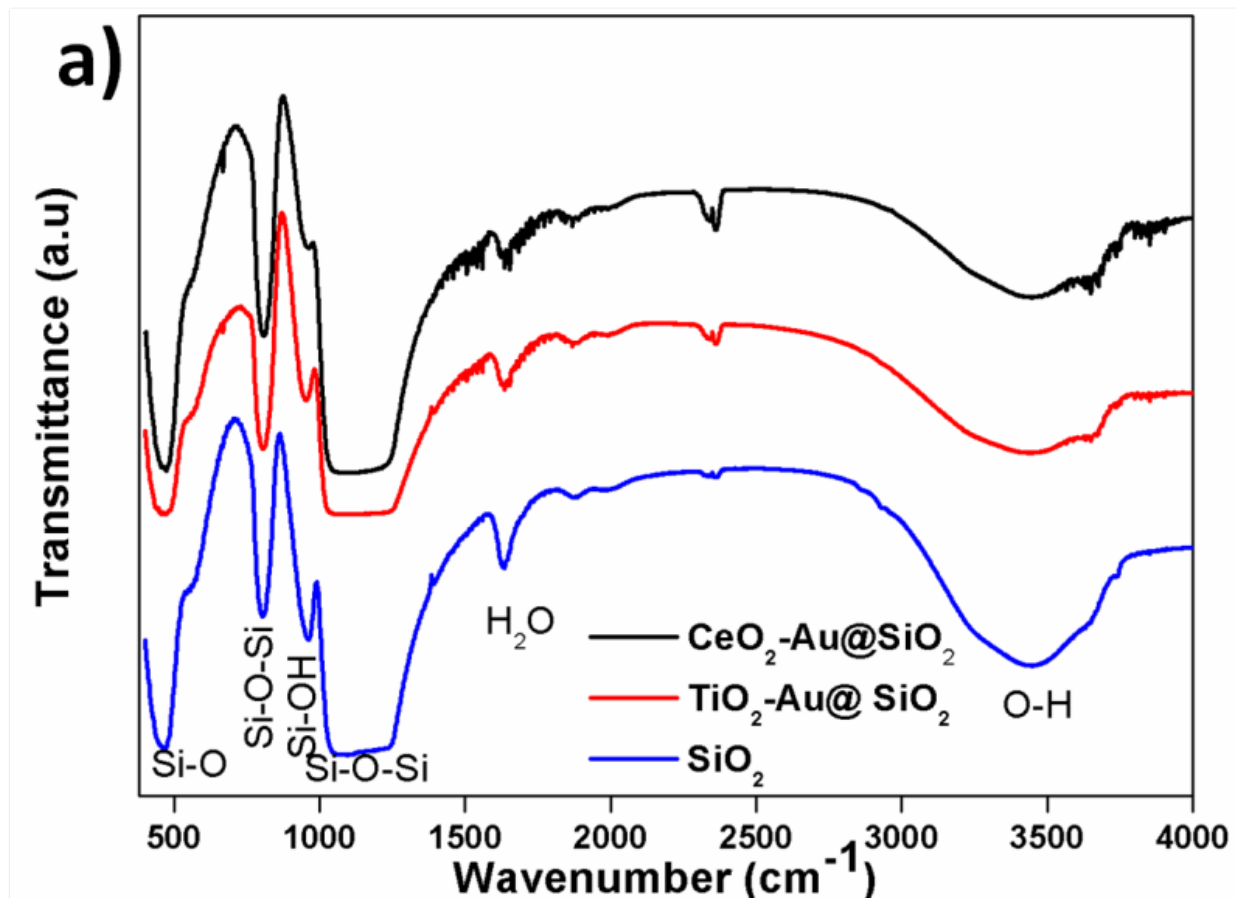
Figure 2.15: IR spectrum of CeO$_2$-Au@SiO$_2$ and TiO$_2$-Au@SiO$_2$ catalysts with SiO$_2$ as reference.

The catalysts were further characterized by Diffused Reflectance Infra Red (DRIFTS) spectroscopy (See Figure 2.15). The features of silica is characterised by peaks at 460 cm^{-1}, 800 cm^{-1}, 960 cm^{-1} and 1105 cm^{-1} corresponding to Si-O bending, Si-O-Si symmetric stretching, Si-OH stretching and Si-O-Si asymmetric stretching.[37] A shoulder at 500-700 cm^{-1} corresponds to Ce-O and Ti-O bond vibrational frequency.[38-40] These signatures were very feeble due to the lower loading in the catalyst. The presence of water can be confirmed from peak at 1600-1630 cm^{-1}. The broad peak above 3000 cm^{-1} corresponds to stretching frequency of hydroxyl group.[39]

Nanoparticles with other shapes: triangles, rods and cubes
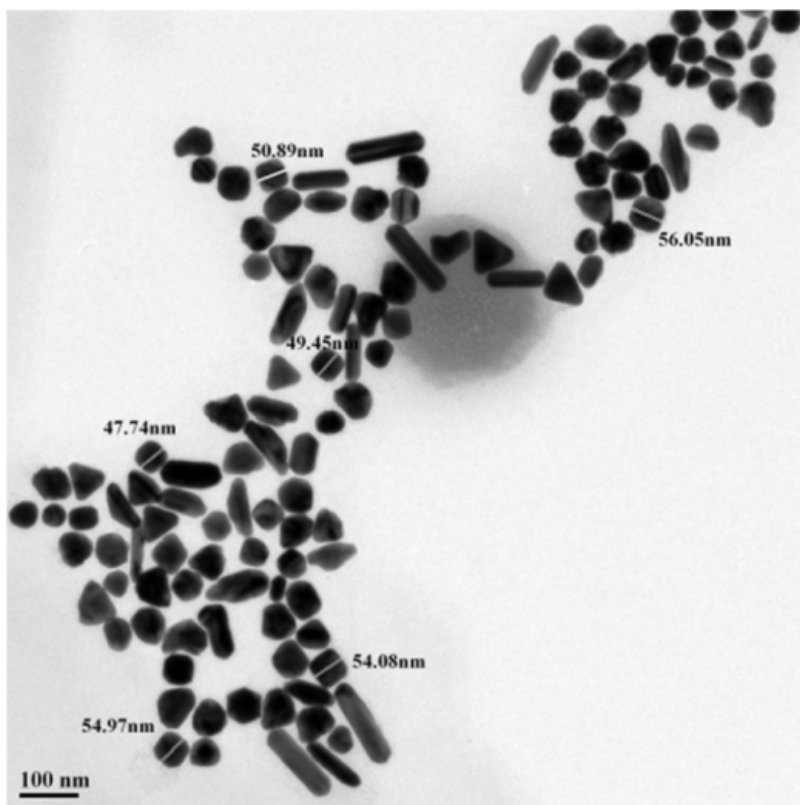
Figure 2.16: TEM image of Au nanocrystals of different morphology used in control experiment.

To probe the structure sensitivity, nanoparticles which expose low index surfaces were synthesized and then TEM image in Figure 2.16 shows the nanoparticles with different shapes. These nanoparticles were found to expose {100} in case of cubes, {111} in case of triangles and {110} in case of rods. The activity was compared with nanoparticles of similar size.

2.5.4. Catalytic activity: CO oxidation

2.5.4.1. CO oxidation from conventional catalyst.

To probe the role of under coordinated atoms in gold catalysis, CO oxidation was carried out on both 45 nm and 110 nm TOH nanoparticles supported on TiO_2 and was found to be moderately active showing conversions around 11% and 24% respectively at 300 °C. The calcined catalysts were subjected to a mild reduction in H_2 atmosphere, which has been shown to dramatically improve the performance of the gold based catalyst.[41-42] The reduced catalysts were subjected to CO oxidation and the steady state conversion of CO for the two catalysts at

various temperatures after a mild reduction in hydrogen is shown in Figure 2.17. The catalysts were found to be active for CO oxidation with conversion reaching 100% at approximately 250 °C. The temperature required for 50% of the CO conversion (T_{50}) was 200 °C for 45 nm particle compared to 230 °C for a 110 nm particle. The shift in the T_{50} temperature is a manifestation of significant density of active sites in a 45 nm 1 wt% catalyst compared to 110 nm 1 wt% catalyst.[14] The catalysts after cooling down to room temperature were then tested for CO oxidation without any pre-treatment. The activity data shown in open circles is remarkable as the catalyst retains up to 80% conversion at 300 °C. The marginal drop in activity could be possibly because of the blocking of the active sites by bicarbonates during the course of the reaction. To confirm that the activity reported here are inherent to the supported gold nanoparticles and not related to the support alone, the catalytic activity were also tested for calcined and reduced TiO_2 which did not show any CO conversion. Furthermore to this, the CO oxidation activity for nanocrystals containing mixture of different shapes (like cube, triangle and rod) synthesized by modified Murphy's procedure were tested.[43] These were carried out as a control experiment to investigate the reactivity of low index {100} and {111} planes present on these nanoparticles.[43] The TEM revealed that the nanocubes were of approximately 50 nm, nanotriangle of approx 60 nm and nanorods of 130 nm. The catalytic activity from mixture of these nanoparticles supported on TiO_2 (1 wt%, after the calcination-reduction step) showed absolutely no activity confirming that the low index planes present on the nanoparticle surface are indeed not active for the reaction. It should be noted that the performance of trisoctahedral gold nanoparticle supported on TiO_2 cannot be compared to the classic Haruta type (less than 5 nm) catalyst supported on TiO_2 which is active at low temperatures for CO oxidation.[3,8] Instead they are comparable to a 50 nm Au nanorice particle with exposed (611) facets supported on ZnO which showed 100% conversion at 280 °C.[44] Clearly, the CO conversion achieved by TOH particles of 110 nm which is more than twice the size of the nanorice and 45 nm TOH particles is very interesting. The full conversion achieved by 45 nm trisoctahedral particle at relatively lower temperature also points to the larger defect density and in turn to the difference in geometry of the defect centres in TOH and nanorice gold. It should be recalled that TOH gold has step sites mostly produced by three or four atom wide terrace as compared to six atom wide terrace-step geometry on

nanorice gold. To test the role of the support in CO oxidation was also performed on trisoctahedral gold nanoparticles supported on SBA-15. In this case no CO conversion was observed even up to 300 °C.
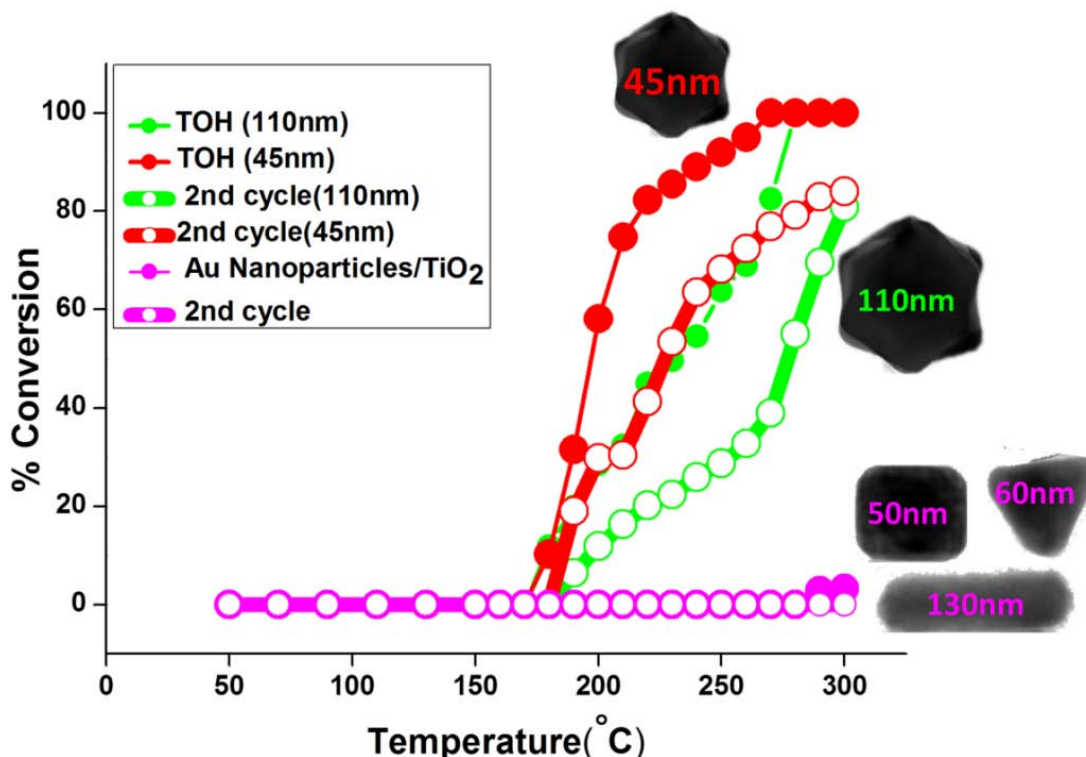
Figure 2.17: The conversion plot for CO oxidation under steady state conditions for a 45 nm and 110 nm trisoctahedral gold nanoparticle supported on TiO_2 after a mild reduction in H_2.The open circle shows the activity of the catalyst during the second cycle. The steady state conversion for a mixture of nanocubes, nanotriangles and nanorods are also plotted.

Previous literature reports suggests that small nanoparticles of approximately 5 nm or less than that supported on SBA-15 are active for CO oxidation.[45] The complete inactivity of TOH supported on SBA-15 also rules out the possibility of smaller particles present in our colloidal system. It is well known that the activation of CO occurs on the metal nanoparticle surface most likely on the defect sites like corner and edge atoms and the O_2 gets activated at the perimeter interface of the metal-oxide support.[5] This provides support to the mechanism of CO oxidation based on an active perimeter interface produced by a reducible support like TiO_2 and trisoctahedral gold nanoparticle being responsible for activating O_2 molecules and subsequent reaction. Even though SBA-15 act as a decent support for Au NPs at the size regime 3-5 nm, the conversion is zero when our

large Au NCs were supported on the same. The analysis of this spent catalyst clearly showed that the particle morphology is completely lost during the calcinations and reduction step or during the reaction and only large spherical particles could be observed in the TEM which could possibly be the reason for the poor activity of this catalyst. The spent catalyst analysis (discussed in section 2.5.6) by TEM also showed smooth facets compared to the original trisoctahedral particles throwing insights into the inactivity.

2.5.4.2. CO oxidation from inverse catalyst system

To probe the role of interfaces, inverse catalyst (i.e. titania decorated on TOH Au nanocrystals) were synthesised, supported and then tested for CO oxidation. The conversion plot for 5 wt% of TiO_2 decorated TOH nanoparticles supported on TiO_2 and SiO_2 is shown in Figure 2.18. The CO oxidation activity of titania and SBA-15 supported titania doped catalyst ATS-5 wt% (45 nm and 70 nm) and ATT-5 wt% (45 nm and 70 nm) (where 5 wt% is the amount of titania doped on Au) reduced at 400 °C is shown in Figure 2.18. The onset temperature for the above mentioned inverse catalysts was shifted significantly to lower temperature when compared to normal TOH nanoparticles supported on TiO_2. It is remarkable to note that all the catalyst showed around 100% conversion at around 230 °C. The onset temperature for titania decorated and silica supported ATS (45 nm and 70 nm)-5 wt% was 100 °C and T_{50} was 180 °C and 190 °C. These results are interesting in the context that the TOH Au nanocrystals supported on SBA-15 showed no activity till 300 °C (also shown in Figure 2.18.). These experiments clearly demonstrate that the inverse model catalyst where co-ordinatively unsaturated metal sites when in intimate contact with an active metal oxide support can facilitate CO oxidation validating the active metal-oxide perimeter model. To investigate the dependence of morphology, TEM nalysis was carried out on the spent ATS catalyst and surprisingly the shape of the ATS catalysts were found to be retained after decorating with titania (Figure 2.27). This is in line with the experiments carried out on nanoporous gold where titania decorated inverse catalyst was shown to preserve the atomic structure of the ligaments due to pinning effects up to fairly large temperatures.[24] The ATT catalysts (45 nm and 70 nm) were found to be more active and gave a conversion of 95% and 97%, respectively, at around 190 °C. The onset temperatures for the reaction were 90 °C for ATT (70 nm) and 100 °C for ATT (45 nm) and the T_{50} values were

140 °C and 150 °C, respectively for ATT (70 nm) and ATT (45 nm) which were lower than the SBA supported catalyst. This document well with the literature that a reducible support like TiO_2 outperforms silica supported gold systems for CO oxidation.[5] Inorder to find the optimum amount of titania doping, TOH Au nanoparticles were decorated with different amount of titania. The titania doping was varied from 4 to 7 wt% with respect to gold. These titania doped gold nanoparticles were then supported on TiO_2 and SBA-15 and tested for CO oxidation. The titania loading on inverse model catalyst were 4, 5, 6 and 7 wt% and found that the optimum was found to be 5 wt% of titania on TOH Au nanoparticles as shown in Figure 2.19.
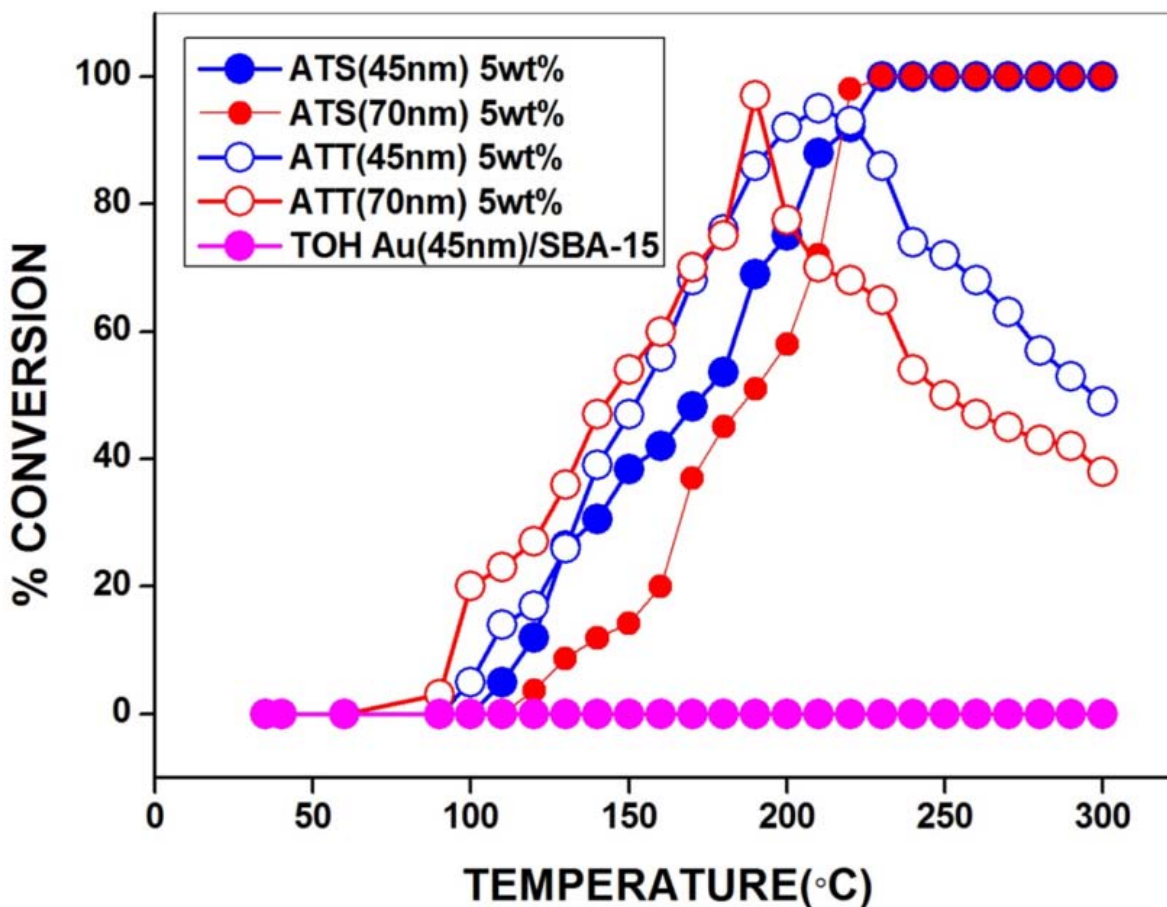
Figure 2.18: The conversion plot for CO oxidation for the inverse systems ATS-5 wt% and ATT-5 wt%. The reactivity of TOH Au/SBA-15 is also shown for comparison.
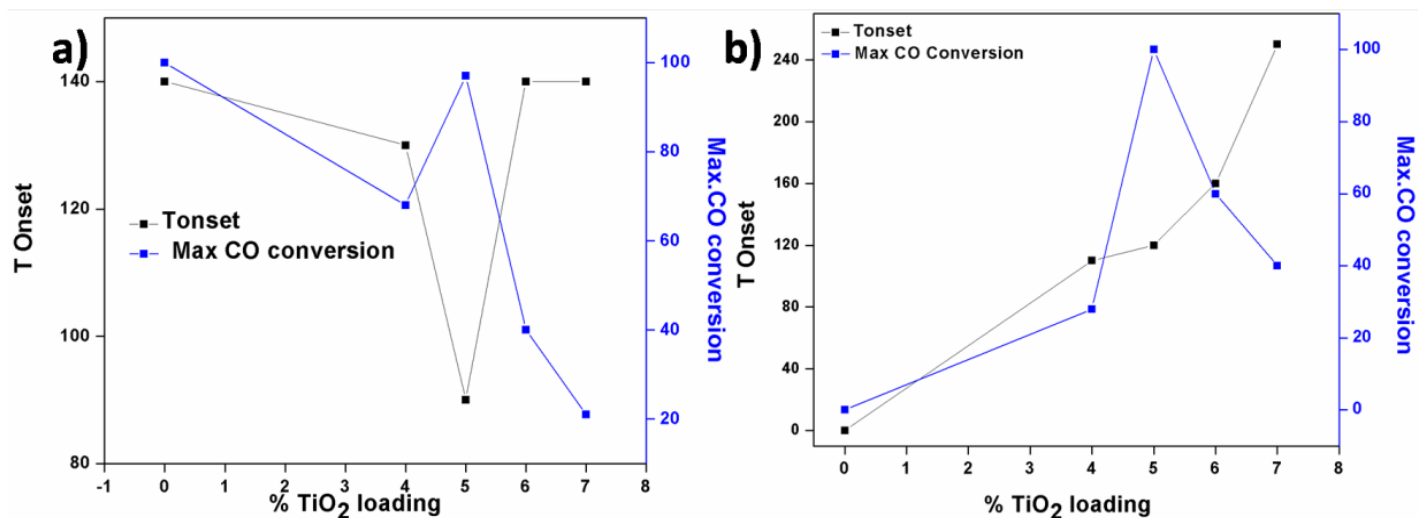
Figure 2.19: The plot showing the dependence of maximum conversion and onset temperature on the oxide loading for a) ATT and b) ATS catalysts.

Unfortunately, both the titania supported inverse TOH catalysts deactivated rapidly after reaching full conversion at approximately 200 °C. A preliminary investigation using FTIR on the origin for this deactivation gave evidence for the presence of bicarbonate on the inverse model catalyst supported on titania (See Figure 2.20). plot shows the FTIR spectra immediately recorded after the CO oxidation reaction on ATT 5 wt% (denoted as ATT 5S for spent catalyst) showed characteristic vibrational feature at 1290 cm^{-1} which is assigned to OH deformation of a bicarbonate species. Scurrell and co-workers have identified bicarbonate species as a route cause for deactivation for gold supported on titanates.[46] According to this literature, accumulation of bicarbonate which is generated from CO_2 formed during the reaction blocks the active site leading to rapid catalyst deactivation. The absence of this feature on the fresh catalyst (ATT 5 wt%) clearly showed that these are generated during the course of the reaction. They also proposed the beneficial role of water vapour which is to aid decomposition of bicarbonates which otherwise blocks the active sites. These features were conspicuously absent on titania decorated TOH supported on SBA-15 which were found not to deactivate in our experiments. The IR absorption frequency at 1730 cm^{-1} can be assigned to the bridging bonding configuration of the surface carbonates.[47]
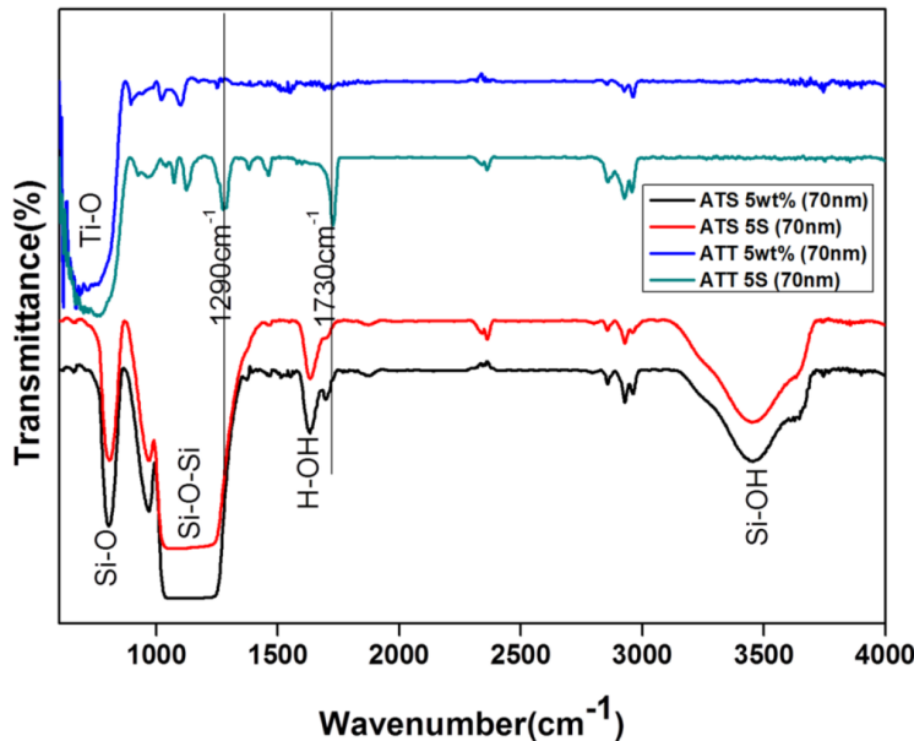
Figure 2.20: FT-IR spectrum of as synthesised ATS 5 wt% and spent ATS 5S (70 nm) and ATT 5 wt% and spent ATT 5S (70 nm) and after CO oxidation reaction ATT 5S shows the presence of bicarbonates at 1290 cm^{-1}.
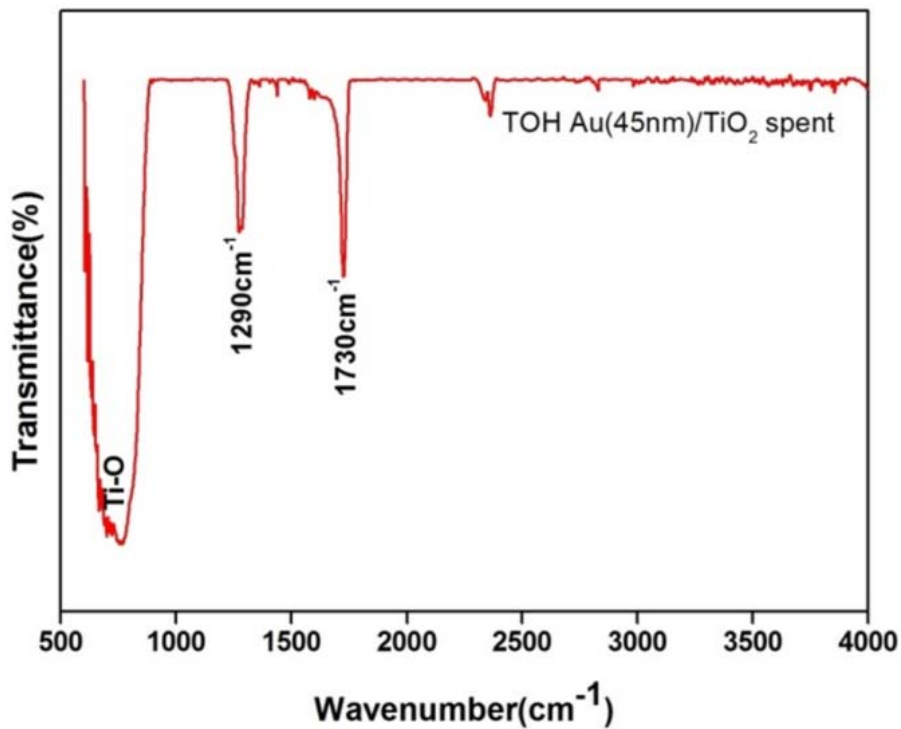
Figure 2.21: IR spectrum of TOH Au (45 nm)/TiO$_2$ after CO oxidation reaction. The peaks at 1290 cm^{-1} and

1730 cm^{-1} show the presence of bicarbonates and bridging carbonyls in the catalyst.

The A small decrease in activity in the second cycle for CO oxidation for the normal TOH supported TiO$_2$ (in Figure 2.18) could also be because of the accumulation of bicarbonates as their presence was detected in the spent catalyst which is shown in Figure 2.21.

2.5.4.3. CO oxidation from encapsulated system

The CO oxidation was carried out on the catalysts with 1, 3, 5, and 7 wt% oxide loading. Here also, the optimum loading was found to be 5 wt % with respect to gold. The catalyst CeO$_2$-Au@SiO$_2$ and TiO$_2$-Au@SiO$_2$ with ~ 1.8 wt% Au loading and decorated with oxide nanoparticle (5 wt% with respect to Au) were room temperature active towards CO oxidation reaction in spite of the size of Au nanoparticle (~ 70 nm) being well above the optimum size regime. The activity was found to decline with increase in loading of nano oxide (see Figure 2.22). The optimum loading was found to be 5 wt% with respect to gold and only those catalysts are compared and discussed in the following section. The lower activity of 1 and 3 wt% can be assumed due to the lower number of active metal-oxide interfaces and that of 7 wt% to the blocking of active sites by these oxides.
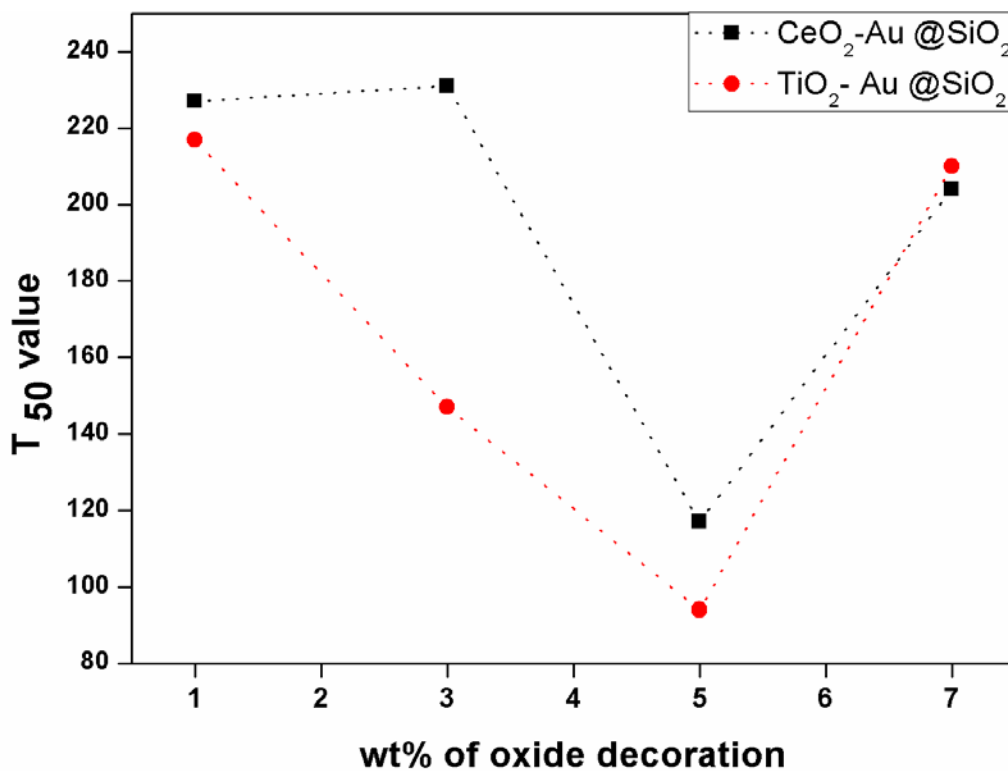
Figure 2.22: Temperature of 50% CO conversion versus TiO$_2$/CeO$_2$ content for different catalysts.

In Figure 2.23 the CO oxidation profile for CeO_2-Au@SiO_2 and TiO_2-Au@SiO_2 for the first two runs and the activity was compared with that of TOH Au@SiO_2 and TOH Au supported on SBA-15 catalysts. During the first cycle, both the catalyst showed a light off temperature at 120 °C with a T_{50} value of around 160 °C. After the first cycle, the catalyst was cooled down to room temperature and during the second cycle, there was a drastic shift in the light off to room temperature with TiO_2-Au@SiO_2 showing a conversion of 3% and CeO_2-Au@SiO_2 of 5% respectively. The T_{50} value was also shifted to 90 °C and 120 °C for TiO_2-Au@SiO_2 and CeO_2-Au@SiO_2 respectively. The catalyst showed full CO conversion with TiO_2-Au@SiO_2 showing a slight edge in conversion rate with 100% conversion at 160 °C compared to CeO_2-Au@SiO_2 which showed full conversion at 250 °C. The activity was also compared with TOH Au@SiO_2 catalyst which showed a maximum CO conversion of 80% at 300 °C.
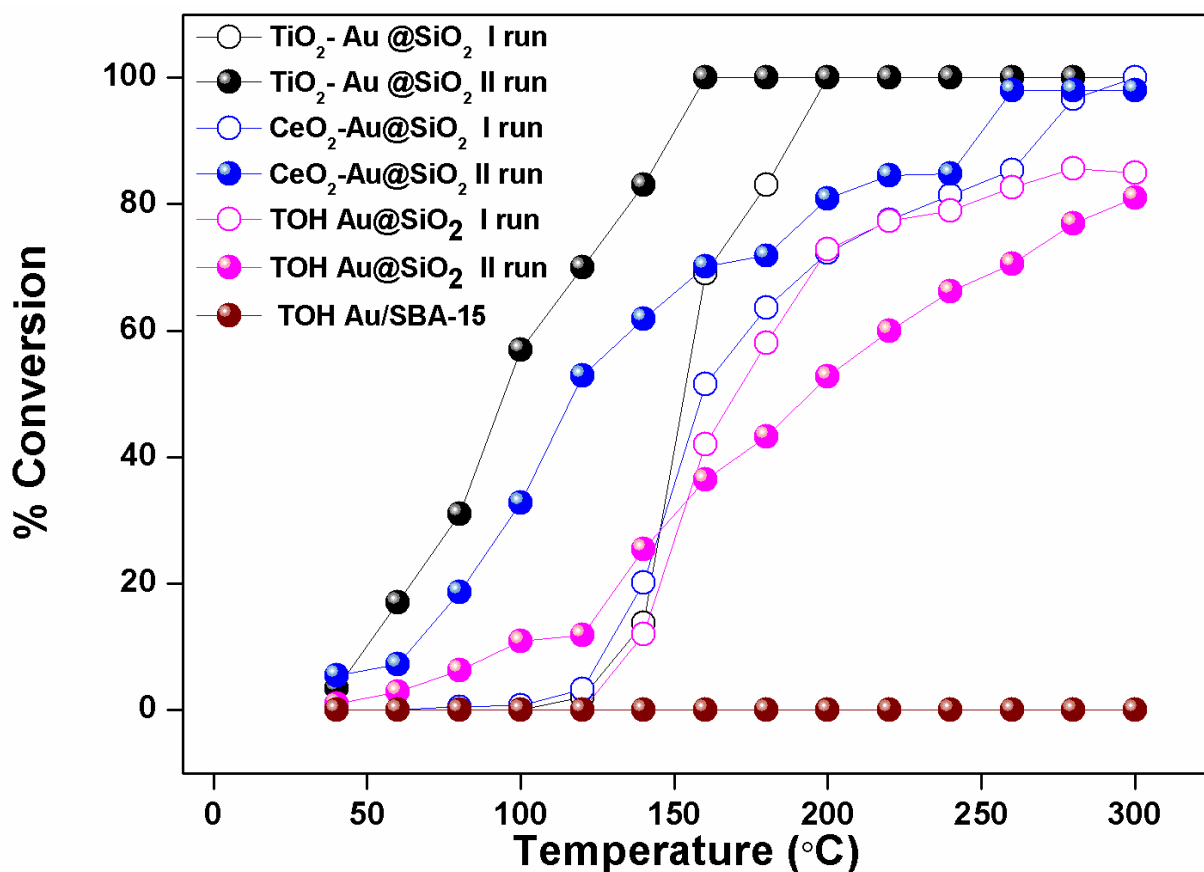
Figure 2.23: The CO oxidation activity profile for CeO_2-Au@SiO_2 and TiO_2-Au@SiO_2 catalyst. The performance of TOH Au @ SiO_2 and TOH Au supported on SBA-15 is also shown.

This clearly depicts that an active metal-oxide interface in contact with under co-ordinated Au atoms can enhance the catalytic activity even though the size of the nanoparticle is above the optimum. As a control experiment TOH Au (~ 70 nm) nanoparticles were also supported on SBA-15 and tested for CO oxidation. The catalyst was not active for CO oxidation even up to 300 °C, demonstrating here how the absence of an active oxide-metal perimeter can inhibit CO oxidation catalysis by gold nanoparticles. A previous study also showed that the morphology of TOH nanoparticles (~ 45 nm) was lost on SBA-15 support. This study shows that the retention of morphology thereby preserving the step atoms (active sites) is an essential criterion for these large Au nanoparticles to show the activity. Here using the encapsulation strategy, complete preservation of the shape of the Au nanoparticles which exposes the high index facets carrying periodic defective centers is achieved. The high temperature pre treatments did not change the structure of the encapsulated catalyst. The catalysts achieved 100% conversion and were resistant to deactivation. Concerning the mechanism of CO oxidation, CO interacts with Au surface mainly on under coordinated atoms and oxygen activation is proposed to occur on the oxygen vacancy of the support at the metal-oxide interface. The role of contact between metal and oxide support was elucidated by using a physical mixture of Au colloid (~ 5 nm) and Degussa P25 by Haruta and co workers.[48] The authors proved that the physical mixture calcined at 600 °C with Au particle of size ~ 12 nm were found to show a similar activity for CO oxidation as that of Au(~ 6 nm)/TiO_2 synthesized by deposition precipitation method. The role of incorporating oxides into Au/SiO_2 matrix has been extensively explored.[49-50] The active perimeter, which the TOH Au that exposes {110} step atoms make with the reducible oxide (TiO_2 or CeO_2) makes the CO oxidation facile on such structured large Au nanoparticles at room temperature. The step atoms may probably act as the active centers for CO adsorption and the oxygen dissociation occurs at active metal-oxide interface or on oxygen vacancies on silica and when this happens within the close proximity of CO adsorption site, it combines with dissociated oxygen forming CO_2 as proved in the literature.[5,51-52]

2.5.4.4. Comparison between CO oxidation activity of conventional, inverse and encapsulated systems

The CO oxidation profile of titania decorated encapsulated system TiO_2-Au@SiO_2 (as it showed a relatively better activity as compared to ceria decorated one) was also compared to those supported real and inverse

system which was discussed before in section 2.5.4.1 and 2.5.4.2. The comparison clearly showed that the encapsulation strategy adopted shifted the reaction regime to a lower temperature. Figure 2.24 shows the CO oxidation profile for TiO_2-Au@SiO_2, TiO_2 decorated TOH Au supported on silica, (ATS ~ 70 nm 5 wt%) and TiO_2 decorated TOH Au supported on titania (ATT ~ 70 nm 5 wt%), and trisoctahedral Au (~ 70 nm) nanoparticles supported on TiO_2. Here, 5 wt% denote the oxide loading in the catalysts. It can be clearly noticed that the TiO_2-Au@SiO_2 with a TOH Au nanoparticles of size ~ 70 nm showed appreciable activity (3%) at room temperature with a T_{50} value of 94 °C and a full conversion at 160 °C. The conventional TOH Au (~ 70 nm) /TiO_2 supported catalysts were found to show an onset at around 150 °C and temperature of full conversion at 270 °C. The activity profile of TiO_2 decorated inverse systems supported on silica and titania (ATS and ATT) with Au loading of ~ 1 wt% were found to shift to lower temperature regime as compared with conventional supported system.
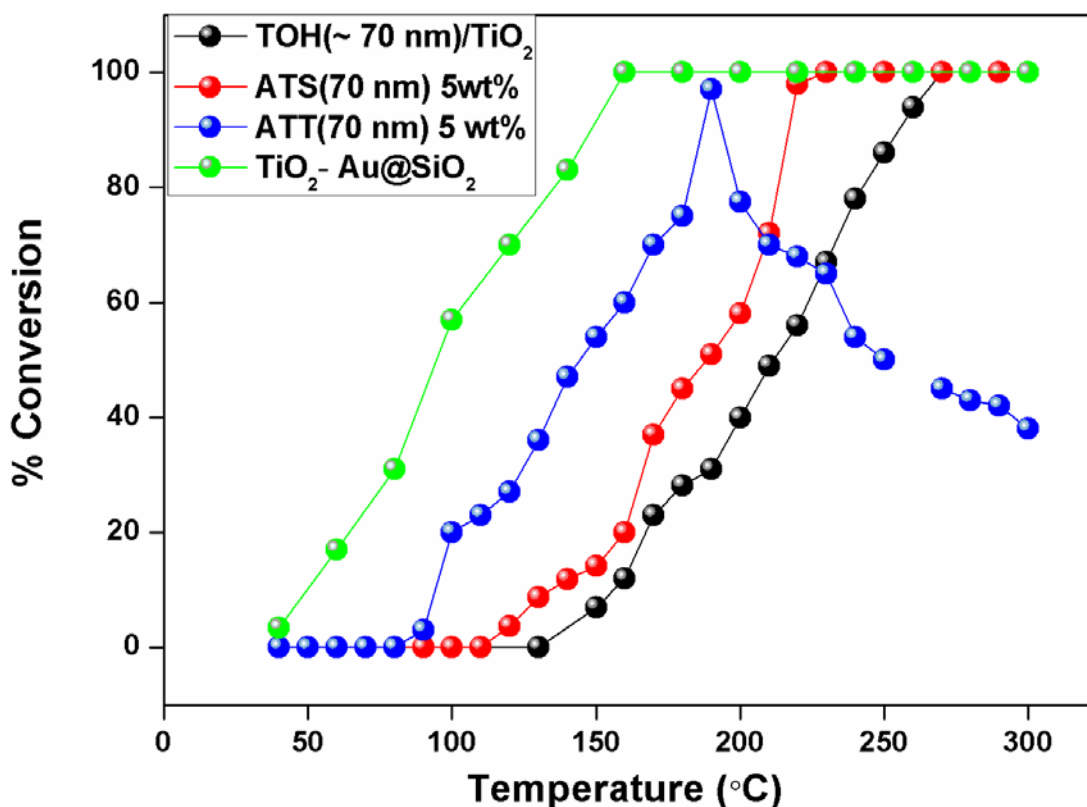
Figure 2.24: The CO oxidation activity for TiO_2-Au@SiO_2, inverse systems ATS-5 wt% and ATT-5 wt% and conventional TOH Au (~ 70 nm) supported on TiO_2.

The T_{onset}, T_{50} and T_{100} value of the other catalyst are compiled in Table 2.2. It was also observed that the titania decorated TOH Au supported on titania (ATT- 5 wt%) system was found to deactivate. The preliminary reason for the same can be attributed to the presence of bicarbonates which was discussed in our previous section. The low temperature CO oxidation activity by the encapsulated large trisoctahedral inverse Au catalysts clearly shows that the encapsulation strategy can preserve the active sites by retaining the morphology. This also proves that surface sites with under co-ordination when in close proximity with suitable oxides can impart reactivity even in the size regimes where gold is not shown to be active for CO oxidation previously.

No.	Catalyst	T_{onset} (3% CO conversion)	T_{50}	T_{100}
1	TOH(~ 70 nm)/TiO$_2$	140	212	270
2	ATS(~ 70 nm) 5 wt%	120	190	225
3	ATT(~ 70 nm) 5 wt%	90	145	190
4	TiO$_2$-Au@SiO$_2$	40	94	160

Table 2.2: The table showing T_{onset}, T_{50} and T_{100} for different catalyst systems.

2.5.5. Catalyst stability and time on stream

The stability of the catalyst on stream was tested. The catalyst TiO$_2$-Au@SiO$_2$ showed 100% conversion till 300 °C and gave a similar conversion trend up to 4 h at 160 °C compared to ATS (~ 70 nm) 5 wt% which showed a decrease in conversion to 80% after 4 h of time on stream at 220 °C as indicated by Figure 2.25. This again proves the stability of encapsulated system when compared to supported ones.
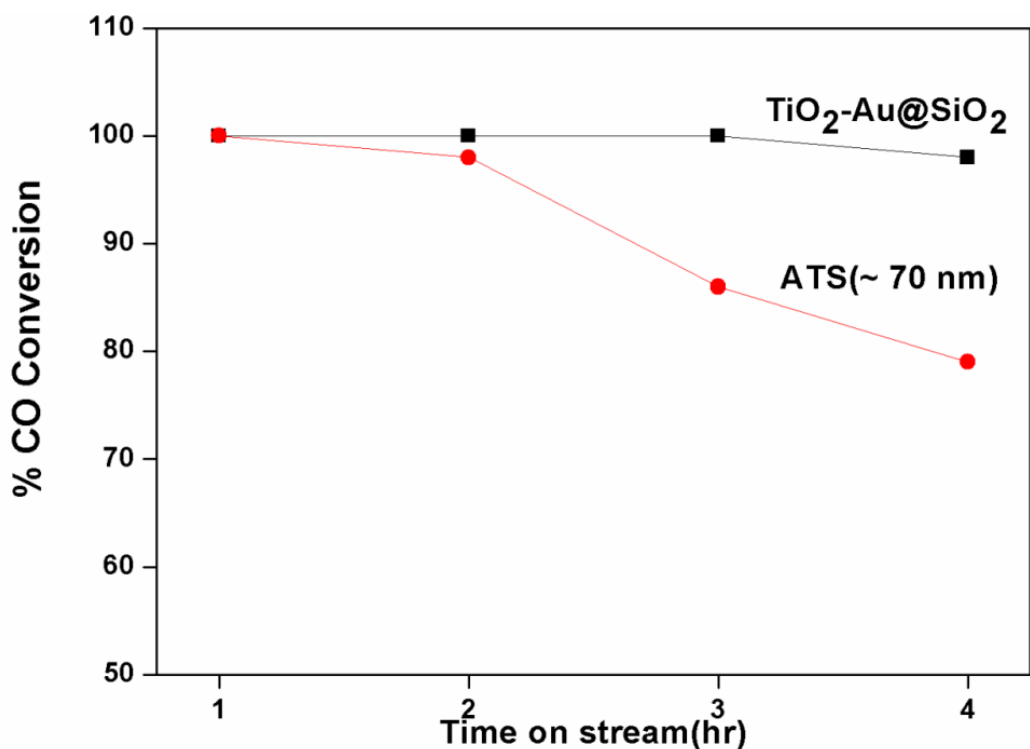
Figure 2.25: Time on stream experiments on TiO_2-Au@SiO_2 done at 160 °C and ATS (~ 70 nm) 5 wt% at 220 °C towards CO oxidation reaction.

2.5.6. Spent catalyst analysis
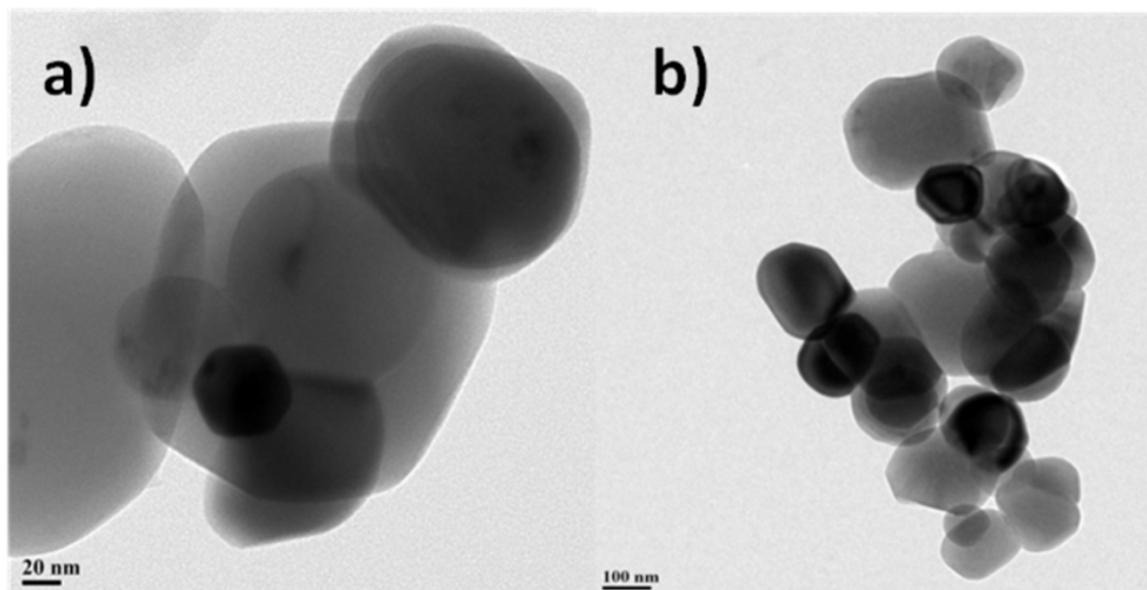
Figure 2.26: TEM image of the spent catalyst a) TOH (45 nm)/TiO_2, b) TOH (110 nm)/TiO_2 respectively after two cycles of CO oxidation which shows that the particle morphology is intact even after the reaction.

Since the trisoctahedral nanoparticles retained its catalytic activity for two cycles of CO oxidation reaction, TEM analysis was carried out to find out the morphology of the particles of these spent catalysts. The microscopy images clearly showed the 110 nm catalyst after two cycles of CO oxidation to show more or less the original morphology as shown in Figure 2.26. The analysis of TOH Au on SBA-15 spent catalyst clearly showed that the particle morphology was completely lost during the calcinations and reduction step or during the reaction and only large spherical particles in the TEM were observed which could possibly be the reason for the poor activity of this catalyst (Figure. 2.27). The inset of the Figure 2.27a also shows a high resolution TEM image of one of the particles which clearly showed smoother facets compared to the original trisoctahedral particles. To investigate the dependence of morphology, TEM analysis on the spent ATS catalyst was done and the shape of the ATS catalysts was found to be retained after decorating with titania (Figure 2.27b). This is in line with the experiments carried out on nanoporous gold where titania decorated inverse catalyst was shown to preserve the atomic structure.[24]
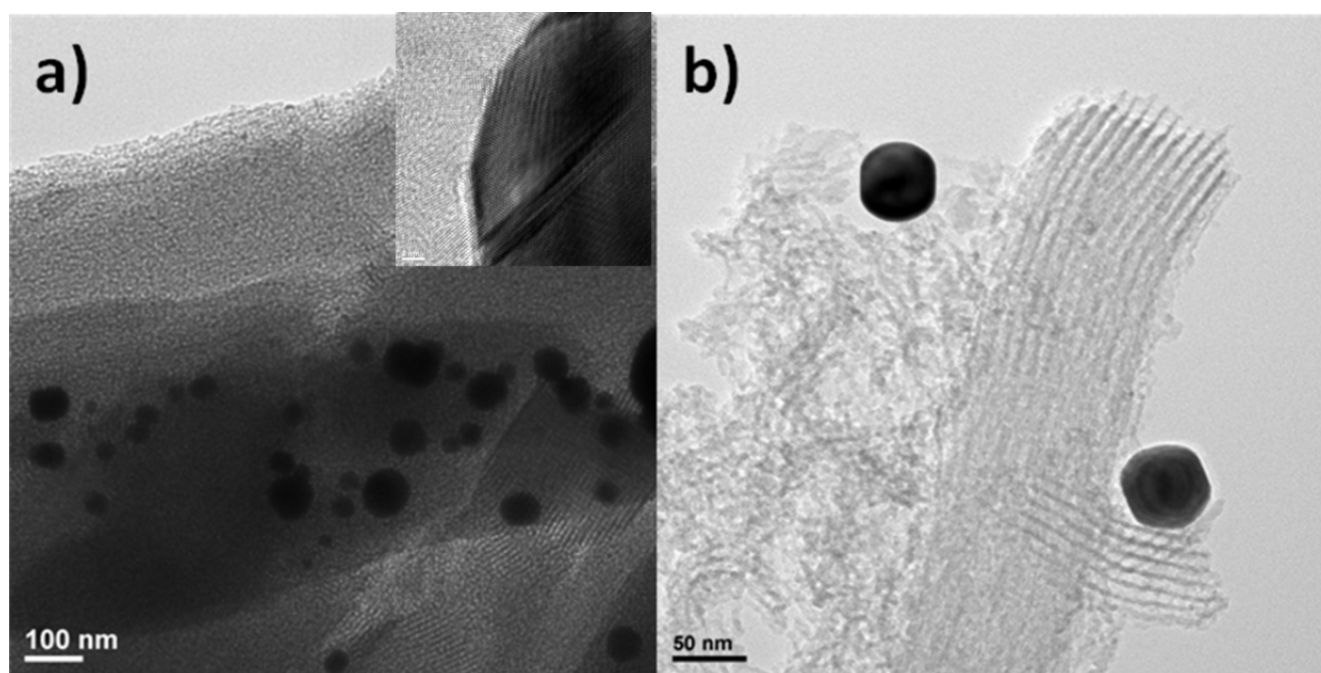
Figure 2.27: TEM image of the a) spent TOH Au supported on SBA-15 and b) spent inverse ATS (45 nm) 5 wt% catalyst.
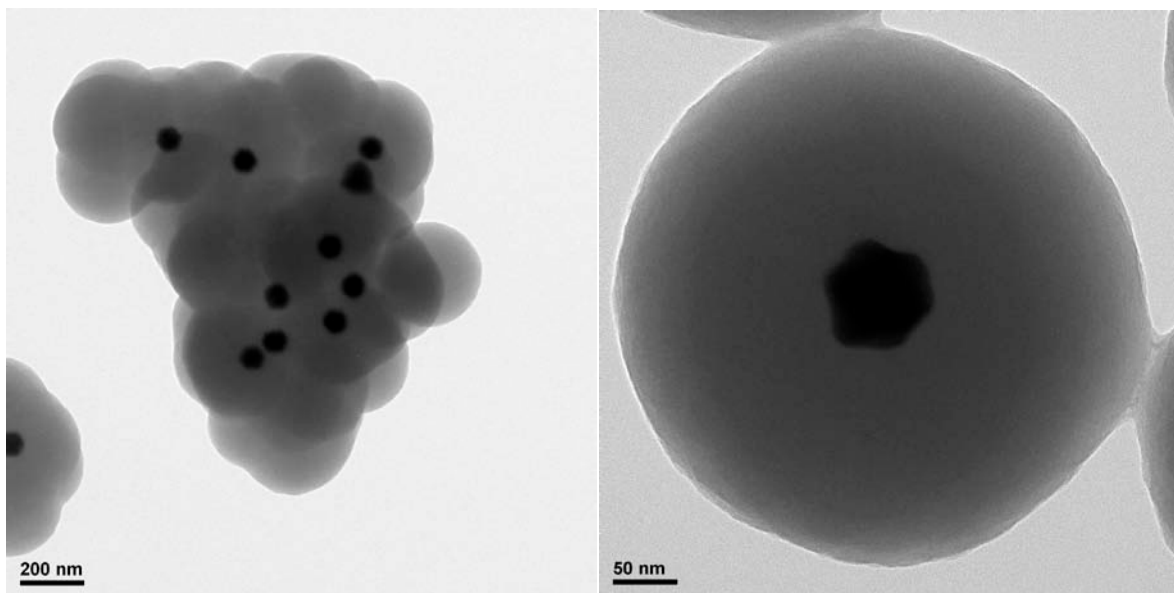
Figure 2.28: The TEM image of the spent catalyst TiO_2-Au@SiO_2 after III cycles of CO oxidation activity.

The spent catalyst analysis by transmission electron microscope of the encapsulated catalyst revealed that the shape of the nanoparticles was completely retained (Figure 2.28).

2.6. Conclusions

To elucidate active sites and the role of Au-metal oxide interfaces in gold catalysis and to the explore role of confinement effects, large trisoctahedral (TOH) Au nanoparticles exposing periodic {110} sites were synthesised using a reported procedure. These nanoparticles supported on different metal oxides were tested for CO oxidation and their activity compared with inverse catalysts. The inverse catalysts are the ones where TOH Au nanoparticles were decorated with active oxides to create a better metal-oxide interface. The trisoctahedral Au nanoparticles were supported on active and inactive supports. The CO oxidation was found to be facile on trisoctahedral Au nanoparticles supported on active support like TiO_2 while they were inactive till 300 °C on SBA-15 proving the importance of reducible support for CO oxidation. The structure sensitivity was proved by comparing the activity of TiO_2 supported trisoctahedral Au nanoparticles with that of nanotriangles, nanorods and nanocubes which were not active under the reaction temperature regime. The inverse system was found to be more active than the supported TOH Au nanoparticles demonstrating the special reactivity of active-metal oxide interface. The role of confinement effects was probed by encapsulating the trisoctahedral Au

nanoparticles and inverse system inside porous silica shell. The encapsulated systems were found to show appreciable activity at room temperature. The encapsulation protocol helps to maintain the particle morphology and thereby making the active centers intact. This chapter thus gives further insights into the reactivity of under coordinated sites, metal-oxide perimeter interface and the role of confinement effects on the catalytic activity of gold.

2.7. References

(1)   Hammer, B.; Norskov, J. *Nature,* **1995**, *376*, 238.

(2)   Hutchings, G. J.; Brust, M.; Schmidbaur, H. *Chem Soc Rev,* **2008**, *37*, 1759.

(3)   Haruta, M.; Yamada, N.; Kobayashi, T.; Iijima, S. *J Catal,* **1989**, *115*, 301.

(4)   Haruta, M. *CATTECH,* **2002**, *6*, 102.

(5)   Schubert, M. M.; Hackenberg, S.; van Veen, A. C.; Muhler, M.; Plzak, V.; Behm, R. J. *J Catal,* **2001**, *197*, 113.

(6)   Valden, M.; Lai, X.; Goodman, D. W. *Science,* **1998**, *281*, 1647.

(7)   Yoon, B.; Häkkinen, H.; Landman, U.; Wörz, A. S.; Antonietti, J.-M.; Abbet, S.; Judai, K.; Heiz, U. *Science,* **2005**, *307*, 403.

(8)   Haruta, M.; Tsubota, S.; Kobayashi, T.; Kageyama, H.; Genet, M. J.; Delmon, B. *J Catal,* **1993**, *144*, 175.

(9)   Bond, G.; Thompson, D. *Gold Bull,* **2000**, *33*, 41.

(10)   Sekhar, A. C. S.; Meera, C. J.; Ziyad, K. V.; Gopinath, C. S.; Vinod, C. P. *Catal Sci Technol,* **2013**, *3*, 1190.

(11)   Taylor., H. S. *Pro R Soc Lond Ser A,* **1925**, *108*, 105.

(12)   Dahl, S.; Logadottir, A.; Egeberg, R. C.; Larsen, J. H.; Chorkendorff, I.; Törnqvist, E.; Nørskov, J. K. *Phys Rev Lett,* **1999**, *83*, 1814.

(13)   Vinod, C. P.; Niemantsverdriet, J. W.; Nieuwenhuys, B. E. *Phys Chem Chem Phys,* **2005**, *7*, 1824.

(14)   Mavrikakis, M.; Stoltze, P.; Nørskov, J. K. *Catal Lett,* **2000**, *64*, 101.

(15)   Quan, Z.; Wang, Y.; Fang, J. *Acc Chem Res,* **2012**, *46*, 191.

(16)   Yu, Y.; Zhang, Q.; Lu, X.; Lee, J. Y. *J Phys Chem C,* **2010**, *114*, 11119.

(17)   Guczi, L.; Petö, G.; Beck, A.; Frey, K.; Geszti, O.; Molnár, G.; Daróczi, C. *J Am Chem Soc,* **2003**, *125*, 4332.

(18)   Suchorski, Y.; Wrobel, R.; Becker, S.; Weiss, H. *J Phys Chem C* ,**2008**, *112*, 20012.

(19)   Rodriguez, J. A.; Ma, S.; Liu, P.; Hrbek, J.; Evans, J.; Pérez, M. *Science,* **2007**, *318*, 1757.

(20)   Magkoev, T. T. *Surf Sci,* **2007**, *601*, 3143.

(21)   Zhou, Z.; Kooi, S.; Flytzani-Stephanopoulos, M.; Saltsburg, H. *Adv Funct Mater,* **2008**, *18*, 2801.

(22)   Déronzier, T.; Morfin, F.; Massin, L.; Lomello, M.; Rousset, J.-L. *Chem Mater,* **2011**, *23*, 5287.

(23)   Wittstock, A.; Zielasek, V.; Biener, J.; Friend, C. M.; Bäumer, M. *Science,* **2010**,*327*, 319.

(24)   Wichmann, A.; Wittstock, A.; Frank, K.; Biener, M. M.; Neumann, B.; Mädler, L.; Biener, J.; Rosenauer, A.; Bäumer, M. *Chem Cat Chem,* **2013**, *5*, 2037.

(25)   Biener, M. M.; Biener, J.; Wichmann, A.; Wittstock, A.; Baumann, T. F.; Ba̋umer, M.;Hamza, A. V. *Nano Lett,* **2011**, *11*, 3085.

(26)   Guo, H.; Al-Hunaiti, A.; Kemell, M.; Rautiainen, S.; Leskelä, M.; Repo, T. *ChemCatChem,* **2011**, *3*, 1872.

(27)   Lazar, M.; Angelici, R. J. *J Am Chem Soc,* **2006**, *128*, 10613.

(28)   Angelici, R. J. *Catal Sci & Technol,* **2013**, *3*, 279.

(29)   Zhu, H.; Liang, C.; Yan, W.; Overbury, S. H.; Dai, S. *J Phys Chem B,* **2006**, *110*, 10842.

(30)   Joo, S. H.; Park, J. Y.; Tsung, C.-K.; Yamada, Y.; Yang, P.; Somorjai, G. A. *Nat Mater,* **2009**, *8*, 126.

(31)   Arnal, P. M.; Comotti, M.; Schüth, F. *Angew Chem Int Ed,* **2006**, *45*, 8224.

(32)   Sunil Sekhar, A. C.; Ziyad, K.; Soni, Y.; Vinod, C. P. *Chem Cat Chem,* **2015**, *7*,1222.

(33)   Graf, C.; Vossen, D. L. J.; Imhof, A.; van Blaaderen, A. *Langmuir,* **2003**, *19*, 6693.

(34)   Yu, Y.; Zhang, Q.; Lu, X.; Lee, J. Y. *J Phys Chem C,* **2011**,*114*, 11119.

(35)   Liz-Marzán, L. M.; Giersig, M.; Mulvaney, P. *Langmuir* **1996**, *12*, 4329.

(36)   Awati, P. S.; Awate, S. V.; Shah, P. P.; Ramaswamy, V. *Catal Commun,* **2003**, *4*, 393.

(37)   Musić, S.; Filipović-Vinceković, N.; Sekovanić, L. *Brazilian j chem eng,* **2011**, *28*, 89.

(38)   Chen, L.; Pang, X.; Yu, G.; Zhang, J. *Adv Mater Lett,* **2010**, *1*, 75.

(39)   Song, X.; Jiang, N.; Li, Y.; Xu, D.; Qiu, G. *Mater Chem Phys,* **2008**, *110*, 128.

(40)   Kwon, Y. G.; Choi, S. Y.; Kang, E. S.; Baek, S. S. *J. Mater. Sci,* **2000**, *35*, 6075.

(41)   Dekkers, M. A. P.; Lippits, M. J.; Nieuwenhuys, B. E. *Catal Lett,* **1998**, *56*, 195.

(42)   Yan, W.; Chen, B.; Mahurin, S. M.; Schwartz, V.; Mullins, D. R.; Lupini, A. R.; Pennycook, S. J.; Dai, S.; Overbury, S. H. *J Phys Chem B,* **2005**, *109*, 10676.

(43)   Sau, T. K.; Murphy, C. J. *J Am Chem Soc,* **2004**, *126*, 8648.

(44)   Zheng, Y.; Tao, J.; Liu, H.; Zeng, J.; Yu, T.; Ma, Y.; Moran, C.; Wu, L.; Zhu, Y.; Liu, J.; Xia, Y.

      Small, **2011**, *7*, 2307.

(45)   Yang, C.-m.; Kalwei, M.; Schüth, F.; Chao, K.-j. *Appl Catal A,* **2003**, *254*, 289.

(46)   Ntho, T. A.; Anderson, J. A.; Scurrell, M. S. *J Catal,* **2009**, *261*, 94.

(47)   Liao, L. F.; Lien, C. F.; Shieh, D. L.; Chen, M. T.; Lin, J. L. *J Phys Chem B,* **2002**, *106*, 11240.

(48)   Tsubota, S.; Nakamura, T.; Tanaka, K.; Haruta, M. *Catal Lett,* **1998**, *56*, 131.

(49)   Qian, K.; Lv, S. S.; Xiao, X. Y.; Sun, H. X.; Lu, J. Q.; Luo, M. F.; Huang, W. X. *J Mol Catal A,* **2009**, *306*, 40.

(50)   Dekkers, M. A. P.; Lippits, M. J.; Nieuwenhuys, B. E. *Catal Today,* **1999**, *54*, 381.

(51)   Chiang, C.-W.; Wang, A.; Mou, C.-Y. *Catal Today,* **2006**, *117*, 220.

(52)   Rombi, E.; Cutrufello, M. G.; Cannas, C.; Casu, M.; Gazzoli, D.; Occhiuzzi, M.; Monacia, R.; Ferinoa, I. *Phys Chem Chem Phys,* **2009**, *11*, 593.

Chapter 3

Shape controlled synthesis of Pd nanoparticles and their application as catalyst for coupling and oxidation reactions[#]

[#]*The chapter is adapted from:*

S. Sreedhala, V. Sudheesh Kumar and C. P. Vinod, Nanoscale, 2014, 6, 7496-7502.

S. Sreedhala, V. Sudheesh Kumar and C. P. Vinod, Journal of Catalysis, 2016, 337, 138-144.

3.1. Introduction

Palladium nanoparticles find potential applications in catalysis, pollution abatement, energy storage etc.[1-3] The intrinsic chemical reactivity of nanoparticles depend on factors like size,[4] shape,[5] support,[6] metal support interaction etc.[7-8] The chemical activity and selectivity of nanoparticle is found to depend on the arrangement of atoms on the nanoparticle surface. The special reactivity of low co-ordinated atoms and atomic steps has been a topic of interest from 1920's to recent past.[9] The theoretical and experimental results from both fcc and hcp transition metal nanoparticles have shown that the active centres in the form of B5 sites are found to significantly influence the activation of adsorbate molecules.[10-12] The synthesis of high index faceted nanostructures carrying such sites is challenging as the growth rate is fast in the direction normal to the high index facets. But these high energy facets consist of surface atom with low co-ordination number which makes them chemically more active than their low index counter parts.[13-14] These atoms of under coordination can act as active centers for breaking and making of bonds. There are a few reports in literature which depicts the synthesis of high index faceted Pd nanostructures and their enhanced catalytic activity in liquid phase reactions. One of the earlier reports by Sun and co-workers described the synthesis of tetrahexahedral (THH) Pd by applying square wave potential to polycrystalline Pd powder deposited on an electrode.[15] These THH Pd nanoparticles were found to be enclosed by {730} facets and thereby exhibited 4-6 times better catalytic activity than a commercial Pd black catalyst toward ethanol electro oxidation.[15] Fivefold twinned high index faceted Pd nanorods which were found to exhibit higher catalytic activity than the commercial Pd black catalyst was reported by Tian and co-workers.[16] Wang et al recently demonstrated the heteroepitaxial growth of Pd nanoshell on a high-index-faceted THH and trisoctahedral (TOH) Au nanocrystals. The grown Pd nanoshells were enclosed by {730} and {221} facets of the THH and TOH Au nanocrystals. These high-index-faceted Pd nanoshells showed higher catalytic activities than Pd nanocubes that are enclosed with the low-index {100} facets for the Suzuki coupling reaction.[17] Huang et al used a solvothermal method for the synthesis of Pd concave tetrahedral nanocrystals with exposed {110} and {111} facets.[18] Recently Xia et.al and Zheng et.al

73

reported a simple route for the synthesis of Pd concave nanocube which exposes {730} facets and vicinal {310} facets showing excellent electrocatalytic activity and good yield for Suzuki coupling reaction.[14,19] Wang and co workers presented a simple non seeded simple method for the synthesis of Palladium concave nanocubes.[20] Similarly, highly branched nanostructures are also promising candidates in catalysis as they possess larger surface area and surface roughness, while exposing specific (high index) crystal facets. Anisotropic palladium nanothorns synthesized by Meng and co-workers were found to exhibit better catalytic activities towards oxidation of formic acid.[21] A universal approach for the synthesis of noble metal nanodendrites using amino acid based surfactant was also recently reported.[22] These nanodendrites were found to expose {220} and {311} facets exhibiting good catalytic activity.

Palladium which is an important component in three way catalytic converter has been extensively studied for its CO oxidation properties.[23-24] Several aspects of chemical reactivity by palladium catalysts for CO oxidation have been demonstrated by using Pd single crystal model surfaces and on supported nanoparticles with size less than 6 nm.[25-29] The size dependence on CO oxidation was proved by several reports and one from Xia and co-workers needs special mention where a sub 10 nm Pd cubes/bars on ZnO nanowires showed 10 times higher activity than 18 nm Pd cubes. Palladium nanoparticles are also reported to show facet dependent chemical reactivity towards chemical reactions.[30] For example Zhao and co-workers demonstrated nanoparticle morphology to have a great influence on the CO oxidation trends.[31] Among the palladium nanoparticles supported on SiO_2, Pd octahedrons enclosed with {111} facet showed a much better performance towards CO oxidation than Pd cubes that exposed {100} facets. There is a growing interest in studying noble metal nanoparticles with exposed high index facets as they are found to show enhanced chemical activity than their low index counter parts. This can be attributed to the presence of special sites like step and kink atoms with unsaturated metal atom co-ordinations. Studies on model Pd single crystals to understand the role of defects were previously reported. A stepped single crystal surface Pd {335} was found to show more CO_2 production compared to flat Pd {111}.[32] Studies also showed that high degree of Pd steps can stabilize the metal phase and destabilize the oxide phase resulting in the oscillations and reactivity trends in CO oxidation.[26,27] It has been

proposed that the surface chemistry of the metal clusters (atomistic details like size and flexibility of the metal atoms constituting the cluster) were shown to influence the interaction with gas phase adsorbates in particular O_2 and CO.[33] An extensive literature search reveals that the gas phase chemical reactivity studies on high index faceted Pd surfaces is limited to single crystals whereas several reports are available on liquid phase reactions on high index faceted Pd nanocrystals. According to our knowledge a systematic report on the CO oxidation trends from high index faceted Pd nanoparticles is missing in literature. Recent success in morphology controlled synthesis of nanoparticles has motivated us to revisit the CO oxidation trends on Pd nanoparticles of different morphologies in order to gain further understanding on the size and shape dependence for this reaction.

Here, in this chapter a simple seed mediated approach for the synthesis of concave Pd nanocubes and Pd nanoflowers in aqueous medium and at room temperature which exposes high index facets is reported. This synthesis strategy shows a systematic evolution of concave Pd nanocubes and Pd nanoflowers using Pd nanospheres with size below 6 nm as seed. The palladium seeds obtained by the simple reduction of H_2PdCl_4 by $NaBH_4$ were used for the synthesis of Pd nanocubes. The nanocubes thus obtained were then used as the template for the formation of palladium concave nanocubes and nanoflowers. Even though this procedure involves three stages; the synthesis was done in aqueous medium at room temperature within 30 to 45 minutes of reaction time thus making it a convenient method for making such nanostructures. They were tested for gas phase CO oxidation and liquid phase coupling reaction to elucidate the structure sensitive chemical activity by Pd nanostructures.

3.2. Experimental

3.2.1. Reagents

Palladium Chloride ($PdCl_2$) (Sigma Aldrich), Cetyl trimethyl ammonium bromide (CTAB), Ascorbic acid (AA), Sodium bromide (NaBr), Sodium Borohydride (Spectrochem), Cetyl trimethyl ammonium chloride (CTAC) (Alfa Aesar), Darco G60 (Activated Carbon) were purchased and used as received. The water used in

all the experiments was ultrapure millipore water.

3.2.2. Synthesis of Pd nanospheres

H_2PdCl_4 solution (10 mM) was prepared by dissolving $PdCl_2$ 0.1773 g in HCl (0.2 M, 10 mL) and further diluting it to 100 mL with ultrapure millipore water. In a typical synthesis, 50 µL of H_2PdCl_4 solution (10 mM) was added to 7 mL, 75 mM CTAB solution. To this 900 µL of 0.1 M freshly prepared $NaBH_4$ solution was added while stirring. This resulted in palladium nanospheres and was used as seed solution for the further growth of nanocubes.

3.2.3. Synthesis of Pd nanocubes

About 300 mg of CTAB was dissolved in 10 mL of millipore water. To this, 125 µL of 10 mM H_2PdCl_4 solution, 10 µl of 0.01 M NaBr, 45 µL 0.1 M AA were added and mixed thoroughly by gentle shaking. Around 50 µL of Pd nanospheres seed solution was added and kept undisturbed. The solution gradually turned to black.

3.2.4. Synthesis of Pd concave nanocubes

In a typical synthesis, 5 mL of 5 mM CTAC solution was kept at 30 °C for 10 mins. Then Pd nanocube seed solution (40 µL for 47 nm, 80 µL for 37 nm, 100 µL for 23 nm), 100 µL of 0.1 M AA and 125 µL H_2PdCl_4 solution (10 mM) were added successively, mixed by gentle shaking and kept undisturbed. Within 10 mins the solution turned black indicating nanoparticle formation. The nanoparticles were designated as Pd concave cubes (~ 47 nm), Pd concave cubes (~ 37 nm) and Pd concave cubes (~ 23 nm) respectively.

3.2.5. Synthesis of Pd nanoflowers

In a typical synthesis, 5 mL of 5 mM aqueous CTAB solution was kept at 30 °C for 10 mins, Then Pd nanocube seed solution 40 µL, 100 µL of 0.1 M AA and 125 µL H_2PdCl_4 solution (10 mM) were added successively, mixed by gentle shaking and the reactants were left undisturbed. The formation of black solution within 10 mins indicated the formation of nanoparticles.

3.2.6. Synthesis of supported Pd Nanoparticles

Desired amount (10 mg) of support $MgO/CeO_2/TiO_2/$ with surface area 70 m^2/g, 83 m^2/g, 55 m^2/g was added to the Pd nanocube and Pd concave nanocube and Pd nanoflower colloid solution. The slurry formed was stirred

for 2 h, centrifuged, washed with water and dried at 100 °C and calcined at 300 °C for 5 h.
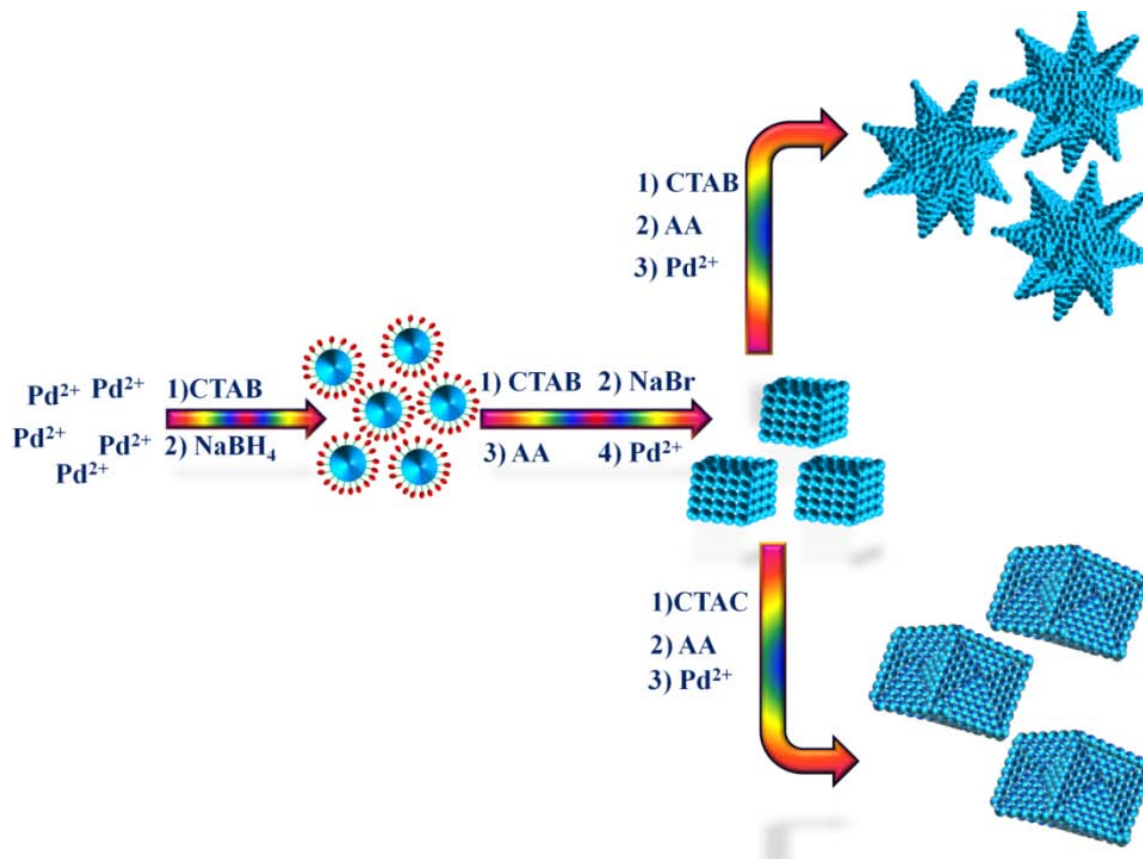
Scheme 3.1: General scheme for the evolution of palladium concave nanocubes and nanoflowers from a spherical seed.

3.2.7. Synthesis of Palladium Nanospheres of larger size

In a typical synthesis, 1 mL of 0.1 M $PdCl_2$ solution was mixed with 10 mL, 12.5 mM CTAB at 30 °C for 10 mins. Then 2 mL of 0.1 M $NaBH_4$ solution was added drop wise while stirring. Stirring continued to remove excess of $NaBH_4$.

3.2.8. Characterisation

The as synthesised catalysts were isolated by centrifugation at 10000 rpm and characterised by transmission electron microscope (TEM, TECHNAI FEI operating at 300 keV), powder X-ray Diffraction (XRD, PAnalytical X pert pro dual goniometre diffractometer) working at 40 kv and 30 mA with Cu Kα source and with Varian Cary 50 Conc UV-Visible spectrophotometer. The ICP analysis was done using Spectro Arcos ICP-OES. The products of Suzuki reaction and Heck reaction were analysed by Agilent N6890 GC.

3.2.9. Catalyst testing

a. Suzuki Coupling

A 25 mL RB flask with 4 mL ethanol and 1.5 mmol of phenylboronic acid was charged with 1 mmol iodobenzene. Then 1.5 mmol K_2CO_3 and 100 µL (0.1 mg of Pd by calculation or 100 mg of Pd nanostructures supported on activated carbon were added. The medium was kept at 80 °C for 1 h under magnetic stirring.

b. Heck Coupling

A 25 mL RB flask, which contained 0.21 mL (1.5 mmol) styrene, was charged with 0.11 mL (1 mmol) iodobenzene. Then 1.5 mmol K_2CO_3 and 100 µL (0.1 mg of Pd by calculation) or 100 mg of Pd nanostructures supported on activated carbon were added. The medium was kept at 120 °C for 1 h under magnetic stirring. The products of both reactions were analysed using gas chromatogram.

c. CO oxidation

The catalytic activity of supported Pd nanostructures for CO oxidation was measured in a fixed bed reactor under atmospheric pressure using 100 mg pelletized catalyst. The total flow rate was 50 ml/min with a ratio of (1:5:19 CO: O_2: N_2) with a temperature range of 40 °C to 300 °C. The calculated GHSV was 30000 cm^3/g_{cat}/h. The reactor was placed in a tubular furnace and temperature of the furnace was controlled by Radix6400 temperature controller. The catalyst bed temperature was measured by a K-type thermocouple. The effluent gases were analysed online by gas chromatograph equipped with online gas sampling valve and a TCD detector. The activity was examined by looking at the CO conversion.

3.3. Results and Discussion

3.3.1. Transmission electron microscopy

a. Pristine nanoparticles

The systematic evolution of Pd nanospheres to nanocubes and then to concave cubes and nanoflowers is reported. By changing the surfactants used in the synthesis strategy, the shape of the nanoparticles was controlled. The first step in this sequential nanostructure synthesis is the formation of palladium seeds. In Figure

3.1a the TEM image of the palladium seed obtained during our synthesis is shown. They are mostly composed of spherical particles with size below 6 nm. These spherical palladium nanoparticles were used to prepare palladium nanoparticles of other morphologies using a seed mediated synthesis procedure. Accordingly, in the second step the spherical Pd nanoparticles were transformed to nanocubes at room temperature with fairly good yield
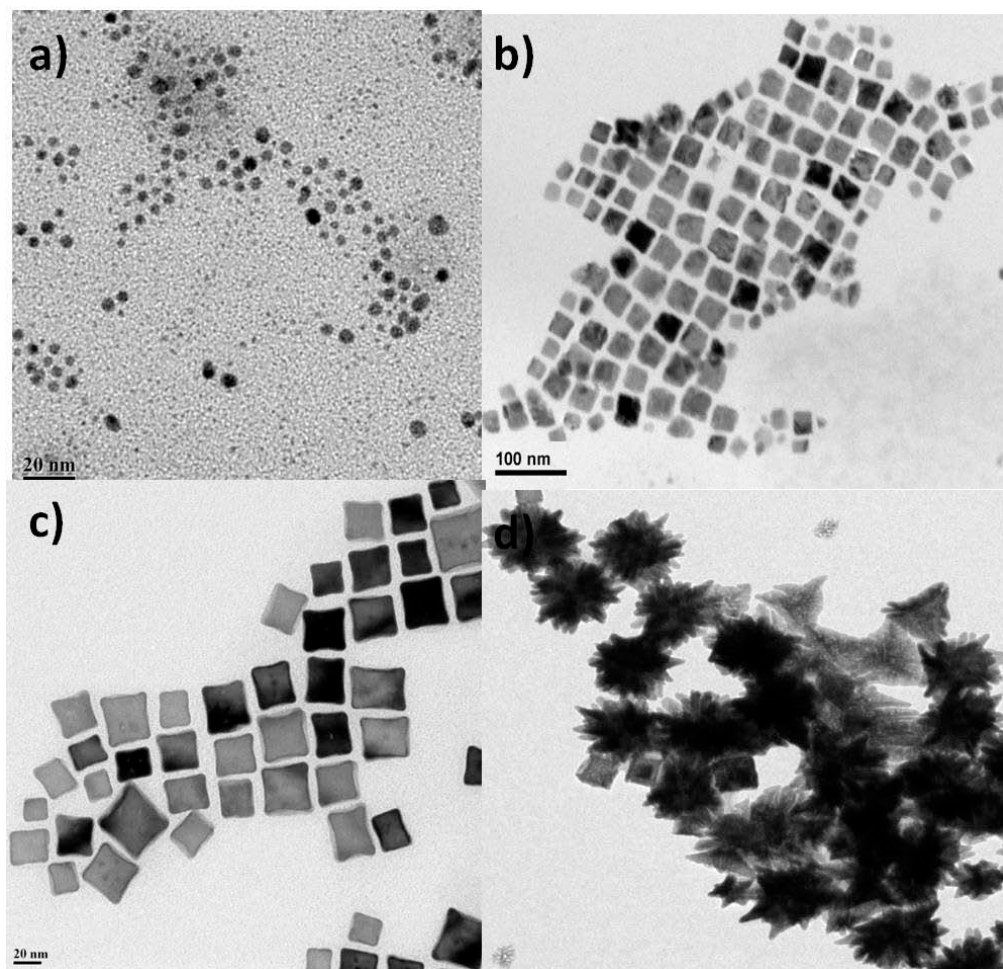
Figure 3.1: The TEM image showing a) spherical Pd nanoseeds, b) Pd nanocubes, c) Pd concave anocubes and d) Pd nanoflowers.

The TEM image in Figure 3.1b shows that the Pd nanocubes are in the size ranging from 20 nm to 35 nm with particles mostly in the size range 20 nm. The TEM image also showed some spherical particles which are from the unreacted seed particles. The novelty of the procedure adopted here is that they are prepared at room temperature and in aqueous medium using Br⁻ as the structure directing agent. These palladium nanocubes were

used as seed for making other nanostructures at room temperature. The binding property of ions in surfactants like CTAB and CTAC to specific facets of the nanocube was utilised to achieve shape control. A concave nanocube can be considered as a cube with centres of the six faces pushed inside to form square pyramid likedepressions. In Figure 3.1c the TEM image of the concave nanocube obtained during our synthesis with an average particle size of 37 nm is shown.
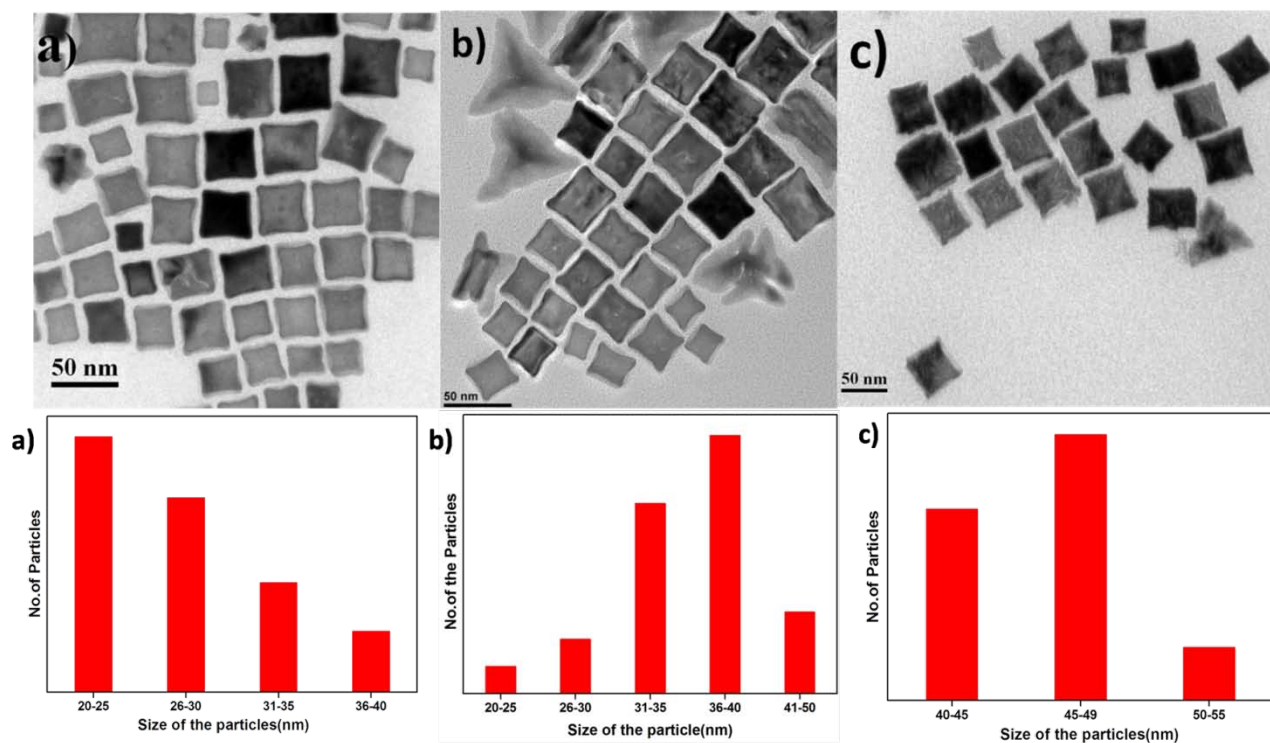
Figure 3.2: TEM image of different sized Pd concave cubes a) Pd concave cubes (~ 23 nm), b) Pd concave cubes (~ 37 nm) and c) Pd concave cubes (~ 47 nm) and the corresponding histogram.

The size control was achieved by changing the amount of seed solution used in the growth stage. Thus by changing the volume of the seed solution that was added to the growth (40 µL for 47 nm, 80 µL for 37 nm, 100 µL for 23 nm) concave nanocubes of varying sizes as shown in Figure 3.2 were achieved. From Pd nanocubes, by changing the surfactant in the growth stage from CTAC by CTAB of similar concentration Pd nanoflowers were obtained instead of concave nanoparticles (Figure 3 1d).

The high resolution microscopic analysis revealed that the surface of concave cube exposes high index facets carrying periodic step sites. In Figure 3.3 an individual concave nanocube with characteristic depressions at

each of the faces thereby forming the concave structure is shown. For a concave nanocube enclosed by high-index facets, the Miller indices can be derived from the projection angles along a selected crystallographic axis.[34-35] From the TEM image, the angle between {100} facets and concave facets was measured to be 18° (see Figure 3.3b). This value is consistent with the theoretical angle between {310} facets and {100} facets (i.e. 18.4°). The theoretical angle can be calculated using the formula, the projection angle $\alpha = \arctan (k/h)$ for a given (hkl) value.[14] The {310} facets consist of (100) terraces and (110) steps. Clearly, the HRTEM image (see Figure 3.3c) from one of the edges of the concave nanocube showed the presence of steps and terraces. The high resolution image also show crystal lattice fringes with d value of around 0.20 nm for a Pd (100) plane. The atomic model of {310} is shown in Figure 3.3 d.
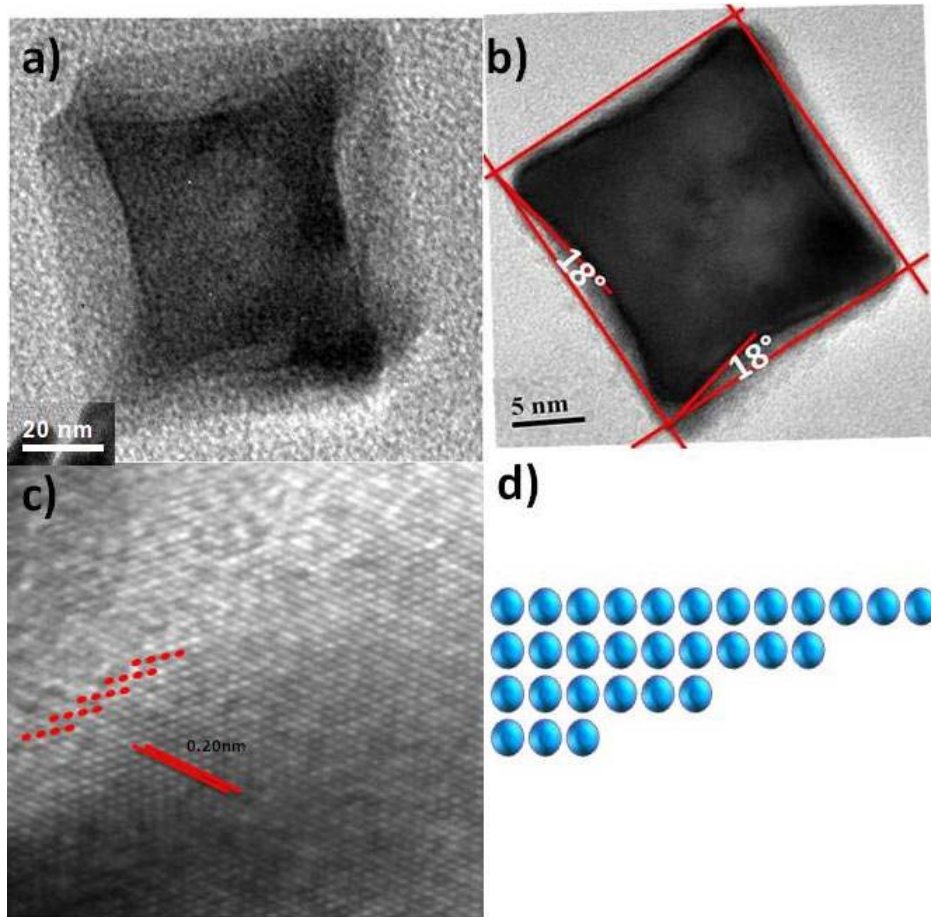
Figure 3.3: a) A single concave nanocube, b) the calculation of the angle between the {100} facet and a concave facet, c) one of the edges showing the steps and terraces along with the lattice fringes and a d spacing of 0.20 nm and d) scheme showing the atomic arrangement of {310} facets.

Highly branched nanostructures are ideally suited for catalysis as high surface area and the presence of high index facets can lead to enhanced catalytic activity. In Figure 3.4a the TEM image of a Pd flower with its receptacle and the different petals is shown. A closer look with TEM showed the surface of the nanoflower to be highly corrugated (see Figure 3.4b). The atomic details of one of the corrugated edges of Pd nanoflower are presented in Figure 3.4c which clearly showed the presence of monoatomic steps. The edges were found to consist of {311} facets which is made up of {100} terrace and {111} steps as reported as shown in Figure 3.4 d and reported previously.[36] In Figure 3.5 the TEM image of low index faceted nanoparticles used in control experiments is also shown.
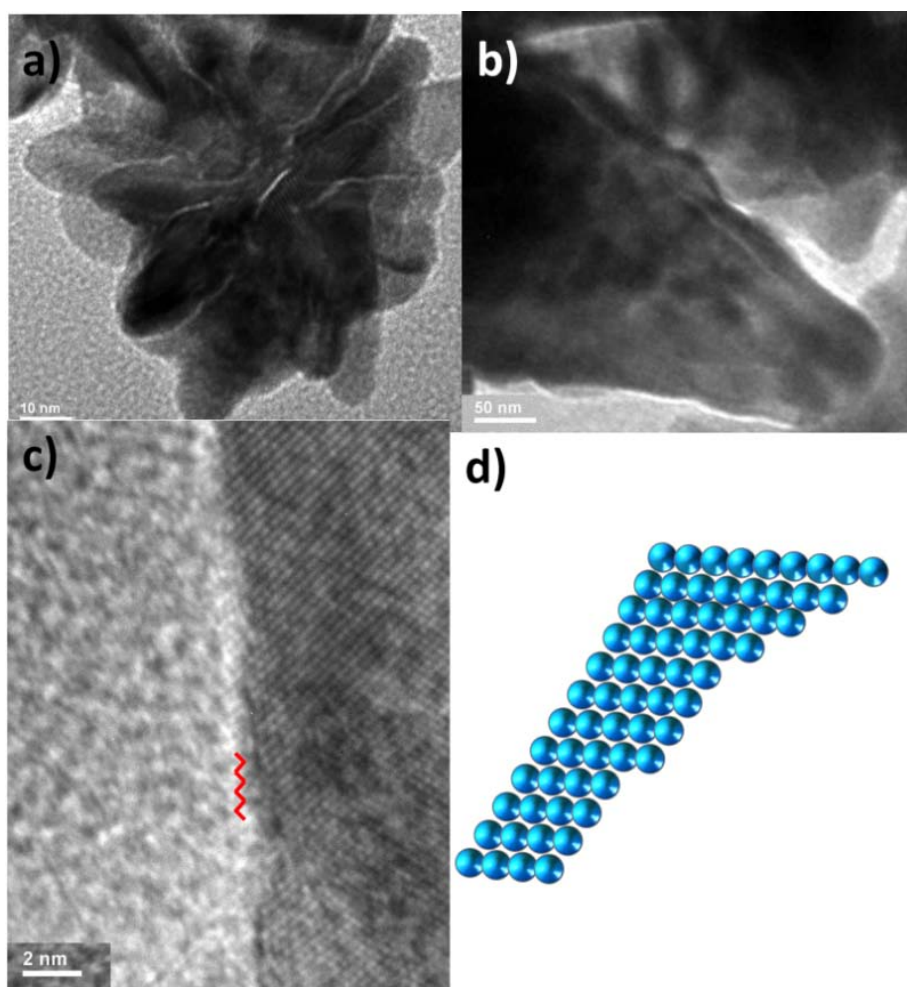
Figure 3.4: TEM image of a) one of the nanoflowers with its receptacle and its petals, b) image showing one of the petals with corrugated steps, c) HRTEM image showing step and terraces and d) atomic model of {311} facets.

For CO oxidation activity of the nanostructures, they were supported on oxide supports like MgO, ceria and titania which are reducible active supports and on activated carbon and silica which are inert supports and the catalytic activity of high index faceted Pd concave cubes and nanoflowers were compared with flat low index faceted nanostrutures of similar size (see Figure 3.5).
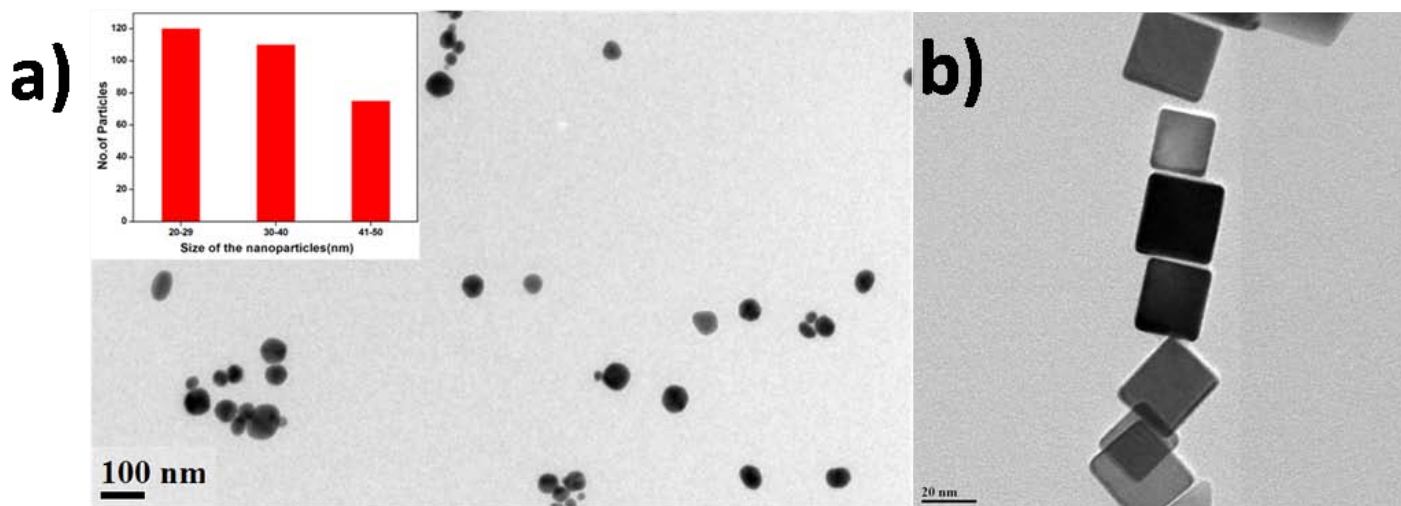
Figure 3.5: TEM image of a) spherical palladium nanoparticles and b) cubes which was used in control experiments.

b. Supported Pd nanostructures

TEM image of the as synthesized Pd concave nanocubes with an average particle size of 37 nm is shown in Figure 3.6a along with the image of supported Pd concave cube (~ 37 nm) on MgO in Figure 3.6b. The contrast difference of the Pd concave cube on MgO support can be clearly noticed from the TEM image. It can be inferred that the morphology of the nanoparticle is retained even after immobilizing on MgO support followed by calcination at 300 °C. The ceria and TiO_2 supported concave cubes are shown in Figure 3.6c and d. Figure 3.7a shows the as-synthesized Pd nanoflowers and MgO supported Pd nanoflowers with a size of approximately 100 nm. The nanoflowers with their petals and the receptacle are shown in the TEM image (Figure 3.7b). Detailed high-resolution TEM as in Figure 3.7c showed the petals to carry {311} atomic sites.
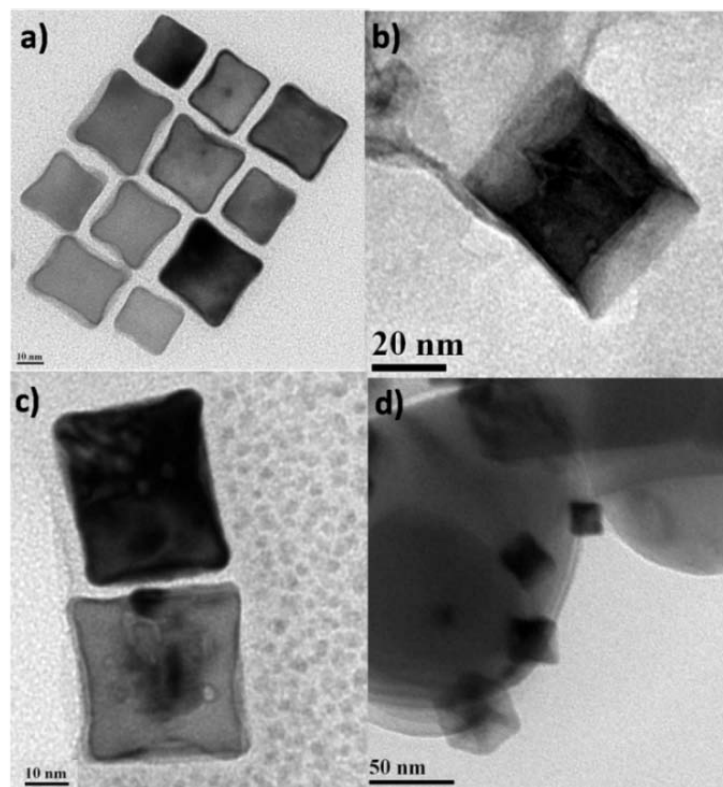
Figure 3.6: The TEM image showing a) as-synthesized Pd concave cubes (37 nm), b) a Pd concave cube supported on MgO, c) Pd concave cubes (~ 37 nm) supported on CeO_2 and d) Pd concave cubes (~ 23 nm) on TiO_2 after calcination.

The formation of Pd nanoparticles with different morphologies can be attributed to the interplay between the selective face blocking tendency of the stabilising agent and the reduction kinetics i.e. the rate at which Pd^0 is supplied to the crystallographic planes of the palladium nanoparticle. The nanocube growth solution also contains an excess of Br^- ions which more strongly bind with {100} facets than with the {111} facet of the spherical nanoparticles. Thus the reduced Pd atoms in solution preferentially grow on the {111} facet and cause their disappearance resulting in the formation of nanocubes with exposed {100} facets.[37] In the case of the concave nanocube and nanoflower synthesis, an excess of either CTAC or CTAB in the growth solution was used. The growth in this case can be understood in terms of the binding properties of Cl^- and Br^- on the {100} facets.[38-39] Since Br^- strongly binds to the {100} facet the only accessible sites for the reduced Pd atoms are {110} and {111} edges and corners and mostly the {111} edges resulting in nanoflowers. Since Cl^- is weakly

bound on the {100} facet when compared to Br⁻ some growth on this facet could be seen resulting in concave nanocube structures. Since the reduction rate is greater than the surface diffusion rate of the particle, the newly formed atoms will not move to the side faces and grow from the edges and corners resulting in either palladium concave nanoparticles or nanoflowers depending on the ions in the growth solution.[40-41]
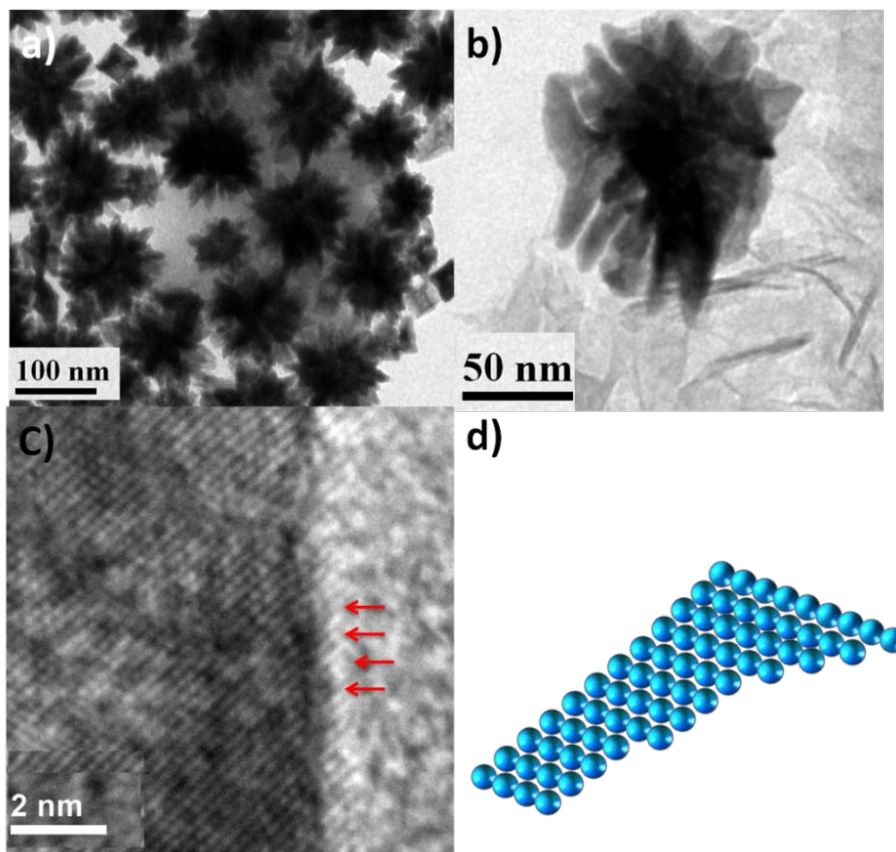
Figure 3.7: The TEM image showing a) as-synthesized Pd nanoflowers; b) MgO supported nanoflower; c) the atomic arrangement along the edge of the petal and d) an atomic model of {311} showing the geometry of defect sites.

So by carefully manipulating the reaction conditions, nanostructures with different shapes have been synthesised. A general scheme for the transformation of palladium nanocubes to concave nanocubes and nanoflower is shown in Scheme 3.1. To garner knowledge on the structure sensitivity, spheres were also synthesised and used for control experiment. The TEM image from MgO supported spherical Pd particle is shown in Figure 3.8.
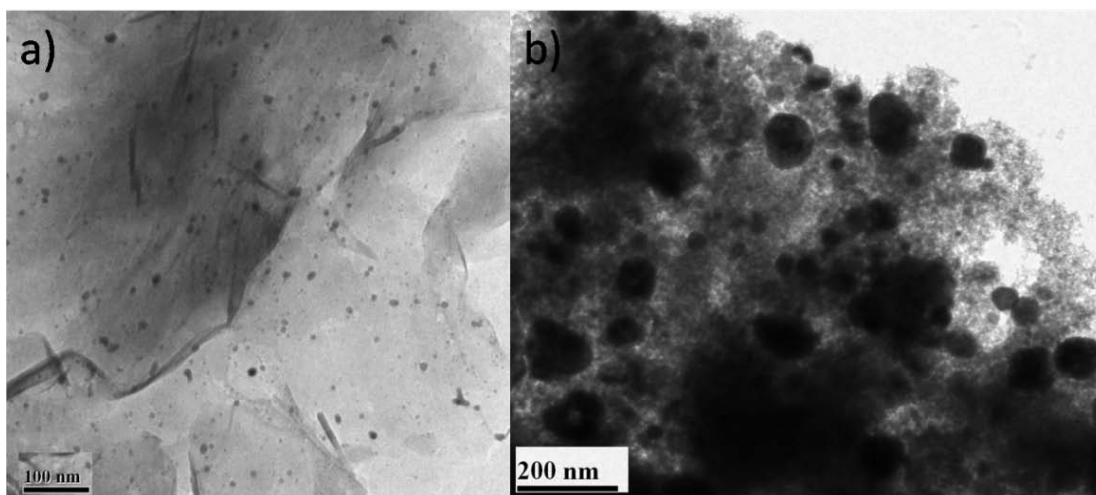
Figure 3.8: TEM image of a) Pd spherical seeds(less than 6 nm) supported on MgO and b) Pd spheres of size around (~ 35 nm) used in the control experiments.

3.3.2. X-ray Diffraction

The corresponding XRD patterns shown in Figure 3.9 indicated palladium to be metallic in nature and exhibiting typical reflections from a fcc lattice. The XRD pattern shows the reflections at 40.5°, 46.8°, 68.4°, 82.3° corresponding to the (111), (200), (222), (311) facets.
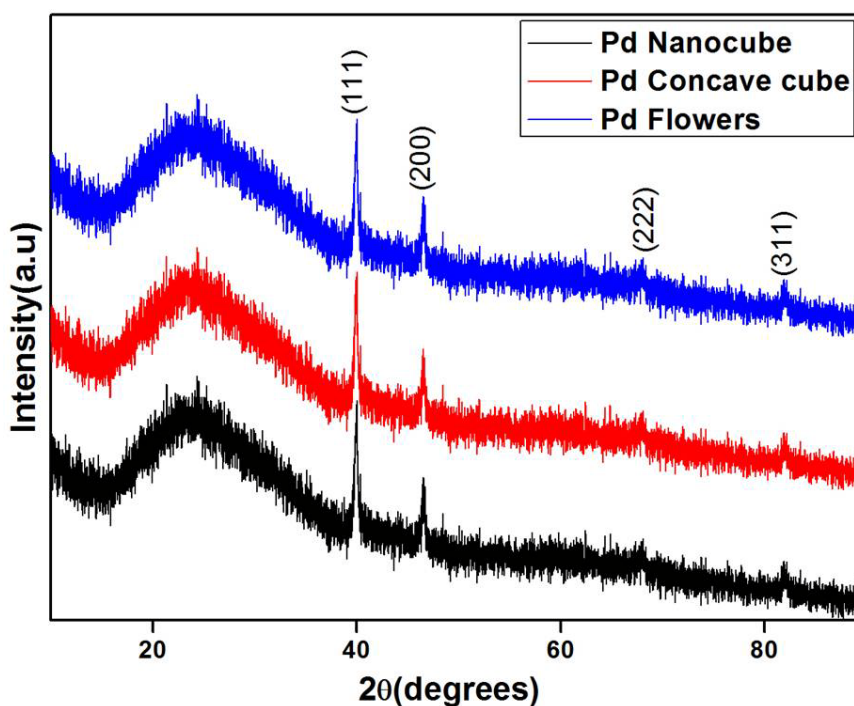
Figure 3.9: XRD spectrum of different pristine Pd nano structures.

The supported catalysts were also analyzed using a powder X-ray diffraction technique, and the corresponding XRD profile is shown in Figure 3.10. The Figure 3.10a shows reflections from MgO (JCPDS [78-0430]) and $Mg(OH)_2$ (JCPDS[84-2167]) indexed by the open and closed circles respectively. The inset shows the reflection at 40° corresponding to Pd (111) facets. The formation of $Mg(OH)_2$ under our immobilization conditions could not be prevented but calcination at higher temperature in air at 500 or 650 °C was able to remove these hydroxides. The XRD analysis for Pd concave cubes and nanoflowers supported on ceria and titania is also reported here (see Figure 3.10b and c).
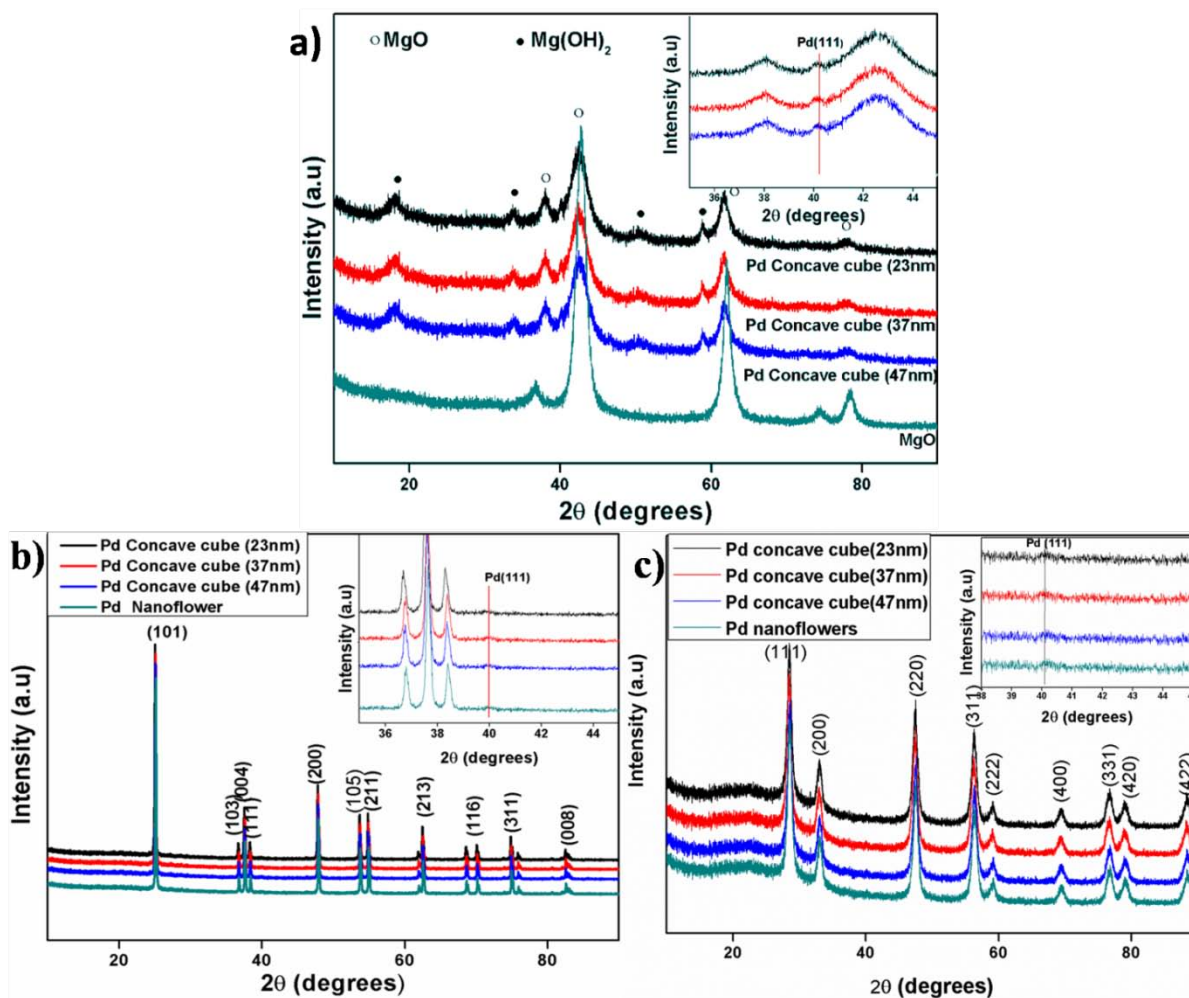
Figure 3.10: The XRD showing the reflections of a) Pd concave cube/MgO catalysts. The peak corresponding to both MgO and $Mg(OH)_2$ is observed. The inset shows the reflection of Pd (111) b) and c) nanostructures supported on ceria and titania.

3.3.3. UV-Visible spectroscopy
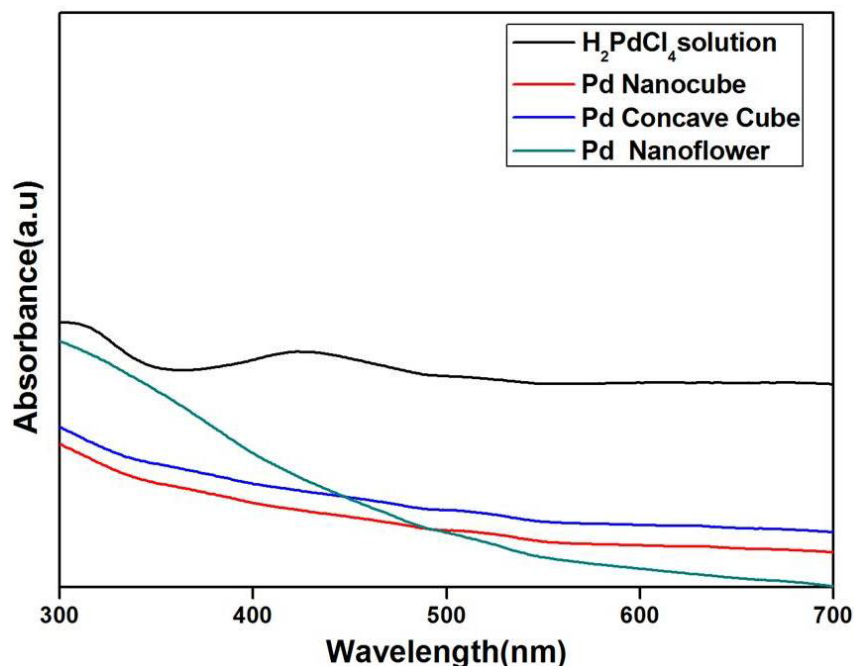
Figure 3.11: UV-Visible spectrum of different Pd nano structures.

UV-Visible is an effective method to investigate whether the metal precursors are reduced or not. The Figure 3.11 shows the UV-Vis spectrum of H_2PdCl_4 solution and the spectrum of Pd concave cubes and flowers. The absorption at 309 nm and 423 nm is due to the charge transfer from ligand (Cl^-) to the Pd^{2+} ions. When reducing agent was added the peaks disappeared showing the formation of Pd nanoparticles. No new peak emerged as Pd is not having any SPR in UV-Vis region.

3.3.4. Catalyst activity testing

One of the major goals of synthesizing the palladium nanostructures was to understand the size and structure sensitivity of reactions catalysed by this metal. The as synthesised palladium cubes, concave cubes, nanoflowers and spherical nanoparticles were evaluated by testing the catalytic activity for bench mark reactions like CO oxidation and coupling reactions.

3.3.4.1. Coupling Reactions: Suzuki and Heck Coupling

In a typical Suzuki coupling reaction phenyl boronic acid is coupled with iodobenzene using different morphologies of palladium nanoparticles. After 1 h of reaction, the as synthesised palladium concave nanocubes

catalyst (23 nm) gave a conversion of 95% of iodobenzene to biphenyl. The conversions achieved in this case were similar to palladium nanoparticles of approximately 5-6 nm and to previous reports on concave cubes.[14] The Suzuki reaction was also carried out on palladium concave nanocubes of bigger sizes (37 and 47 nm) and showed good catalytic activity. The results are summarized in the Table 3.1.

No.	Catalyst	% Conversion [a]	TOF (x 10^{12}) s^{-1}	% Conversion [b]	TOF (x 10^{12}) s^{-1}
1	Pd concave cube (~ 23 nm)	95	11	76	8.8
2	Pd concave cube (~ 39nm)	96	19.1	80	15.9
3	Pd concave cube (~ 47 nm)	97	23.8	84	20.1
4	Pd cubes (~ 20 nm)	48	3.8	34	2.6
5	Pd spheres (~ 35 nm)	55	4.3	48	3.7
[a] Suzuki Coupling and [b] Heck Coupling					

Table 3.1: Table showing the % conversion and TOF for Suzuki coupling and Heck coupling done with different palladium catalysts.

To compare the reactivity with low index surfaces, the same reaction under similar conditions was tested on 20 nm palladium nanocubes. Unlike concave nanocubes, the simple nanocube analogues are exclusively bound by {100} faces without any defects. In this case the conversion achieved was only 48%, thus proving beyond doubt attributing the supreme activity on concave nanocube to the high density of step atoms present on their surface. The marginal activity shown by conventional cubes may be due to the presence of edge and corner atoms present on the cubes. Further, the Suzuki coupling reaction was carried out on Pd nanoflowers which our TEM analysis showed considerable density of step atoms. In this case the activity achieved was similar to that of

concave nanocubes with conversion reaching around 99%. As a control experiment, Pd nanospheres of approximately 30 nm was synthesized and tested for Suzuki reaction which gave only 55% conversion.

Previous literature report suggests Suzuki reaction to be size dependent with size below 10 nm found to be catalytically more active.[42] It should be noted that the nanoparticle systems, even though the size was above the optimum, gave a comparable activity to that of conventional catalyst. This activity can certainly be attributed to the presence of high density of step atoms in concave nanocubes and nanoflowers.

The Pd nanostructures synthesized were also tested for Heck coupling, where iodobenzene was coupled with styrene to form trans-stilbene. It is already reported that the Pd-metal catalyzed Heck coupling of aryl halides with olefins is a structure-sensitive reaction and the Pd sites responsible for high activity are those with metal atoms with low coordination number.[43] So the catalyst with high index facets (i.e. with high density of under co-ordinated atoms) was expected to give a good conversion even though the particle is well above the optimum size of 5-6 nm. It was remarkable to note that palladium concave nanocube of approximately 47 nm showed a conversion of around 84% with smaller sizes also being equally active. The high index Pd nanoflowers also showed around 85% conversion towards trans-stilbene. As a control experiment the chemical activity of Pd concave nanocubes and nanoflowers were also compared with that of Pd nanospheres of size around 30-35 nm. Here, The Pd nanospheres showed a conversion of about 48% for Heck coupling reaction. This again proves that the defects are responsible for the observed high activity for the reaction, and the reactions are shape dependent and size independent.

a. Turn over frequency calculations

The nanoparticle systems like (concave) nanocubes reported here are truly model and ideal to calculate the dependence of reactivity on the specific exposed surface atoms. For this the total surface atoms to volume ratio per particle for three different concave nanocubes which were the most active in both the reactions were calculated and its dependence on the TOF was plotted (for TOF calculation see appendix of the thesis). Similarly, the total number of step atoms along the edge per particle of concave nanocubes was also calculated and plotted against the TOF. The calculations on palladium nanoflowers were not attempted as the calculation

of surface atoms were difficult due to the complex surface structure of the nanoflowers. The results from concave nanocubes of different sizes shown in Figure 3.12 clearly demonstrate distinctly different dependence on the rate. It can be seen that as the size of the concave nanocube increases the surface to volume ratio decreases dramatically. Thus a 47 nm palladium concave nanocube, in spite of having smaller surface to volume of Pd atoms compared to a 23 nm particle showed better reactivity. This is interesting as the general trend in nanocatalysis is the observation of enhanced reactivity with decreasing size.[44] From the curve it can also be inferred that TOF values did not show a linear dependence towards the total surface to volume of Pd atoms. On the other hand a plot of the total number of surface step atoms along the edge per particle (shown in Figure 3.12) showed a linear increase on the calculated TOF values with size for the reactions studied. Such linear correlation clearly indicates that the step atom density has a direct bearing on the observed enhanced catalytic activity of the two reactions studied over palladium concave nanocubes.
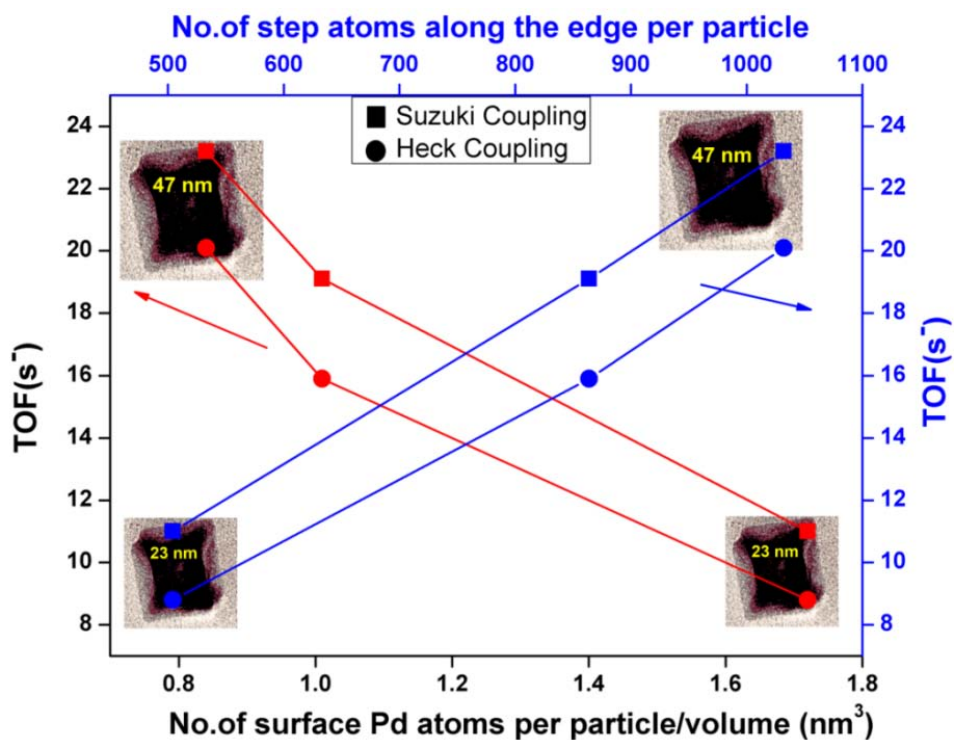
Figure 3.12: The plot of turn over frequency (TOF) for Suzuki and Heck coupling reactions against the Pd surface atom to volume ratio of a particle and step atom density along the edge of the palladium concave nanocubes of different sizes.

b. Spent Catalyst Analysis

The liquid phase catalytic transformations were carried out at elevated temperature at 80 °C and 120 °C respectively, the morphology of the nanoparticles after the reaction was investigated using TEM. Interestingly, the Pd nanoparticles in both catalysts maintained their morphologies during the catalytic reaction, as revealed by TEM imaging shown in Figure 3.13. The presence of some isolated nanoflower like structures was observed in the case of concave nanocubes. These could be formed during the course of the catalytic reaction as such structures were not present before the reaction.
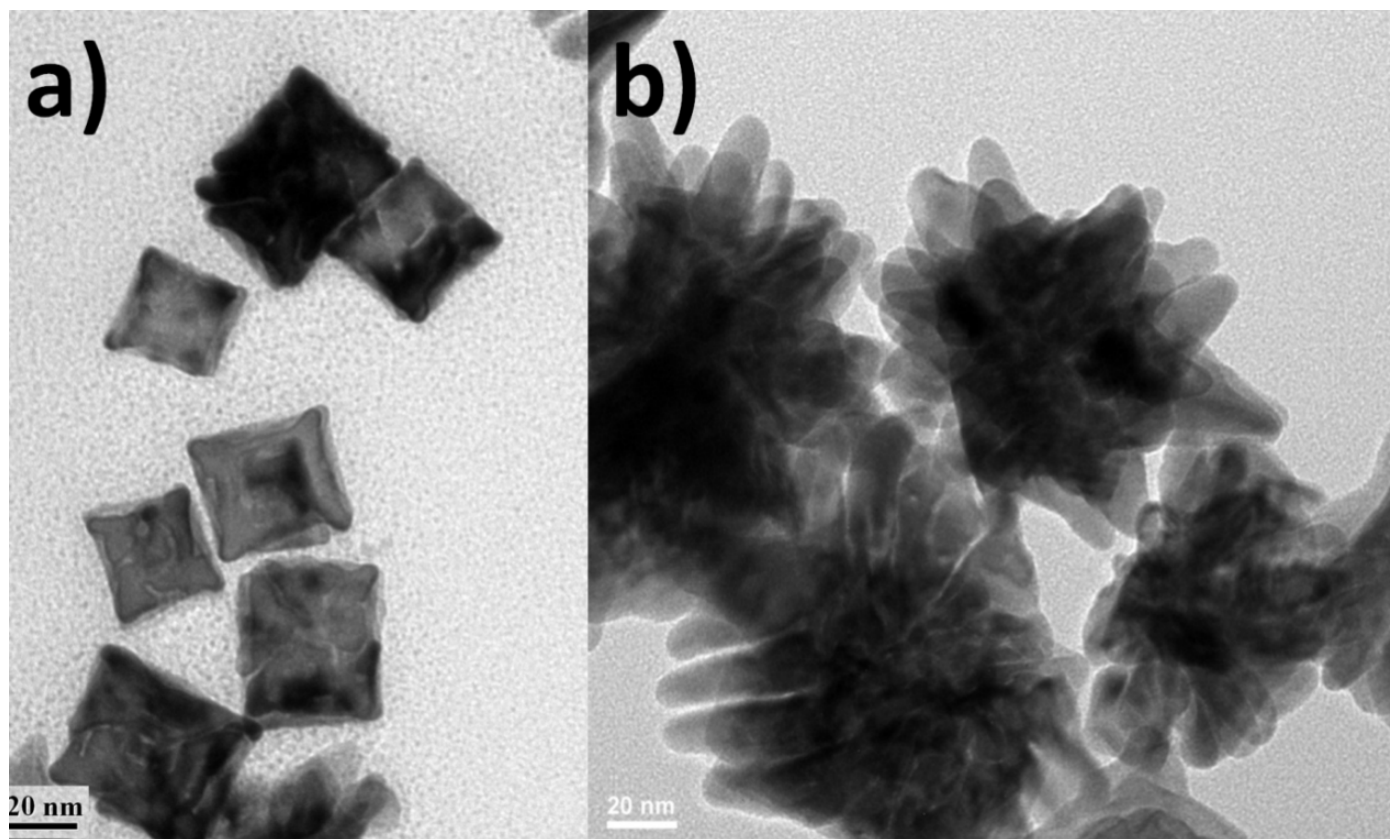
Figure 3.13: The TEM image of the catalyst a) concave nanocube and b) nanoflowers after Heck coupling which shows that morphology is retained.

3.3.4.2. CO oxidation activity

a. Structure dependent CO oxidation on Pd nanostructures

To garner further knowledge on structure sensitivity of these nanostructures, the supported nanoparticles were tested for CO oxidation reaction. In Figure 3.14 the CO conversion plot for Pd concave nanocubes (47 nm) and

Pd nanoflowers (~ 100 nm) supported on MgO is shown. The CO oxidation was found to be facile on the Pd concave nanocubes, and nanoflowers with onset temperatures at 140 °C for 47 nm Pd concave cube and nanoflowers respectively. The full conversion for these catalysts was achieved at around 200 °C and 190 °C respectively. This activity profile demonstrated the role of coordinatively unsaturated atoms in the form of steps on the surface of Pd concave nanocubes and nanoflowers which exposes {310} and {311} high index planes. To compare the CO oxidation activity of these high index faceted Pd nanostructures, Pd nanoparticle systems with different sizes and morphology was investigated. As a first comparison the CO oxidation activity of Pd cubes of size 30 nm supported on MgO was studied. Unlike concave nanocubes and nanoflowers, surface of a simple cube is expected to carry minimum amount of under co-ordinated atoms (mainly from the edges) which can impart slightly improved reactivity compared to spherical particle of similar size. This is indeed reflected from the CO oxidation profile shown in Figure 3.14, where an onset temperature of 200 °C and full conversion temperature of 270 °C was observed which is far below as that demonstrated by concave nanocubes and nanoflowers. The reactivity of supported Pd nanocubes from this study is in agreement with the work of Xia et al where an 18 nm Pd cube on ZnO showed an onset of 160 °C and full conversion at 260 °C.[30] To further investigate the size and shape dependence of CO oxidation on Pd nanostructures, reactions on Pd nanospheres of 6 nm and 35 nm supported on MgO was carried out. The Pd nanospheres of size ~ 35 nm showed an onset temperature of 190 °C and did not achieve full conversion until 300 °C with a maximum conversion being 35%. A self consistent DFT calculation study by Norskov and co-workers clearly indicate that the step density continuously increases as particle size decreases.[45] They predict that the concentration of step edge sites to be minimal for a spherical cluster size above 10 nm. The residual activity and higher onset temperature of our 35 nm spherical Pd nanoparticles can be attributed to these marginal sites explaining the structure sensitivity of CO oxidation on supported Pd nanoparticles.

Figure 3.14: The conversion plot showing the CO oxidation activity of Pd concave nanocubes (47 nm) and Pd nanoflowers (100 nm) supported on MgO. The performance of spherical seeds, cubes, and spheres is also compared.

From the previous CO oxidation studies, it is clear that the optimum size for activity is found to be around ~ 5 nm.[25] To test and compare the activity of Pd concave nanocubes, Pd nanoparticles of ~ 5-6 nm was synthesised and supported on MgO. The CO oxidation profile from 6 nm particles in (Figure 3.14) showed a light off temperature at 160 °C with full conversion at 220 °C. On comparison it can be concluded that supported Pd concave nanocubes (47 nm) and Pd nanoflowers showed a lower onset temperature for CO oxidation compared to the supported Pd nanospheres of size less than 6 nm. This is in agreement with the report of Cuenya et al on the importance of under coordinated Pt surface atoms, where a decrease in the onset temperature for 2-propanol oxidation was observed with increase in the number of dangling bonds on the Pt nanoparticle surface.[5] Pd nanoparticles of size 3-5 nm on different oxide supports were found to show an onset temperature at around 100 °C and full conversion at around 200 °C.[25] Microporous polymer supported Pd nanoparticles with size 2.7 nm

and with a Pd loading of 0.9 wt% showed a T_{50} at 205 °C and maximum conversion at 220 °C.[46] These values are comparable with Pd concave cube (47 nm) where T_{50} was around 180 °C with a temperature of full conversion at 200 °C even though size was 10 times larger than the reported one. In another study, the light-off temperatures of CO oxidation over Pd (octahedron) (22 nm)/SiO_2 and Pd (cube) (23 nm)/SiO_2 catalysts were 250 °C and 320 °C, with the complete CO conversion temperatures at around 290 °C and 370 °C respectively.[31]

b. Effect of support
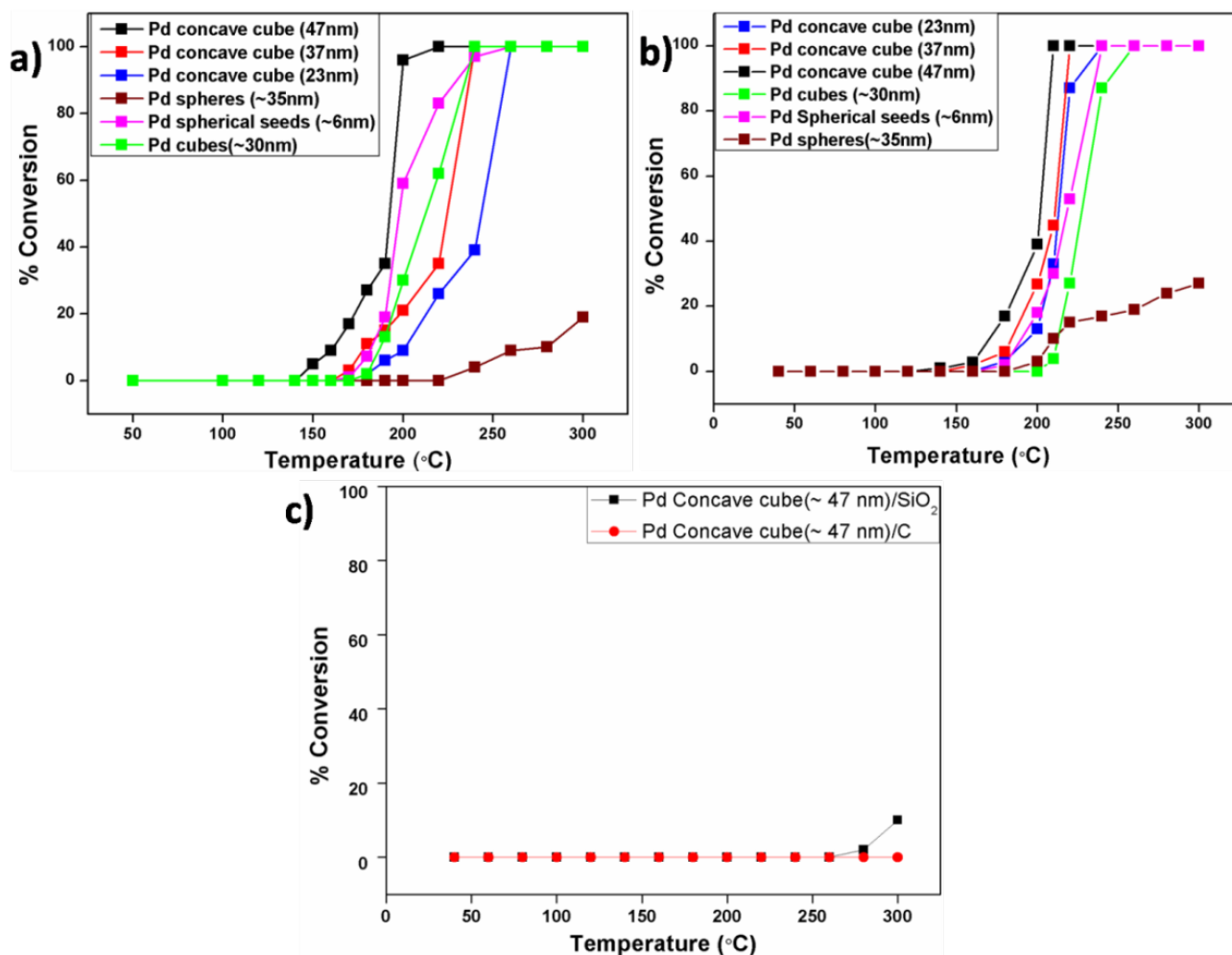
Figure 3.15: The CO oxidation plot for Pd nanostructures supported on a) CeO_2, b) TiO_2 c) Pd concave cubes (~ 47 nm) supported on carbon and silica.

The effect of support in the CO oxidation rates is inconclusive and has been debated in literature. For example, the CO oxidation by Pd nanocubes recently reported by Qiu et al showed that a basic support like MgO outperform others in the chemical activity.[47] The CO oxidation by Pd nanoparticles with size less than 10 nm is

extensively studied on different supports like SBA-15,[48] Al_2O_3,[49] TiO_2,[50] FeOx,[51] CeO_2.[23,52] In this context, Pd concave nanocubes were supported anatase TiO_2 as well as on ceria and tested for CO oxidation to probe the role of support (see Figure 3.15 for the conversion plot). In the present study, the catalysts showed a similar trend on the active supports used, with larger sized Pd concave nanocube (47 nm) showing a marginally better activity in all the three supports. The CO oxidation activity profile of Pd concave cubes (~ 47 nm) was also tried by supporting them on activated carbon and silica. They were found to show no or minimal activity at 300 °C (See Figure 3.15c). The slightly enhanced activity for Pd concave cube (~ 47 nm) than 37 nm and 23 nm can be attributed to the better morphological stability.

c. **Size dependent CO oxidation on Pd nanostructures**
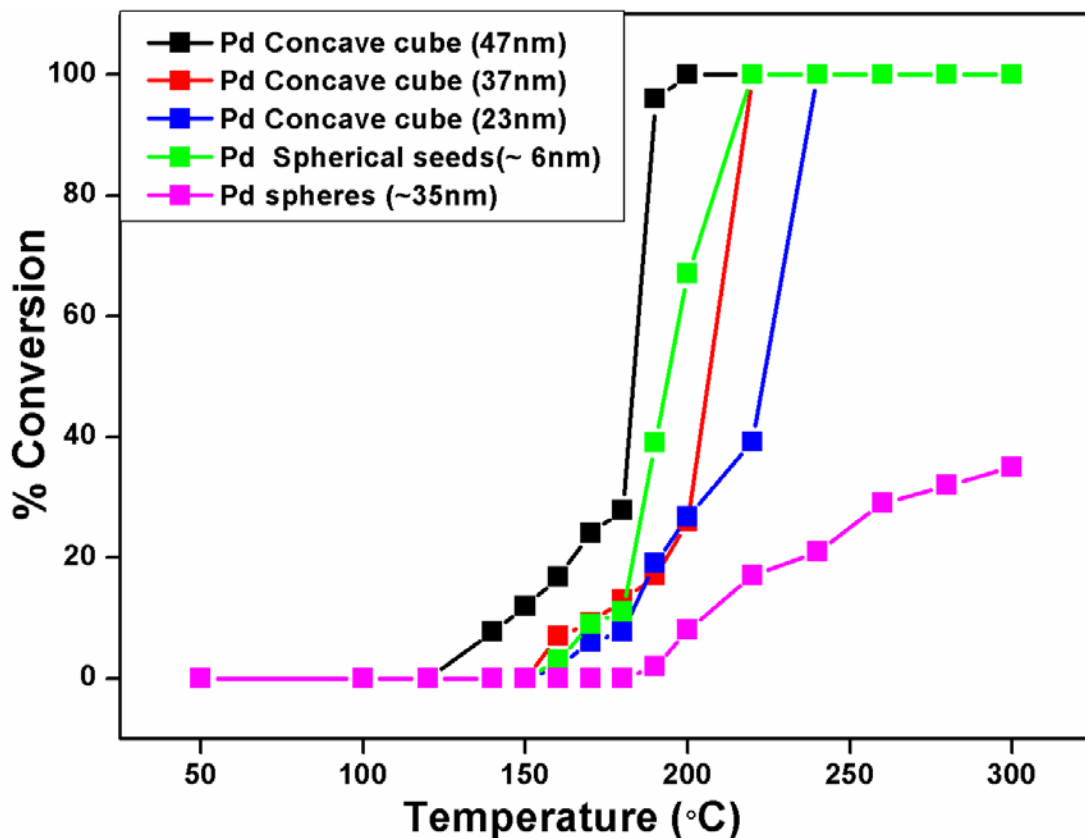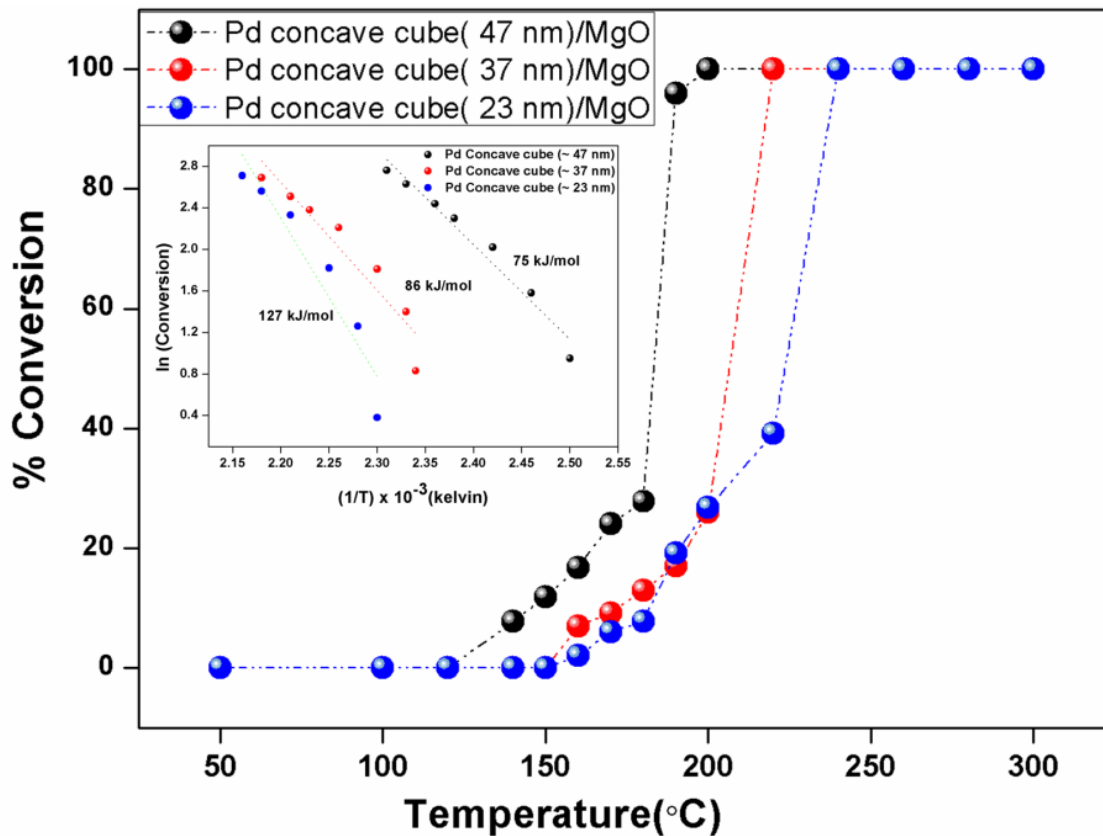

Figure 3.16: The conversion plot showing the CO oxidation activity of Pd concave nanocubes (47 nm) and Pd nanoflowers (100 nm) supported on MgO. The performance of spherical seeds, cubes, and spheres is also compared.

The size dependency of Pd concave cubes for CO oxidation was also studied by probing the activity for Pd concave cubes of size 23 nm and 37 nm and results were compared with the activity of 47 nm Pd concave cubes and are shown in Figure 3.16. The catalyst with concave cubes of largest size was found to be marginally more active when compared to smaller ones. The onset temperature for 37 nm particles and 23 nm supported on MgO was 150 °C and 160 °C respectively. They showed 100% conversion at around 230 °C. This was contradictory to the usual scenario where activity decreases with increasing particle size. The activation energy for Pd concave cubes of 47 nm, 37 nm and 23 nm was 75 kJ/mol, 86 kJ/mol and 127 kJ/mol respectively taking CO conversion values below 15% for calculation. This better activity can be speculated to the better stability of our larger nanoparticles when compared to the smaller ones keeping the active centers intact under reaction environment.

d. Turn over frequency calculations

In order to investigate the intrinsic activity of the catalyst, the TOF values were calculated using total number of surface Pd atoms into account. The turn over frequency value calculated from different nanoparticle systems is compiled in table 3.3. Here, the TOF value of different catalyst system at a particular temperature (200 °C) was compared. The Pd concave cube (47 nm)/MgO showed a higher TOF value of 2.5 s^{-1} when compared to that of Pd concave cube (37 nm)/MgO and (23 nm)/MgO with values of 0.5 s^{-1} and 0.3 s^{-1} respectively (See Appendix for calculations). These results clearly showed that Pd concave cube (47 nm) was found to give a better performance even though the size was far above the optimum. The control experiments done with MgO supported Pd cubes and Pd spheres of similar size gave TOF@ 200 °C values of 0.024 s^{-1} and 0.065 s^{-1} which clearly depict the structure sensitivity of CO oxidation over Pd nanostructures. The TOF trends observed were similar on CeO_2 and TiO_2, except that for TiO_2 supported Pd concave nanocubes (47 nm) showed lower values which is due to the poor conversions achieved at 200 °C on this support. The Pd concave cube (47 nm) showed a relatively higher TOF value of 0.196 at 140 °C than that over 2 wt% Pd cubes (22 nm)/SiO_2 catalyst and 2 wt% Pd octahedrons (22 nm)/SiO_2 which gave a maximum TOF value of 0.52 s^{-1} and 0.69 s^{-1} respectively.[31]

No.	Catalyst	TOF value at T=200°C (s^{-1})			TOF max (s^{-1}) at 100% at T=T$_{100}$ conversion on MgO
		MgO	CeO$_2$	TiO$_2$	
1	Pd concave cube (47nm)	2.55	2.45	0.99	2.55 (200°C)
2	Pd concave cube (37nm)	0.5	0.4	0.5	2.13 (220°C)
3	Pd concave cube (23nm)	0.3	0.1	0.16	1.24 (240°C)
4	Pd spheres(~ 35nm)	0.06	-	0.02	-
5	Pd cubes (~30nm)	0.02	0.069	0.03	0.84 (270°C)
6	Pd spherical seeds (~6nm)	0.1	0.13	0.08	0.16 (220°C)

Table 3.2: The TOF values calculated for different supported nanoparticle systems at 200 °C and maximum TOF obtained at full conversion.

The TOF values obtained here gave an indication that the activity of Pd concave nanocubes with size above the optimum range have little dependence on the support that is being used and it is the structural defects on the nanoparticle that play a dominant role in CO adsorption and oxygen activation and thereby formation of CO_2. The Pd concave nanocube carrying large amount of under co-ordinated surface atoms can provide lower activation barrier for CO oxidation reaction compared to 6 nm or 35 nm spherical particles. This is interesting as it is contradictory to the usual scenario where activity increases on decreasing the particle size.[44]

Since catalysis is a surface phenomenon, the dependence of the turn over frequency on the exposed surface atoms was investigated. The surface atoms on concave cubes, cubes and spheres of similar size were calculated numerically by taking morphological factors into account (see Appendix for calculation). It can be inferred that even though the number of surface Pd atoms is more for 35 nm spherical particles when compared to a 37 nm Pd concave cube, the TOF is less relative to a concave cubes (See Figure 3.17). This enhanced activity can be related to the presence of under coordinated step atoms on a Pd concave cube which exposes {310} high index planes. The calculations on Pd nanoflowers were not taken into consideration due to the more corrugated structure. Both experimental and theoretical studies have shown that oxygen binds strongly to the defect sites

than on flat terraces of Pd surfaces.[53-55] It is also understood that the CO binding energy is also altered on such defect sites but not as significant compared to oxygen adsorption.[56-57] So improved activity could be attributed to the increased number of adsorption sites for O_2 activation in the form of steps and kinks which reacts with CO from the terrace surfaces.[58-59]
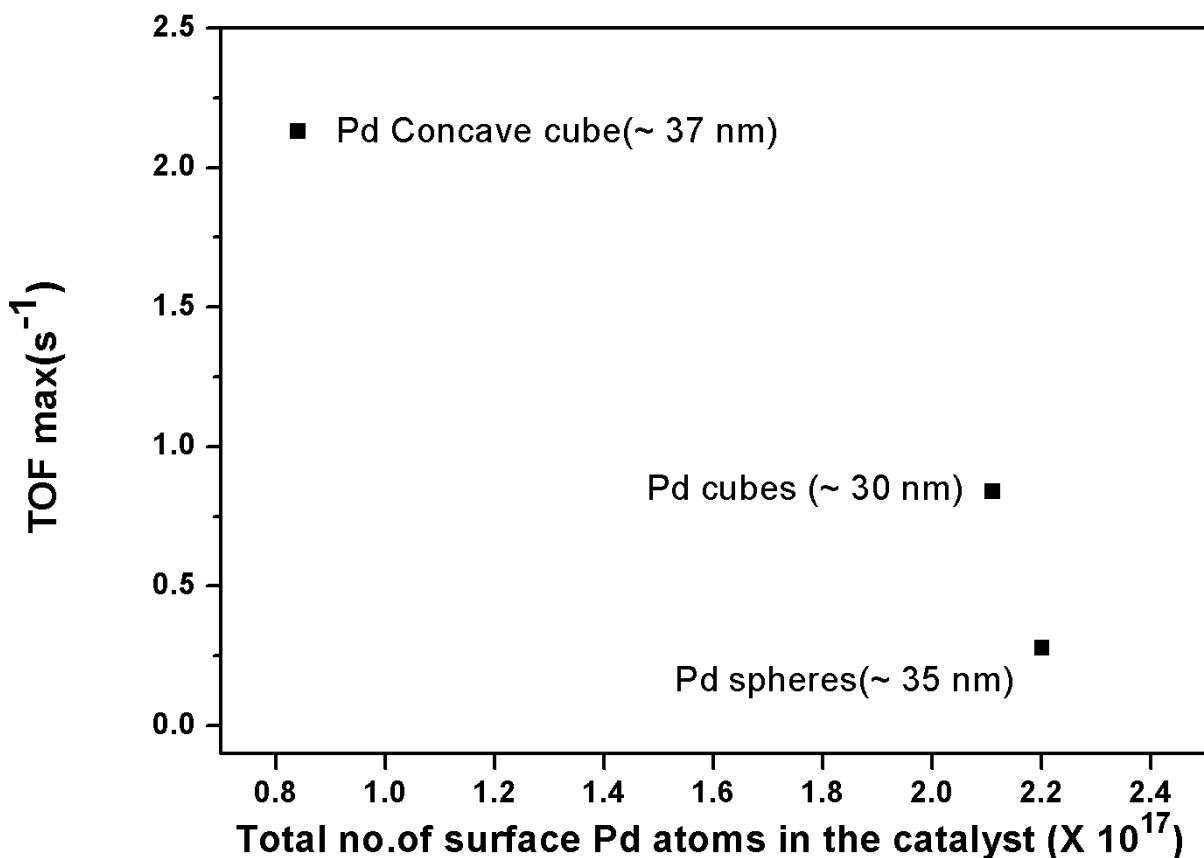
Figure 3.17: The plot of maximium TOF value for CO oxidation reaction against the total surface Pd atoms on concave cubes, cubes and spherical nanoparticles of similar size supported on MgO.

e. Catalyst stability

To find the extended stability of the nanostructures, the second cycle for the supported Pd catalysts was carried out, and the conversion plot is shown in Figure 3.18. Surprisingly, a similar activity was observed with remarkable stability for a supported Pd concave cube (47 nm) and Pd nanoflowers (100 nm). The lesser structural stability of the 23 nm particles is also evident from the shift in onset and full conversion temperature during the second cycle. The structural stability of Pd concave cubes (47 nm) and nanoflowers (100 nm) can be

attributed to the bigger size of the nanoparticles, which can resist morphological changes to a greater extent as demonstrated recently for nanoporous Au.[60]
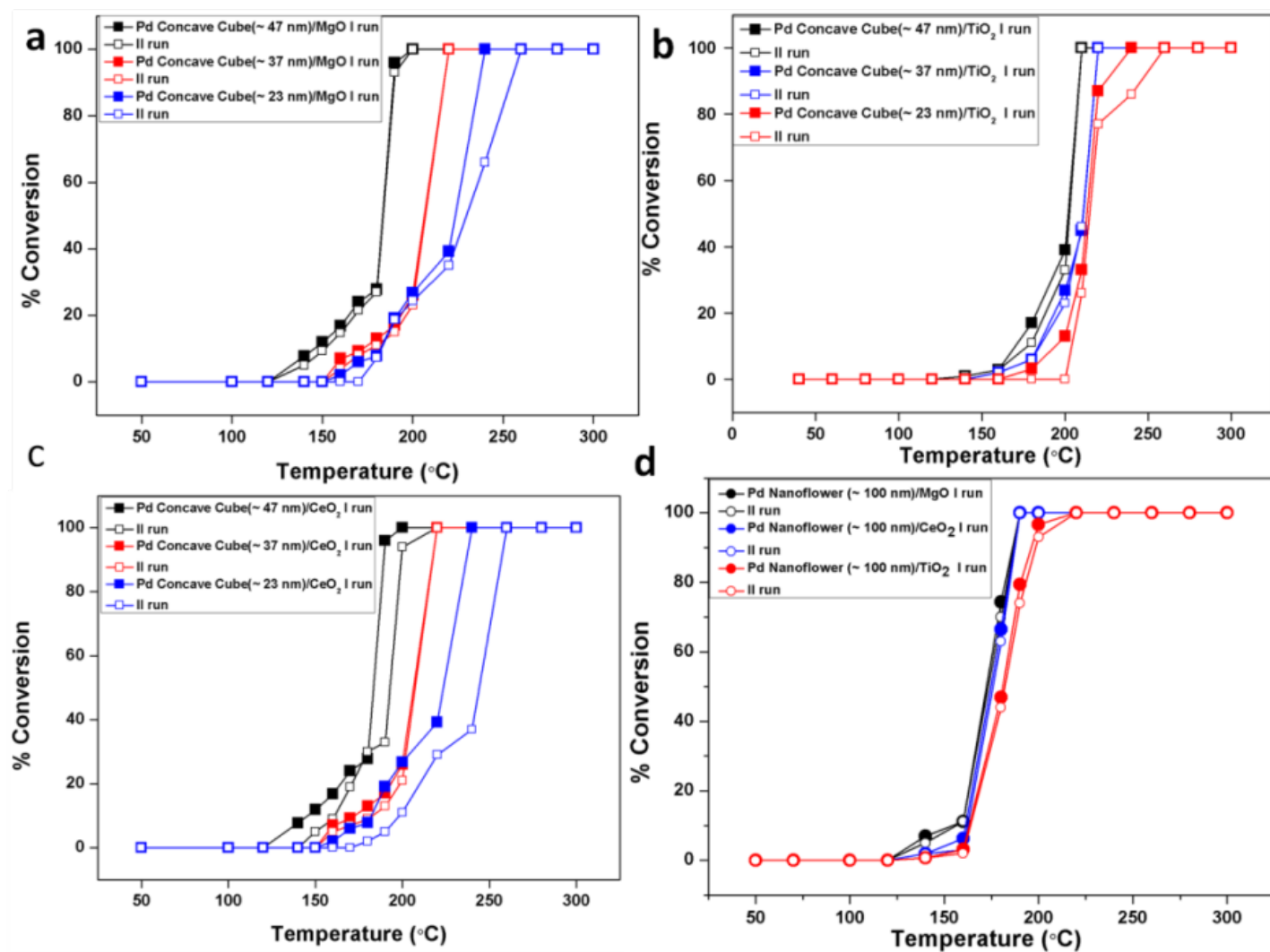
Figure 3.18: The CO conversion graph for the first and second run of the different supported Pd nanostructures. The catalysts were also found not to deactivate till 300 °C and showed a steady conversion (100%) for 5 h at 200 °C demonstrating that the active sites responsible for catalysis were intact even at those temperatures and in reactant stream except for supported 23 nm Pd concave nanocubes (See Figure 3.19). It is well documented that smaller particles are mobile on the support and can undergo structural changes under reactant stream and with temperature.[61-63]
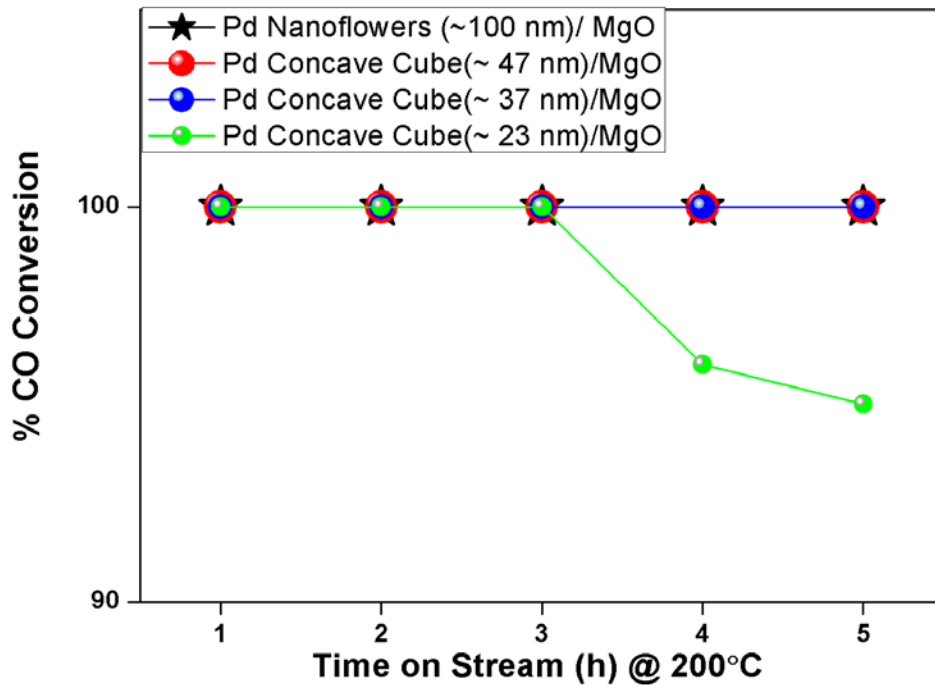
Figure 3.19: The time on stream versus % CO conversion plot for Pd Concave cubes of different sizes and Pd nanoflowers (~ 100 nm) supported on MgO.

f. Spent catalyst analysis
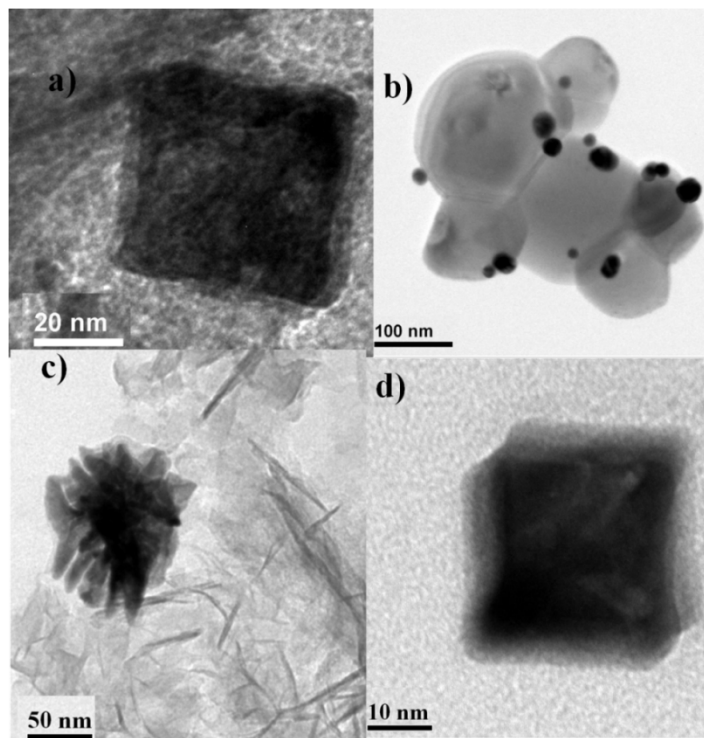
Figure 3.20: TEM images of the catalyst after two cycles of CO oxidation reaction. a) Pd concave cube (~ 47

nm) supported on MgO b) Pd Concave cube (~ 23 nm) supported on TiO_2 c) nanoflower supported on MgO d) unsupported nanoparticle (~ 37 nm) before reaction.

TEM analysis of the spent catalyst was done, and interestingly, Pd concave cubes with size 47 nm were found to maintain their morphology, but smaller particles with size 23 nm lost their morphology after two cycles as observed from Figure 3.20. The Pd nanoflowers (~ 100 nm) were also found to retain their morphology after three cycles of CO oxidation. This clearly shows the extended stability of larger nanoparticles when compared to smaller ones.

3.4. Conclusions

In summary concave Pd nanocubes and Pd nanoflowers were synthesized using a seed mediated protocol in aqueous solution at room temperature within 1 h reaction time. The synthesis method showed the systematic evolution of spherical Pd nanoparticles into Pd nanocubes and then to concave Pd nanocubes. By carefully choosing the surfactant from CTAC to CTAB Pd nanoflowers were obtained as the major product. Owing to the presence of a large amount of defects, these nanoparticles showed better catalytic activity towards Suzuki coupling and Heck coupling reactions than the Pd nanocubes. This clearly demonstrates the structure sensitivity of Pd nanoparticles for this reaction. The reactivity of different sized concave nanocubes showed similar conversion and turn over numbers showing the size insensitivity and demonstrating the strong dependence on surface defects.

The rate of CO oxidation was found to be more facile on supported high index faceted Pd concave nanocubes and nanoflowers which exposes {110} and {111} step sites than to a 6 nm particle. This was evidenced by lower onset temperature and temperature of full conversion shown by high index faceted particles. The effect of support was also probed by using different supports like MgO, CeO_2 and TiO_2. A marginal or no support effect was observed in this case. The better activity of larger concave cubes when compared to the smaller ones can be attributed to the better morphological stability of larger particles. This study is probably the first attempt on investigating the trends in reactivity of structured high index faceted Pd nanoparticle systems for gas phase

reactions. The importance of morphology controlled synthesis of nanoparticles with high index facets is reiterated by the results reported in this work.

3.5. References

(1)   Zeng, X. Q.; Latimer, M. L.; Xiao, Z. L.; Panuganti, S.; Welp, U.; Kwok, W. K.; Xu, T.*Nano Lett,* **2010**, *11*, 262.

(2)   Lim, B.; Jiang, M.; Camargo, P. H. C.; Cho, E. C.; Tao, J.; Lu, X.; Zhu, Y.; Xia, Y. *Science,* **2009**, *324*, 1302.

(3)   Sawai, K.; Tatumi, R.; Nakahodo, T.; Fujihara, H. *Angew Chem,* **2008**, *120*, 7023.

(4)   Haruta, M.; Tsubota, S.; Kobayashi, T.; Kageyama, H.; Genet, M. J.; Delmon, B. *J Catal,* **1993**, *144*, 175.

(5)   Mostafa, S.; Behafarid, F.; Croy, J. R.; Ono, L. K.; Li, L.; Yang, J. C.; Frenkel, A. I.; Cuenya, B. R. *J Am Chem Soc,* **2010**, *132*, 15714.

(6)   Schubert, M. M.; Hackenberg, S.; van Veen, A. C.; Muhler, M.; Plzak, V.; Behm, R. J. *J Catal,* **2001**, *197*, 113.

(7)   Bowker, M.; Stone, P.; Morrall, P.; Smith, R.; Bennett, R.; Perkins, N.; Kvon, R.; Pang, C.; Fourre, E.; Hall, M. *J Catal,* **2005**, *234*, 172.

(8)   Comotti, M.; Li, W.-C.; Spliethoff, B.; Schüth, F. *J. Am. Chem.Soc,* **2005**,*128*, 917.

(9)   Taylor., H. S. *Proc. R.Soc. of Lond Ser A*, **1925**, *108*, 105.

(10)   Vilé, G.; Baudouin, D.; Remediakis, I. N.; Copéret, C.; López, N.; Pérez-Ramírez, J. *ChemCatChem,* **2013**, *5*, 3750.

(11)   Hellman, A.; Baerends, E. J.; Biczysko, M.; Bligaard, T.; Christensen, C. H.; Clary, D. C.; Dahl, S.; van Harrevelt, R.; Honkala, K.; Jonsson, H.; Kroes, G. J.; Luppi, M.; Manthe, U.; Nørskov, J. K.; Olsen, R. A.; Rossmeisl, J.; Skúlason, E.;Tautermann, C. S.; Varandas, A. J. C.; Vincent, J. K., *J Phys Chem B,* **2006**, *110*, 17719.

(12)   García-García, F. R.; Guerrero-Ruiz, A.; Rodríguez-Ramos, I. *Top Catal,* **2009**, *52*, 758.

(13)   Zhou, Z.-Y.; Huang, Z.-Z.; Chen, D.-J.; Wang, Q.; Tian, N.; Sun, S.-G. *Angew Chem Int Ed,* **2010**, *49*, 411.

(14)   Jin, M.; Zhang, H.; Xie, Z.; Xia, Y. *Angew Chem Int Ed,* **2011**, *50*, 7850.

(15)   Tian, N.; Zhou, Z. Y.; Yu, N. F.; Wang, L. Y.; Sun, S. G. *J Am Chem Soc,***2010**, *132*, 7580.

(16)   Tian, N.; Zhou, Z.-Y.; Sun, S.-G. *Chem Commun,* **2009**, *0*, 1502.

(17)   Wang, F.; Li, C. H.; Sun, L. D.; Wu, H. S.; Ming, T. A.; Wang, J. F.; Yu, J. C.; Yan, C. H. *J Am Chem Soc,* **2011**, *133*, 1106.

(18)   Huang, X.; Tang, S.; Zhang, H.; Zhou, Z.; Zheng, N. *J Am Chem Soc,* **2009**,*131*, 13916.

(19)   Zhang, J.; Zhang, L.; Xie, S.; Kuang, Q.; Han, X.; Xie, Z.; Zheng, L. *Chem.Euro J,* **2011**, *17*, 9915.

(20)   Shao, Z.; Zhu, W.; Wang, H.; Yang, Q.; Yang, S.; Liu, X.; Wang, G. *J Phys Chem C,* **2013**, *117*, 14289.

(21)   Meng, H.; Sun, S.; Masse, J.-P.; Dodelet, J.-P. *Chem.Mater,* **2008**, *20*, 6998.

(22)   Mohanty, A.; Garg, N.; Jin, R. C. *Angew Chem Int Ed,* **2010**, *49*, 4962.

(23)   Oh, S.-H.; Hoflund, G. B. *J Phys Chem A,* **2006**, *110*, 7609.

(24)   Zhou, Y.; Wang, Z.; Liu, C. *Catal Sci & Technol,* **2015**, *5*, 69.

(25)   Glaspell, G.; Fuoco, L.; El-Shall, M. S. *J. Phys Chem B,* **2005**, *109*, 17350.

(26)   Hendriksen, B. L. M.; Ackermann, M. D.; van Rijn, R.; Stoltz, D.; Popa, I.; Balmes, O.; Resta, A.; Wermeille, D.; Felici, R.; Ferrer, S.; Frenken, J. W. M. *Nat Chem,* **2010**, *2*, 730.

(27)   Hendriksen, B. L. M.; Bobaru, S. C.; Frenken, J. W. M. *Surf Sci,* **2004**, *552*, 229.

(28)   Hendriksen, B. L. M.; Bobaru, S. C.; Frenken, J. W. M. *Catal Today*, **2005**, *105*, 234.

(29)   Hendriksen, B. L. M.; Frenken, J. W. M. *Phys Rev Lett,* **2002**, *89*, 046101.

(30)   Jin, M.; Liu, H.; Zhang, H.; Xie, Z.; Liu, J.; Xia, Y. *Nano Res,* **2011**, *4*, 83.

(31)   Wang, R.; He, H.; Liu, L.-C.; Dai, H.-X.; Zhao, Z. *Catal Science & Technol,* **2012**, *2*, 575.

(32)   Uetsuka, H.; Watanabe, K.; Kimpara, H.; Kunimori, K. *Langmuir,* **1999**, *15*, 5795.

(33)   Schauermann, S.; Freund, H.-J. *Acc Chem Res,* **2015,** *48,* 2775.

(34)   Tian, N.; Zhou, Z.-Y.; Sun, S.-G.; Ding, Y.; Wang, Z. L. *Science,* **2007**, *316*, 732.

(35)   Tian, N.; Zhou, Z.-Y.; Sun, S.-G. *J Phys Chem C ,* **2008**, *112*, 19801.

(36)   Watt, J.; Cheong, S.; Toney, M. F.; Ingham, B.; Cookson, J.; Bishop, P. T.; Tilley, R. D. *ACS Nano,* **2010**, *4*, 396.

(37)   Lim, B.; Jiang, M. J.; Tao, J.; Camargo, P. H. C.; Zhu, Y. M.; Xia, Y. N. *Adv Funct Mater,* **2009**, *19*, 189.

(38)   Millstone, J. E.; Wei, W.; Jones, M. R.; Yoo, H.; Mirkin, C. A. *Nano Lett,* **2008**, *8*, 2526.

(39)   Yu, Y.; Zhang, Q.; Lu, X.; Lee, J. Y. *J Phys Chem C*, **2010**, *114*, 11119.

(40)   Zhang, H.; Jin, M.; Xia, Y. *Angew Chem Int Ed,* **2012**, *51*, 7656.

(41)   Chernov.A *Sov.Phys.Cryst*, **1972**, *16*, 734.

(42)   Zhang, W.; Wang, Q.; Qin, F.; Zhou, H. M.; Lu, Z.; Chen, R. *J Nanosci Nanotech,* **2011**, *11*, 7794.

(43)   Le Bars, J.; Specht, U.; Bradley, J. S.; Blackmond, D. G. *Langmuir,* **1999**, *15*, 7621.

(44)   Vinod, C. P. *Catal Today*, **2010**, *154*, 113.

(45)   Mavrikakis, M.; Stoltze, P.; Nørskov, J. K. *Catal Lett,* **2000**, *64*, 101.

(46)   Liang, Q.; Liu, J.; Wei, Y.; Zhao, Z.; MacLachlan, M. J. *Chem Commun,* **2013**, *49*, 8928.

(47)   Liu, X.; Wang, R.; Song, L.; He, H.; Zhang, G.; Zi, X.; Qiu, W. *Catal Commun,* **2014**, *46*, 213.

(48)   Wang, H.; Liu, C.-j. *Appl Catal B,* **2011**, *106*, 672.

(49)   Ivanova, A. S.; Slavinskaya, E. M.; Gulyaev, R. V.; Zaikovskii, V. I.; Stonkus, O. A.; Danilova,
        I. G.; Plyasova, L. M.; Polukhina, I. A.; Boronin, A. I. *Appl Catal B,* **2010**, *97*, 57.

(50)   Wang, Z.; Li, B.; Chen, M.; Weng, W.; Wan, H. *Sci. China Chem,* **2010**, *53*, 2047.

(51)   Liu, L.; Zhou, F.; Wang, L.; Qi, X.; Shi, F.; Deng, Y. *J Catal,* **2010**, *274*, 1.

(52)   Hinokuma, S.; Fujii, H.; Okamoto, M.; Ikeue, K.; Machida, M. *Chem Mater,* **2010**, *22*, 6183.

(53)   Vogel, D.; Spiel, C.; Schmid, M.; Stöger-Pollach, M.; Schlögl, R.; Suchorski, Y.; Rupprechter,
        G. *J. Phys Chem C,* **2013**, *117*, 12054.

(54)   Zhang, Y.; Rogal, J.; Reuter, K. *Phys Rev B,* **2006**, *74*, 125414.

(55)   Westerström, R.; Gustafson, J.; Resta, A.; Mikkelsen, A.; Andersen, J. N.; Lundgren, E.; Seriani,
        N.; Mittendorfer, F.; Schmid, M.; Klikovits, J.; Varga, P.; Ackermann, M. D.; Frenken, J. W. M.;
        Kasper, N.; Stierle, A. *Phys Rev B,* **2007**, *76*, 155410.

(56)   Yudanov, I. V.; Sahnoun, R.; Neyman, K. M.; Rösch, N.; Hoffmann, J.; Schauermann, S.;
        Johánek, V.; Unterhalt, H.; Rupprechter, G.; Libuda, J.; Freund, H.-J. *J. Phys Chem B,* **2003**, *107*,
        255.

(57)   Ramsier, R. D.; Lee, K. W.; Yates Jr, J. T. *Surf Sci,* **1995**, *322*, 243.

(58)   Xu, J.; Jr., J. T. Y. *J Chem.Phys,* **1993**, *99*, 725.

(59)   Watanabe, K.; Ohnuma, H.; Kimpara, H.; Uetsuka, H.; Kunimori, K. *Surf Sci,* **1998**, *402*, 100.

(60)   Biener, M. M.; Biener, J.; Wichmann, A.; Wittstock, A.; Baumann, T. F.; Bäumer, M.; Hamza,
        A. V. *Nano Lett,* **2011**, *11*, 3085.

(61)   Cabié, M.; Giorgio, S.; Henry, C. R.; Axet, M. R.; Philippot, K.; Chaudret, B. *J. Phys Chem C,*
        2010, *114*, 2160.

(62)   Hansen, T. W.; DeLaRiva, A. T.; Challa, S. R.; Datye, A. K. *Acc Chem Res,* **2013**, *46*, 1720.

(63)   Newton, M. A.; Belver-Coldeira, C.; Martinez-Arias, A.; Fernandez-Garcia, M. *Nat Mater,* **2007**,
        6, 528.

Chapter-4

Synthesis of Ruthenium nanostructures and its CO oxidation activity[#]

4.1. Introduction

The area of nanoparticle assemblies and its application have gained much interest during recent past as they can bridge the gap between nanometer scale and macro size regime.[1-3] The synthesis strategies for the formation of self assembled nanoparticles in the form of nanochains and structured nanoparticles has been developed for face centered cubic (fcc) metals like Ag,[4] Au,[5] Pd,[6] Ir,[7] Rh[8] etc but are less established for hexagonally close packed (hcp) metals. The inherent anisotropy along the C-axis in hcp systems makes it tedious to synthesise structured nanoparticles of the same. Generally, hcp metals they tend to grow in the form of nanorods or nanoworm like structures to minimise surface energies.[9]

Ruthenium nanoparticles find potential application in hydrogenation as well as for the oxidation or preferential oxidation (PROX) of CO when used in conjunction with fuel cell applications. Since PROX reactor should perform between low temperature shift reactor (~ 200 °C) and polymer–electrolyte membrane fuel cell (PEMFC) (~ 80 °C) there is lot of interest in CO oxidation studies on Ru based structures.[10-12] Morphology controlled synthesis of Ruthenium nanoparticles have been achieved recently. A report by Tilley et al demonstrated the thermodynamic formation of hour glass ruthenium nanocrystals which were found to readily self assemble to form a super lattice structure.[13] The crucial role of morphology in defining catalysis has been recently demonstrated by Yan and co-workers where Ru with capped column morphology synthesized by a hydrothermal approach was found to show enhanced SERS activity when compared to nano triangles and spheres.[14] Yang et al reported a systematic study on the synthesis of ruthenium nanoparticles in oleylamine at well above 300 °C, where the morphology was tuned by temperature or by employing Au or Ag as seeds.[15] Chain like Ruthenium arrays with ~ 280 nm length have been synthesized by reducing the complex of Ru ions with poly vinyl pyrrolidone (PVP) at 1 MPa H_2 and 353 K in aqueous media and were found to hydrogenate phenol in aqueous media.[16] The synthesis strategies developed till now for Ru nanoparticles are energy intensive (in the form of temperature or pressure) and the morphology control at ambient or near ambient conditions still remains a challenge. Here, in this chapter, a seed mediated synthesis strategy for the formation of Ruthenium nanochains at mild temperatures (70 °C) and in aqueous medium is reported and their CO

oxidation activity demonstrated and compared to Ru spheres of ~ 6 nm and ~ 3.5 nm size.

4.2. Experimental

4.2.1. Reagents

Ruthenium nitrosyl nitrate $Ru(NO)(NO)_3$ 1.5 wt% w/V, Ruthenium chloride, Ruthenium acetyl acetonate (Sigma Aldrich), Poly vinyl pyrrolidone, 1-4 butanediol, Cetyl trimethyl ammonium bromide (CTAB), Ascorbic acid (AA), Sodium Borohydride (Spectrochem) were purchased and used as received. The water used in all the experiments was ultrapure millipore water.

4.2.2. Synthesis of Ruthenium nanochains

Ruthenium nanochains were synthesised by a seed mediated procedure. In brief, for the formation of Ru nanoseeds, 125 µL of 1.5 wt% w/V $Ru(NO)(NO)_3$ solution was added to a beaker followed by 50 µL freshly prepared ice cold 0.25 M sodium borohydride ($NaBH_4$) solution. The solution turned black on adding $NaBH_4$ solution. For the preparation of nanochains, a solution containing 4 mL of 22 mM CTAB, 300 µL of 0.1 M Ascorbic acid (AA) and 50 µL of 1.5 wt% w/V $Ru(NO)(NO)_3$ solution was made and kept at 70 °C. The seed solution was completely added to the above solution and kept for 30 minutes under magnetic stirring. The black colloidal solution formed was then left undisturbed at room temperature for 12 h.

4.2.3. Synthesis of supported Ruthenium nanochains

The supported catalysts were prepared by sol-immobilization (SI method) method by scaling up the synthesis to obtain 5 mg of Ru metal in the final colloidal solution. The colloidal solution was centrifuged at 12000 rpm for 15 minutes and washed thoroughly with water. In brief, the residue containing approximately 5 mg of Ru metal was made up to 3 mL with Millipore water and desired amount (170 mg) of support was added so as to obtain 3 wt% catalysts. The slurry obtained was stirred for 2 h and dried to remove water and calcined at 300 °C for 5 h.

4.2.4. Synthesis of Ruthenium nanospheres (~ 6 nm)

Ru nanoparticles (~ 6 nm) were synthesised by a reported polyol procedure as described by Somorjai and co-workers.[12] In a typical synthesis of 6 nm Ru NPs, 10 mM $Ru(acac)_3$ and PVP (in terms of repeating unit) at a

fixed Ru / PVP ratio of 1:10 were added to 20 mL of ethylene glycol (EG) in a 50 mL three-necked flask at room temperature. The stock solution was heated to 80 °C at this temperature for 20 min to remove water and oxygen under magnetic stirring. The solution was then heated to 180 °C and maintained at this temperature for 2 h under Ar. When the reaction was complete, an excess of acetone was poured into the solution at room temperature to form a cloudy black suspension. This suspension was separated by centrifugation at 4200 rpm for 6 min, and the black product was collected by discarding the colorless supernatant. The precipitated Ru NPs were washed with acetone once, and were redispersed in ethanol.

4.2.5. Synthesis of Ru (2.8 nm) impregnated catalyst

In a typical synthesis as adopted,[17] the appropriate amounts of $RuCl_3 \cdot 3H_2O$ were dissolved in deionized water and appropriate amount of support added. The resultant slurry was aged at room temperature for 24 h and stirred at regular intervals to retain uniformity. After evaporation at 373 K in water bath and drying at 378 K for 12 h, the samples were calcined at 673 K for 4 h. The catalyst was designated as Ru (2.8 nm) Imp.

4.2.6. Characterisation

Characterization of the catalysts was done by

X-ray Diffraction Analysis: Powder X-ray diffraction (XRD) was measured on a PANalytical X'pert Pro dual goniometer diffractometer working under 40 kV and 30 mA. The Cu Kα (1.5418Å) radiati on was used with a Ni filter.

UV-Visible Spectroscopy: Varian Cary 50 Conc UV–Vis spectrophotometer with a dual beam source was used for the UV-Visible analysis.

Transmission Electron Microscopy (TEM): TEM images were recorded by FEI Tecnai TF-30 and TF-20 electron microscope, operating at 300 keV and 200 keV.

The Inductively coupled Plasmon analysis was done using Spectro Arcos ICP-OES.

The Dynamic Light Scattering experiments and zeta potential measurements were done with Brookhaven Instruments Corporation-90 plus Nanoparticle size analyser equipped with a 632.8 nm laser source.

4.2.7. Catalyst activity testing: CO oxidation

The catalytic activity of supported Ru nanostructures for CO oxidation was measured in a fixed bed reactor under atmospheric pressure using 100 mg pelletized catalyst. The total flow rate was 50 ml/min with a ratio of (1:5:19 CO: O_2: N_2) with a temperature range of 40 °C to 300 °C. The calculated GHSV was 30000 $cm^3/g_{cat}/h$. The reactor was placed in a tubular furnace and temperature of the furnace was controlled by Radix 6400 temperature controller. The catalyst bed temperature was measured by a K-type thermocouple. The effluent gases were analysed online by gas chromatograph equipped with online gas sampling valve and a TCD detector. The activity was examined by looking at the CO conversion.

4.3. Results and Discussion

4.3.1. Transmission electron microscopy

a. Ruthenium seeds and nanochains
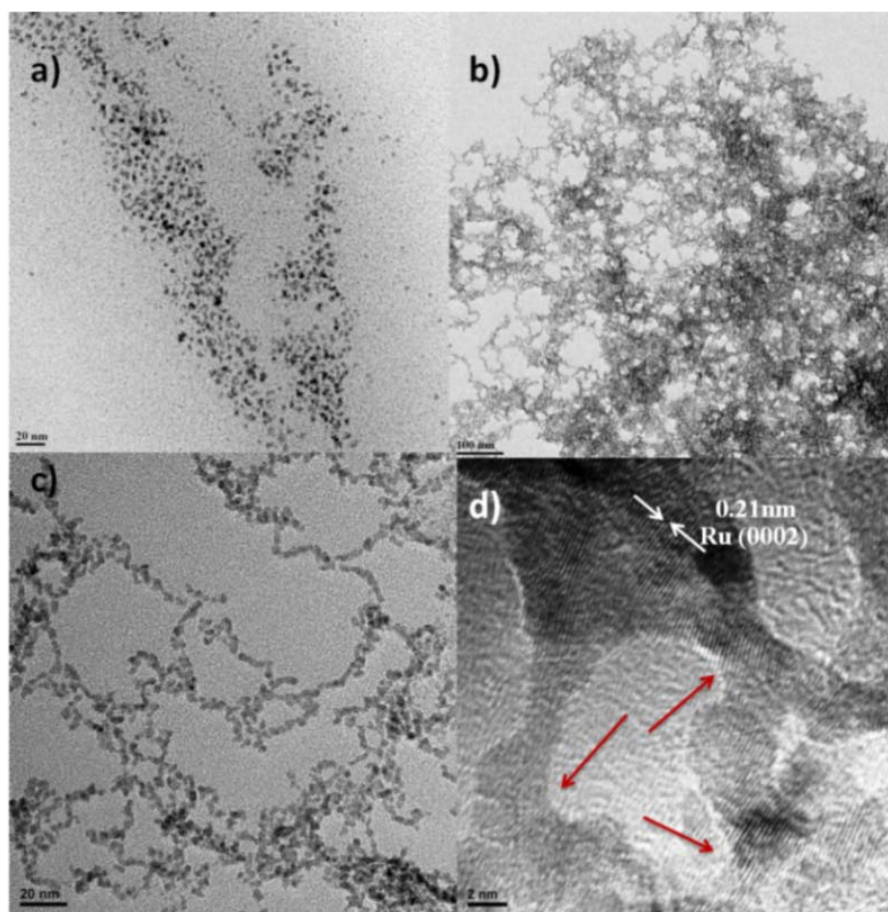
Figure 4.1: TEM image showing a) Ru seeds of approximately 3.5 nm b) interconnected Ru nanoparticles forming chains c) a magnified image and d) HRTEM image showing the lattice fringe with d value 0.21 nm

where grooves are marked using arrows.

The TEM images of the as synthesised Ru seeds and Ru nanochains are shown in Figure.4.1. The as synthesised Ruthenium seeds of size ~ 3.5 nm are shown in Figure 4.1a. In Figure 4.1b (low) and Figure 4.1c (high) Ru nanochains at different magnifications is shown. It can be inferred that the small nanoparticles aggregates to form interconnected networks whose length varies from few tens of nanometer to micron scale. The high resolution TEM image shows a d spacing value of 0.21 nm which corresponds to the Ru (0002) lattice. The presence of grooves which is marked by the arrows is shown in the Figure 4.1d. The continuity of the formed nanochains and the presence of under coordinated edges are also clear from the high resolution TEM image showed in Figure 4.2.
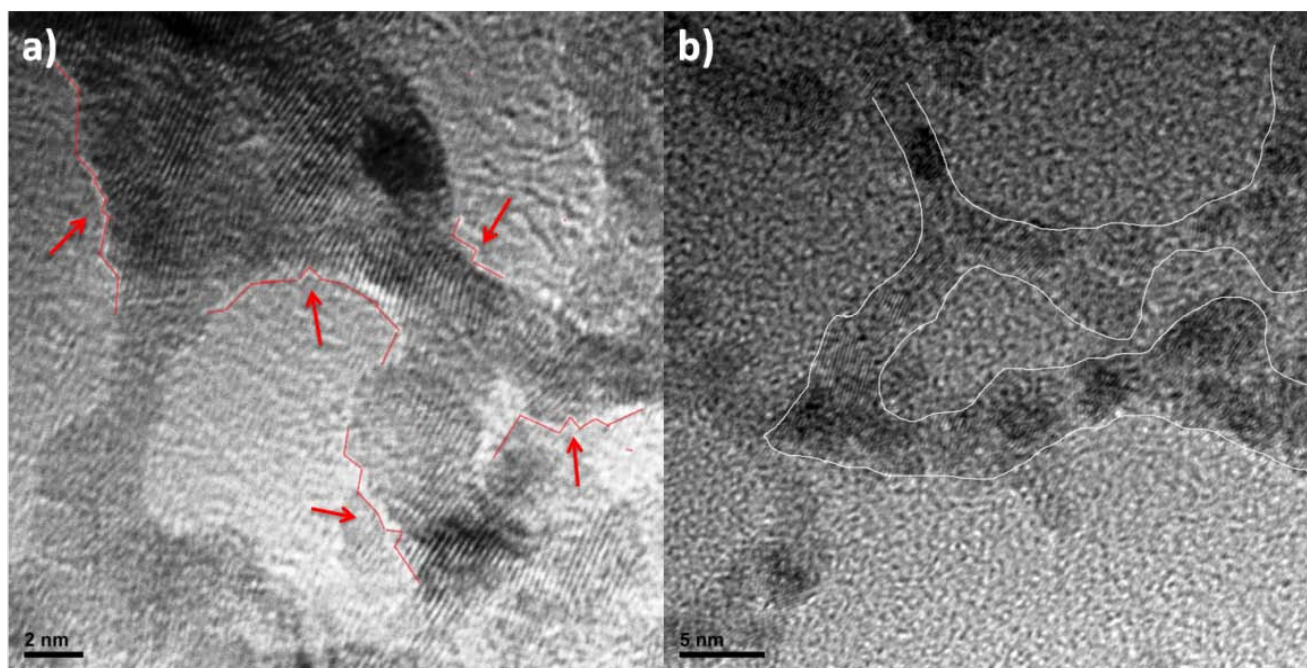
Figure 4.2: TEM image showing the under co-ordinated edges and the continuity of the Ru nanochains that are formed.

4.3.2. X-ray Diffraction and UV-Visible spectroscopy

Characteristic diffraction peaks from Ru nanochains gave major reflections of hcp at Ru (0002) and (1010) which implies that the growth orientation is along these two axes {JCPDS 06-0663}. The seed did not show any diffraction peaks this can be due to the small size of the nanoparticles as shown in Figure 4.3a. The UV-Visible

spectrum in Figure 4.3b shows that these nanostructures were SPR inactive.
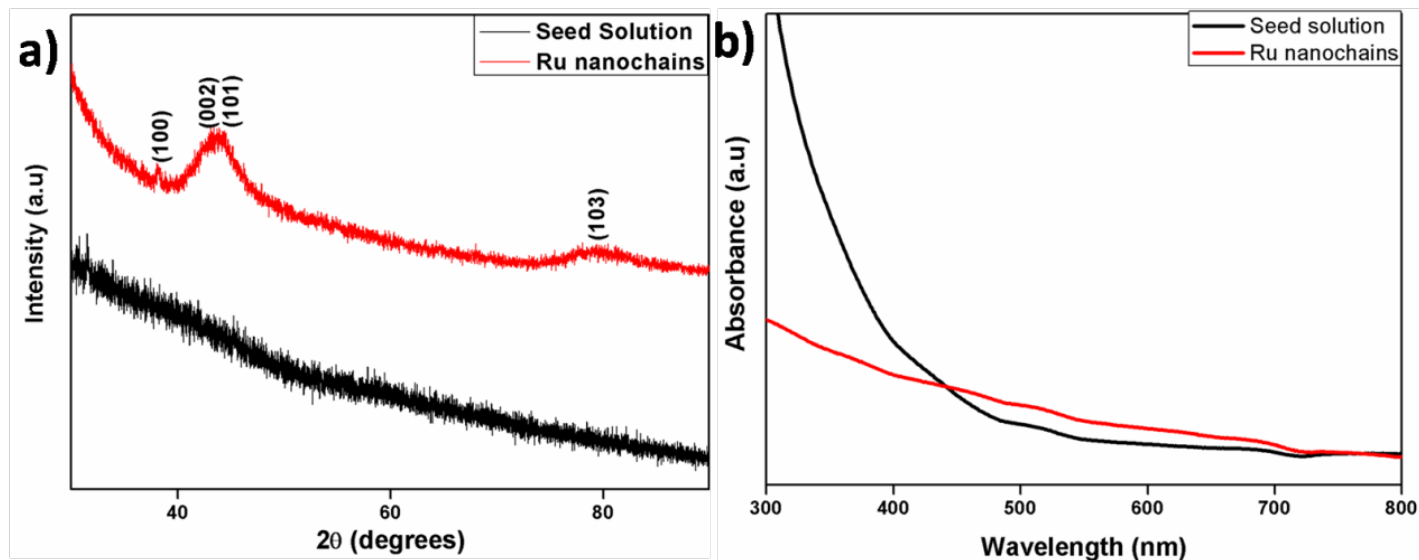
Figure 4.3: a) The XRD reflections of as synthesised Ru nanoseeds (~ 3.5 nm) and hcp Ru nanochains and b) The UV-Visible spectrum of Ru seed solution and Ru nanochains.

4.3.3. Dynamic Light scattering

The mechanism of the growth of nanoparticles to nanochains was studied using Dynamic Light Scattering (DLS) experiments. The mean diameter of the particle in the growth solution on the addition of seed varied from 68 nm (0 minutes) to 454 nm (2.5 h) indicating that the spontaneous formation of nanochains commenced as soon as the seed solution was added to growth solution as shown in table 4.1 which shows the mean diameter value measured at different time intervals. The stability of nanoparticle in solution is decided by the net charge on the nanoparticle surface.[18] The general rule for electrostatic stability is that the zeta potential should not be less than 30 mV. The mean Zeta potential value obtained for the nanochains was 76 mV which shows the electrostatic stability of the system. A positive zeta potential value also indicates positive charge on the nanoparticle surface and can be attributed to the binding of CTA+ ion on Ru nanoparticle surface.[15] The DLS particle size measurements correlates well with that reported by Sampath and co-workers for the formation of Ir and Os nanochains where a sudden increase in hydrodynamic size of the particles was attributed to the formation of such structures.[7,19]

Time (minutes)	Mean Diameter (nm)
0	68
30	102
60	127
90	253
120	262
150	454

Table 4.1: The table shows the variation of mean diameter of Ru nanochains with time as obtained from DLS experiments.

4.3.4. Inductively coupled Plasma

The amount of metal loading was estimated using ICP analysis. The loading of metal in all the catalysts were ~ 3 wt%.

4.3.5. Growth Mechanism of Ruthenium nanochains

In the present study, a seed mediated approach where small Ru seeds serve as the precursor for the synthesis of Ru nanochains is reported. The first step in this synthesis is the formation of small Ruthenium nanoparticles formed by the $NaBH_4$ reduction of Ru^{3+} ions which serves as the seed. These seeds are then added to the growth solution which contains surfactant and a weak reducing agent. The nanoparticles aggregate to form long nanochains which show defective sites in the form of grooves or furrows which can act as active centres for catalysis. Surfactant induced self assembly of nanoparticles to nanochains has been already reported.[20-22] The hydrophobic interaction and the steric hindrance between the added surfactant may play a role for the aggregation of nanoparticles to form chains.[3,8,23] If there is a non-uniform distribution of surfactants on the

nanoparticle surface a linear aggregate could be formed due to hydrophobic interactions of the CTAB. This was further confirmed by a control experiment where without surfactant in the growth solution showed immediate agglomeration and settling down of the particles. The schematic representation for the plausible mechanism of formation of nanochains from Ru nanoseed is shown in Scheme 4.1.
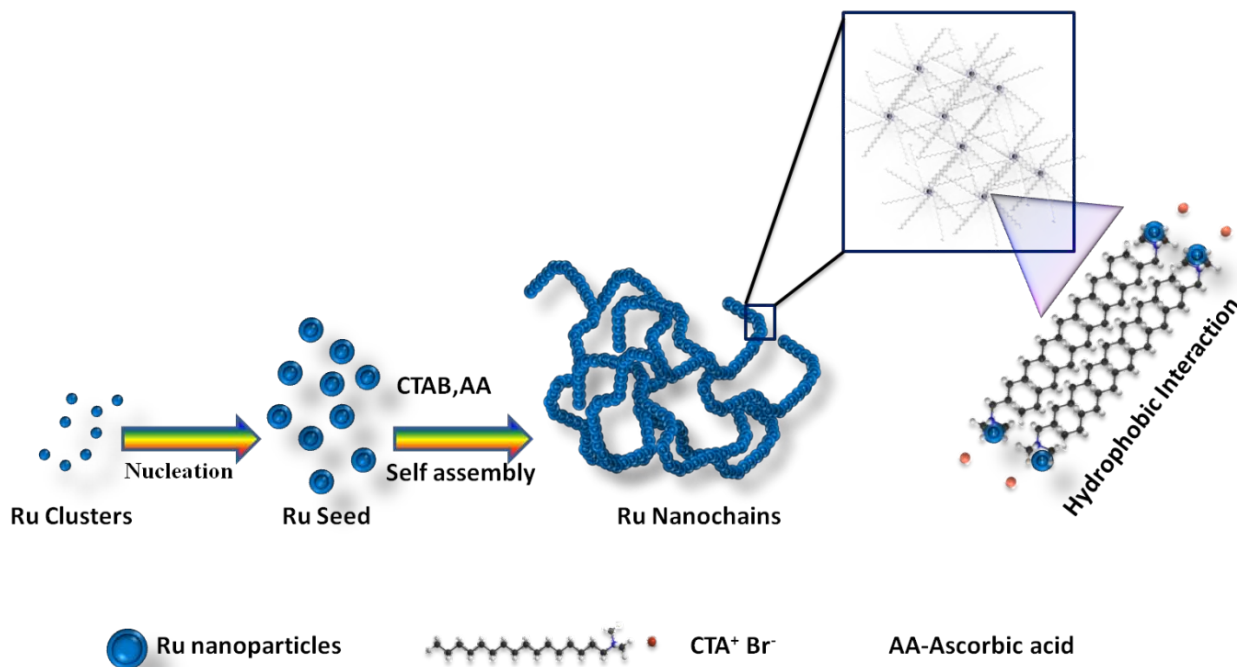
Scheme.4.1: The schematic representation for the formation of Ru nanochains from Ru nanoseeds

4.3.6. Catalytic activity testing: CO oxidation

The performance of these nanochains as a catalyst for CO oxidation was investigated by supporting them on ceria, titania and silica by sol-immobilisation (SI) method. These supports were chosen as the first two are reducible supports which show strong metal support interactions (SMSI) while the third one is considered as an inert support.[24] To compare the activity of Ru nanochains, the reactivity of Ru nanoseeds of approximately 3.5 nm used for making nanochains and ruthenium nanospheres of approximately 6 nm prepared by a reported procedure was also tested.[12] To test the role of the catalyst preparation method, Ru (2.8 nm) particle supported on ceria was synthesised by wet impregnation method by utilizing a reported procedure and the reactivity was compared with the rest of the catalysts.[25] Before the reaction the supported catalysts were calcined at 300 °C for 5 h as a pre-treatment step to remove any surfactants which can hamper the activity. The metal loadings were

approximately 3 wt% in all the catalysts as confirmed by Inductively Coupled Plasma (ICP) analysis.
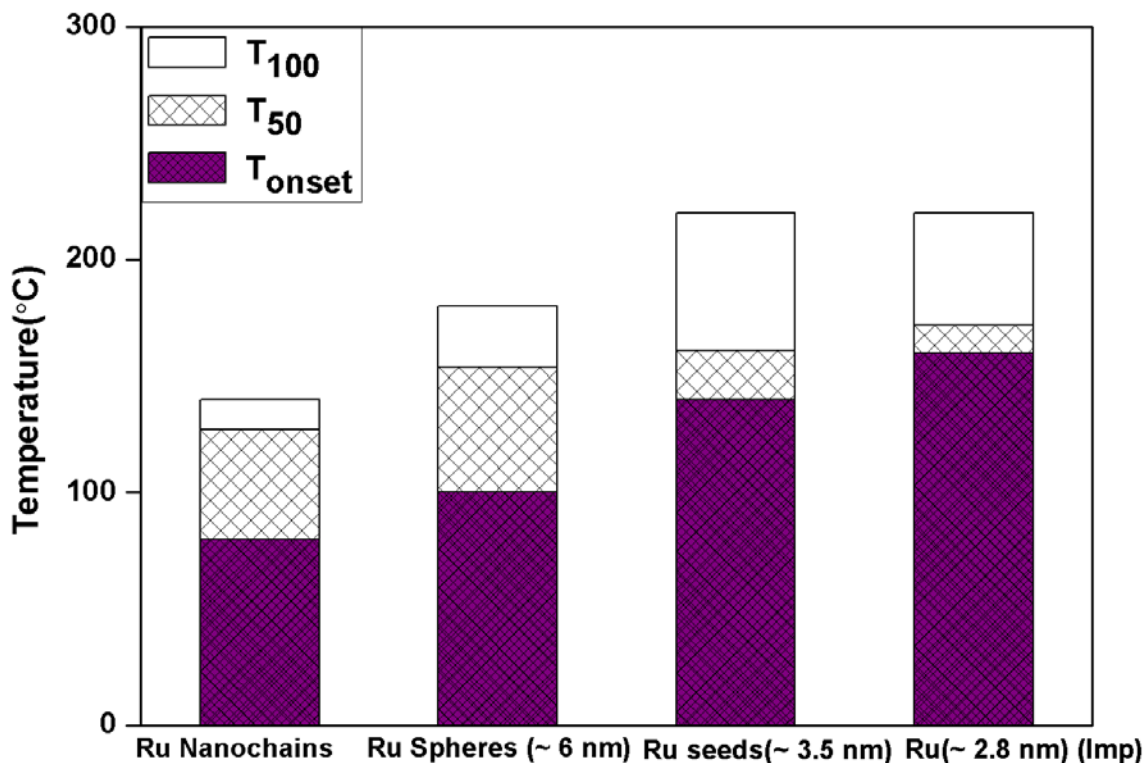
Figure 4.4: The CO oxidation activity profile for different Ru nanostructures supported on ceria by sol immobilisation method. Ru (2.8 nm) (Imp) denote the impregnated catalyst. T_{50} and T_{100} represent temperature for 50% conversion and full conversion respectively. The metal loading is approximately 3 wt% in all the catalysts.

The catalytic activity for the Ru nanostructures on ceria is summarized in Figure 4.4. It is evident that, Ru nanochains are the most active with an onset temperature of 80 °C giving full conversion (T_{100}) at 140 °C with a temperature for 50% conversion (T_{50}) value of 127 °C. The CO oxidation on Ru nanoparticles is reported to show size and crystal lattice dependency.[12,26] Also, previous literature shows that 6 nm Ru particles on silica exhibit better catalytic activity for CO oxidation compared to smaller particles which are prone to bulk oxidation faster.[27] The results shown in Figure 4.4 where Ru (6 nm) spheres supported on ceria being catalytically more active than Ru seeds of 3.5 nm supports the findings in literature. The performance of the nanochain were also compared with the conventional Ru (2.8 nm) impregnated on ceria system. Here also, the trends were as expected with smaller Ru (2.8 nm) (Imp) catalysts being marginally less active than sol

immobilised Ru seeds (~ 3.5 nm) catalyst but their onset, T_{50} and T_{100} being well above 6 nm Ru spheres. Overall the catalytic performances of these three nanoparticle systems were far below than that of Ru nanochains.
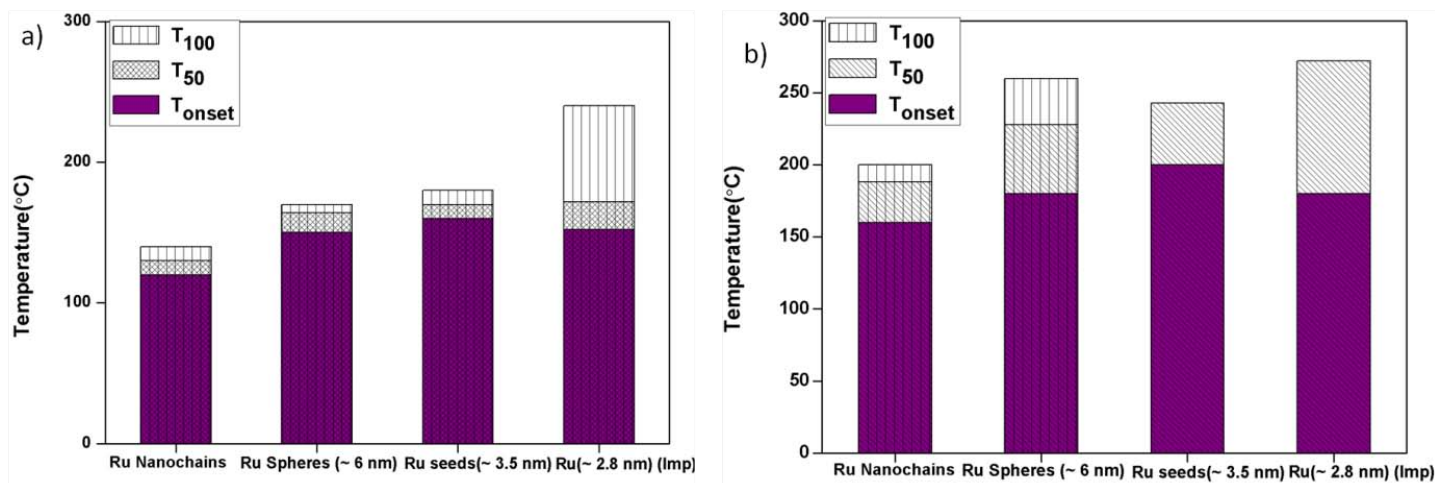
Figure 4.5: The CO oxidation activity profile for the Ru nanostructures supported on different supports a) TiO_2 b) SiO_2

To validate these important findings, the four sets of nanoparticles were supported on TiO_2 and SiO_2 and results gave similar trend like that on CeO_2 with Ru nanochains being the most active among the four as shown in Figure 4.5. Among the supports the activity trend follow based on easily reducible nature of the oxides i.e. CeO_2 > TiO_2 > SiO_2. It is important to note that Ru (3.5 nm) seeds and Ru (2.8 nm) (Imp) particles supported on SiO_2 did not reach full conversion even at 300 °C (80% conversion) whereas Ru nanochains on SiO_2 showed full conversion at ~ 200 °C. Thus ruthenium nanochains offer a distinctly different and enhanced reactivity pattern even on an inert support like silica. It is also worth mentioning that Ru nanochain system reported here showed a remarkably lower T_{100} value (by 40 °C) as compared to the Ru nanoparticles (2 nm)/CeO_2 which showed a full conversion at 180 °C as recently reported.[28]

4.3.7. Catalyst stability and time on stream experiments and spent catalyst analysis

Having demonstrated the superior catalytic activity of Ru nanochains, the stability of the catalyst was tested. The catalyst Ru nanochains/CeO_2 was subjected to time on stream (TOS) study at 140 °C (full conversion

temperature) for 8 h. The nanochains were found to be exceptionally stable under these conditions (See Figure 4.6).
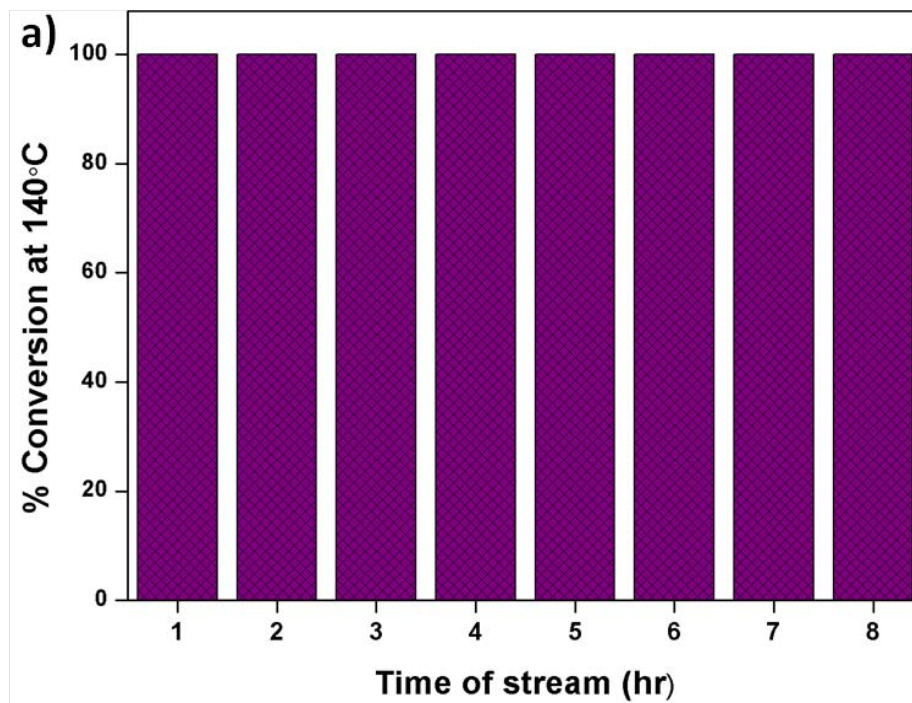
Figure 4.6: TOS of Ru Nanochains/CeO$_2$ after first cycle at temperature of full conversion.

Also the recyclability test done on nanochains did not show any variation up to four cycles demonstrating a stable and sustainable catalytic activity. Such stable activity was observed for Ru nanochains supported on TiO$_2$ also as shown in Figure 4.7.
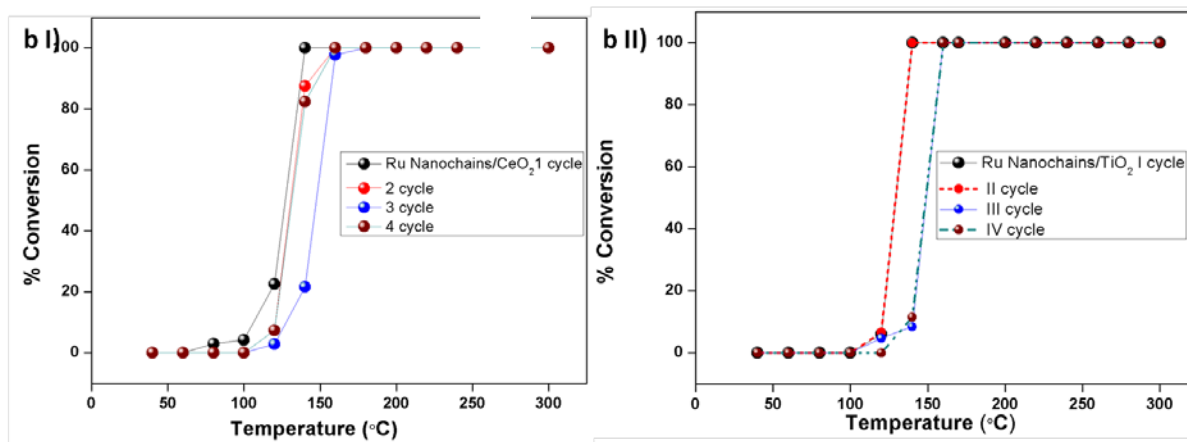
Figure 4.7: I) Stability of the Ru nanochains/CeO$_2$ and II) Ru nanochains/TiO$_2$ catalyst for four cycles.

The catalytic stability test for Ru spheres ($\sim$ 6 nm) supported on TiO_2 was also done and the results showed a clear contrast from that of nanochains. The onset and temperature of full conversion of Ru spheres ($\sim$ 6 nm)/TiO_2 were found to shift to higher temperatures during each cycle reaching a value of 170 °C and 220 °C from 140 °C and 170 °C as shown in Figure 4.8.
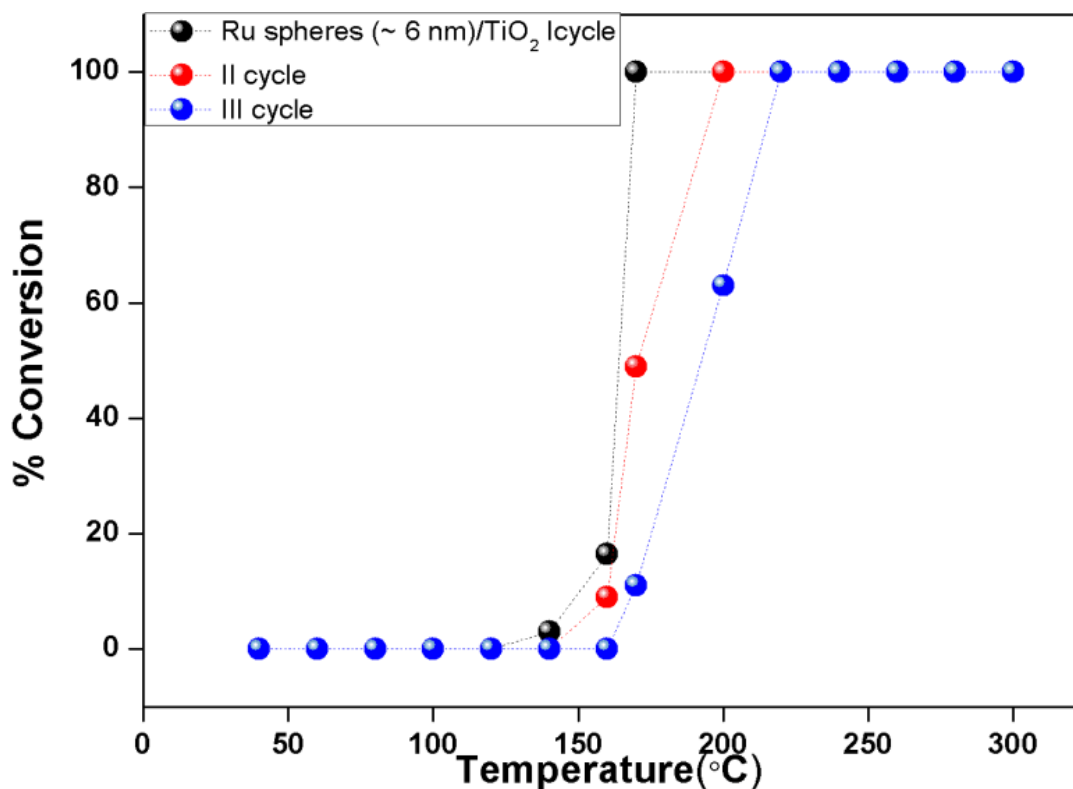
Figure 4.8: The CO oxidation plot for Ru spheres ($\sim$ 6 nm)/TiO_2) upto three cycles of CO oxidation.

To understand this slump in activity the electron microscopy of the spent Ru spheres ($\sim$ 6 nm)/TiO_2 catalyst was carried out. From the TEM image (Figure 4.9) the particle size obtained was $\sim$ 15 nm which indicated a clear case of sintering. Sintering of nanoparticles is major cause of catalyst deactivation.[29] On the other hand the spent supported Ru nanochain catalysts showed intact interconnected chain morphology even after four cycles of CO oxidation and the inset shows the F_{2g} vibrational mode of the cubic fluorite ceria. Such interconnected extended nanochain structures are not susceptible to sintering and can be active towards a chemical reaction due to the abundance of under coordinated sites.[30-31]
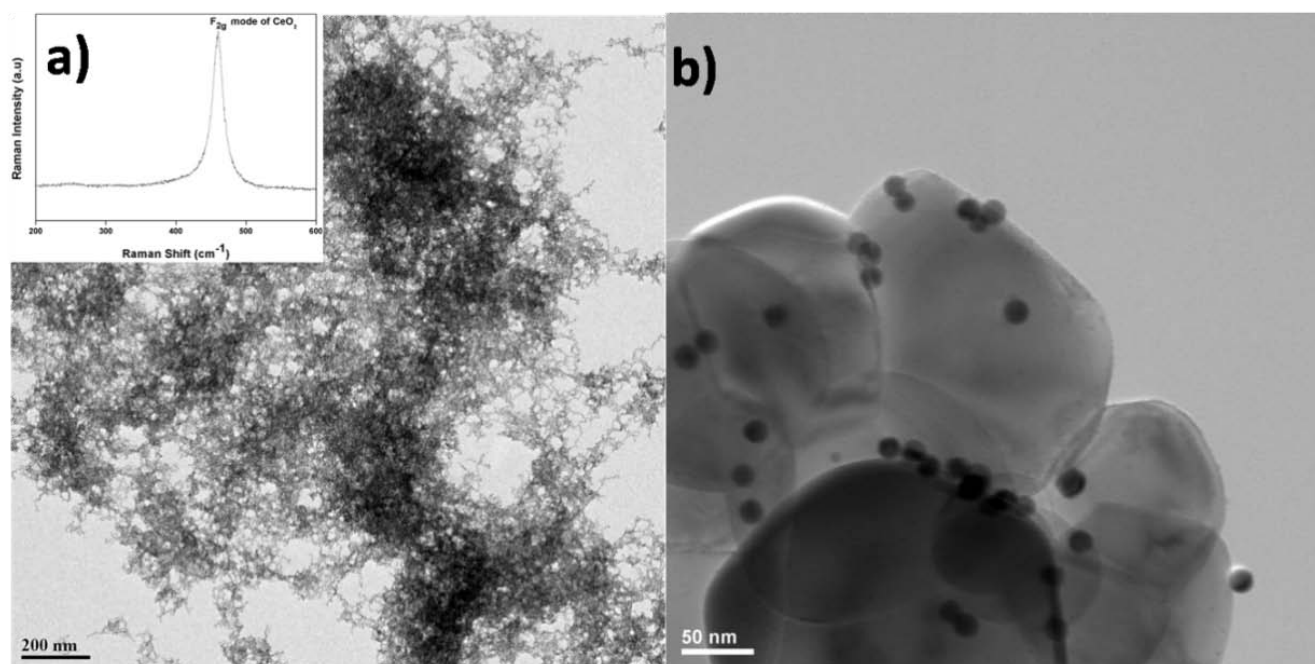
Figure 4.9: The TEM image a) showing the morphology of the spent catalyst supported on ceria, the inset shows the F_{2g} vibrational mode of the cubic fluorite CeO_2 and b) the spent catalyst which shows the increase in particle size after reaction.

4.4. Conclusions

In summary, Ru nanochain was synthesized in aqueous medium and at relatively mild conditions with CTAB as the capping agent using a seed mediated protocol. DLS measurements clearly showed spontaneous evolution of Ru seeds to nanochains. A surfactant induced self assembly is proposed to be the mechanism for nanochain formation. On three different supports studied, the Ru nanochains were found to show enhanced catalytic activity towards CO oxidation when compared to Ru nano seeds (~ 3.5 nm) and Ru spheres (~ 6 nm). Thus Ru nanochains exhibited best properties from two world's viz high percentage of under coordinated atoms from "nano" and stability from the "micro" regimes.

4.5. References

(1)   Petit, C.; Russier, V.; Pileni, M. P. *J. Phys Chem B,* **2003**, *107*, 10333.

(2)   Favier, F.; Walter, E. C.; Zach, M. P.; Benter, T.; Penner, R. M. *Science,* **2001**, *293*, 2227.

(3)   Tang, Z.; Kotov, N. A. *Adv Mater,* **2005**, *17*, 951.

(4)   Shiers, M. J.; Leech, R.; Carmalt, C. J.; Parkin, I. P.; Kenyon, A. J. *Adv Mater,* **2012**, *24*, 5227.

(5)   Polavarapu, L.; Xu, Q.-H. *Nanotechnology,* **2008**, *19*, 075601.

(6)   Feng, C.; Guo, L.; Shen, Z.; Gong, J.; Li, X.-Y.; Liu, C.; Yang, S. *Solid State Sci,* **2008**, *10*, 1327.

(7)   Chakrapani, K.; Sampath, S. *Chem Commun,* **2014**, *50*, 3061.

(8)   Sathe, B. R.; Balan, B. K.; Pillai, V. K. *Energy Environ Sci,* **2011**, *4*, 1029.

(9)   Pan, C.; Pelzer, K.; Philippot, K.; Chaudret, B.; Dassenoy, F.; Lecante, P.; Casanove, M.-J. *J Am Chem Soc,* **2001**, *123*, 7584.

(10)   Liu, K.; Wang, A.; Zhang, T. *ACS Catal,* **2012**, *2*, 1165.

(11)   Su, F.; Lv, L.; Lee, F. Y.; Liu, T.; Cooper, A. I.; Zhao, X. S. *J Am Chem Soc,* **2007**, *129*, 14213.

(12)   Joo, S. H.; Park, J. Y.; Renzas, J. R.; Butcher, D. R.; Huang, W.; Somorjai, G. A. *Nano Lett,* **2010**, *10*, 2709.

(13)   Watt, J.; Yu, C.; Chang, S. L. Y.; Cheong, S.; Tilley, R. D. *J Am Chem Soc ,***2012**, *135*, 606.

(14)   Yin, A.-X.; Liu, W.-C.; Ke, J.; Zhu, W.; Gu, J.; Zhang, Y.-W.; Yan, C.-H. *J Am Chem Soc,* **2012**, *134*, 20479.

(15)   Yang, J.; Lee, J. Y.; Deivaraj, T. C.; Too, H.-P. *J Colloid Interf Sci,* **2004**, *271*, 308.

(16)   Lu, F.; Liu, J.; Xu, J. *Mater Chem Phys,* **2008**, *108*, 369.

(17)   Chin, S. Y.; Alexeev, O. S.; Amiridis, M. D. *Appl Catal A,* **2005**, *286*, 157.

(18)   Zhang, B.; Zhang, C.; He, H.; Yu, Y.; Wang, L.; Zhang, J. *Chem Mater,* **2010**, *22*, 4056.

(19)   Chakrapani, K.; Sampath, S. *Chem Commun,* **2013**, *49*, 6173.

(20)   Yang, Y.; Nogami, M.; Shi, J.; Chen, H.; Ma, G.; Tang, S. *Appl Phys Lett,* **2006**, *88*.

(21)   Lin, S.; Li, M.; Dujardin, E.; Girard, C.; Mann, S. *Adv Mater,* **2005**, *17*, 2553.

(22)   Polavarapu, L.; Xu, Q.-H. *Langmuir,* **2008**, *24*, 10608.

(23)   Lu, X.; Liu, Q.; Huo, G.; Liang, G.; Sun, Q.; Song, X. *Colloids and Surf A,* **2012**, *407*, 23.

(24)   Schubert, M. M.; Hackenberg, S.; van Veen, A. C.; Muhler, M.; Plzak, V.; Behm, R. J. *J Catal,* **2001**, *197*, 113.

(25)   Li, D.; Ichikuni, N.; Shimazu, S.; Uematsu, T. *Appl Catal A,* **1998**, *172*, 351.

(26)   Kusada, K.; Kobayashi, H.; Yamamoto, T.; Matsumura, S.; Sumi, N.; Sato, K.; Nagaoka, K.; Kubota, Y.; Kitagawa, H. *J Am Chem Soc,* **2013**, *135*, 5493.

(27)   Qadir, K.; Joo, S. H.; Mun, B. S.; Butcher, D. R.; Renzas, J. R.; Aksoy, F.; Liu, Z.; Somorjai, G. A.; Park, J. Y. *Nano Lett,* **2012**, *12*, 5761.

(28)   Satsuma, A.; Yanagihara, M.; Ohyama, J.; Shimizu, K. *Catal Today,* **2013**, *201*, 62.

(29)   Bartholomew, C. H. *Appl Catal A ,* **2001**, *212*, 17.

(30)   Chen, X.; Xie, J.; Hu, J.; Feng, X.; Li, A. *J Phys D,* **2010**, *43*, 115403.

(31)   Zheng, J.-N.; Zhang, M.; Li, F.-F.; Li, S.-S.; Wang, A.-J.;.*Electrochimica Acta,* **2014**, *130*, 446.

Chapter-5

Summary and Conclusions

The elucidation of active sites is attempted on model nanoparticle surfaces. The choice of nanoparticles with specific morphology helps to bridge the material gap between the real world catalysts and UHV single crystal surfaces extensively employed for structure versus activity correlations. In this thesis an attempt for the determination of active sites in heterogeneous catalysis has been made. Inspired from single crystal and theoretical studies, which showed that stepped surfaces have different chemical reactivity relative to flat surfaces, attempts were adopted to synthesize metal nanoparticles with specific structure and which exposes sites of under coordination. The nanoparticles synthesized were trisoctahedral Au using a reported method which exposes {331}/{221} facets which carries {110} step atoms, Pd concave cubes and nanoflowers which is bound by {310} and {311} high index facets, and Ru nanochains which were found to have grooves and corrugated surfaces. The structure activity correlations were made using these nanoparticles on reactions which are metal specific. These structured nanoparticles were more active when compared to their low index counterparts. The thesis opens up some preliminary observations for the explanation of the hypothesis of active sites on nanoparticle surfaces.

Chapter-1*:* The chapter gives an introduction to nanocatalysis, morphologically controlled nanoparticles, surface structure, low index and high index facets, structure-sensitivity or facet dependent chemical activity on single crystal surfaces by UHV surface science studies and on different nanoparticles surfaces viz low index and high index structures and theoretical background for structure sensitivity. This chapter also discusses the analytical methods for the characterization of catalyst and tools used for analyzing a chemical reaction.

Chapter-2: This chapter deals with oxidation catalysis by large trioctahedral Au nanoparticles, wherein the role of step atoms, interfaces and confinement effects have been probed. To understand the origin of catalysis by gold and to probe the role of defects and interfaces, CO oxidation were carried out on supported trisoctahedral gold nanoparticles and on the inverse catalyst system. The sizes of these particles which are between 45 nm and 110 nm, are well beyond the quantum size regime and well above the optimum size range where gold is considered to be catalytically active. The periodic steps sites in contact with oxide support interface were able to promote the reaction. In the later part, the effect of confining these structured nanoparticles inside porous silica

was probed. As envisaged, a synthesis strategy is reported for encapsulating high index faceted trisoctahedral Au nanoparticles inside porous silica to preserve nanoparticle size by preventing sintering. Further, to probe the role of interfaces an active metal oxide junction was created by decorating trisoctahedral (TOH) Au nanoparticle with nano oxides before silica encapsulation. The activity of these catalysts was tested for CO oxidation reaction. The reaction was found to be facile on these encapsulated large structured Au nanoparticles showing appreciable activity at room temperature compared to non encapsulated counter parts. Apart from preventing sintering, the improved activity is demonstrated due to the retention of morphology and thereby the active centers due to encapsulation.

Chapter-3*:* This chapter describes the synthesis of high index faceted Pd concave cubes and nanoflowers using a seed mediated procedure at room temperature and in aqueous medium. The systematic evolution of a spherical seed to cube and then to concave cubes and nanoflowers were achieved by changing the surfactants used in the synthesis. A growth mechanism was proposed for the same. The structure sensitive chemical activity by these Pd nanostructures was proved for coupling and CO oxidation reaction. It was observed that these high index faceted nanostructures were found to be more active when compared to their low index counterparts. This enhanced activity can be attributed to the presence of large number of under coordinated atoms on high index faceted nanostructures. Moreover we observed that larger nanoparticles were thermally stable under CO oxidation conditions which make it more efficient relative to smaller nanoparticles.

Chapter-4: This chapter explains a surfactant assisted formation of Ru nanochains in aqueous medium and in mild synthesis conditions. The highlight of this chapter is the synthesis as the methods adopted till now for the making of hcp Ru crystals with morphology control has been energy intensive. These nanochains were synthesized using a seed mediated protocol where spherical nanoparticles serve as the seeds; a surfactant assisted self assembly of such seeds to form chain like morphology has been proposed. A detailed TEM analysis showed these nanostructures to expose corrugations and grooves which may be bound by atoms of under co-ordinations. This was proved by reactivity studies where supported Ru nanostructures were found to catalyse

CO oxidation reaction with a lower onset temperature and full conversion temperature when compared to spherical particles of ~ 3.5 nm and 6 nm and conventional impregnated catalyst.

List of Publications

1) S. Sreedhala, V. Sudheesh Kumar and C. P. Vinod, *Catalysis Today*, 2015, 244, 177-183.

2) S. Sreedhala, V. Sudheesh Kumar and C. P. Vinod, *Nanoscale,* 2014, 6, 7496-7502.

3) S. Sreedhala, C. P. Vinod*, Chemical Communications*, 2015, 51, 10178-10181.

4) S. Sreedhala, V. Sudheesh Kumar and C. P. Vinod, *Journal of Catalysis*, 2016, 337, 138-144.

5) S.Sreedhala, Sruthi Maheshwari, Betsy K.J, C. P. Vinod*, Applied catalysis A*, 2016, 524, 1-7.

6) D. Mullangi, S. Nandi, S. Shalini**,** S. Sreedhala , C. P. Vinod, R .Vaidhyanathan, *Scientific Reports* **5**, Article number: 10876 (2015) doi:10.1038/srep10.

Appendix

1. Calculation of turn over Frequency for Suzuki and Heck Coupling reactions on Pd nanostrutures

The efficiency of the catalyst was evaluated by computing TOF, where TOF can be defined as the iodobenzene conversion per surface Pd atom per second as described in the literature.

Calculation of the total number of Pd atoms in a Pd nanocube enclosed by {100} facets, and the total number of Pd atoms on the surface

1. Conventional nanocubes enclosed by {100} facets

a. Number of Pd atoms in a nanocube

The edge length of a Pd nanocube is approximately 31 nm. Its volume is $(31 \text{ nm})^3 = 2.97 \times 10^4 \text{ nm}^3$. Pd occupies a face centered cubic structure with a lattice constant of 0.389 nm. The volume of a unit cell is $(0.389 \text{ nm})^3 = 0.059 \text{ nm}^3$. Each unit cell contains four Pd atoms.

Therefore the total number of Pd atoms in a single Pd nanocube is $(2.97 \times 10^4 \text{ nm}^3/0.059 \text{ nm}^3) \times 4 = 2.01 \times 10^6 \text{ nm}^3$

b. Number of Pd atoms on the surface of a nanocube

A Pd nanocube has 6 {100} facets. The total surface area is $(31 \text{ nm})^2 \times 6 = 5.76 \times 10^3 \text{ nm}^2$. Each two-dimensional unit cell on the {100} facets contains two Pd atoms, and the area of this unit cell is $(0.39 \text{ nm})^2 = 0.15 \text{ nm}^2$. The total number of Pd atoms on the surface of a single nanocube is $(5.76 \times 10^3 \text{ nm}^2 / 0.15 \text{ nm}^2) \times 2 = 0.76 \times 10^5$.

c. Total number of Pd atoms on the surface of nanocubes used in the reaction

The total number of Pd atoms in the catalyst is $(10^{-4} \text{ g}) / (106.42 \text{ g/mol}) \times (6.02 \times 10^{23} \text{ g/mol})$

= 5.66×10^{17}. The number of Pd nanocubes involved in the catalytic reaction is $(5.66 \times 10^{17}) / (2.01 \times 10^6)$ = 2.78×10^{11}. The total number of Pd atoms on the surface of Pd nanocubes used in the catalytic reaction is 2.78 x 10^{11} x 0.76 x 10^5= 2.11 x 10^{16} Pd atoms

2.11 x 10^{16} Pd atoms = 0.35 x 10^{-4}m moles of Pd,

TOF can be calculated using this value.

TOF= %. Conversion x mol (substrate) / mol (catalyst) x time (sec), For example

For Palladium Nanocube

TOF=48 x 1 mmol / 0.35 x 10^{-4} mmoles X 3600 (sec)

$= 3.8$ x 10^2 s^{-1}

2. Concave nanocubes enclosed by {310} facets

a. Volume of a single concave nanocube {Pd concave cube (~ 23 nm)

The Pd concave nanocube has an average edge length of 23 nm

The volume of a cube = $(23 \text{ nm})^3$=1.21 x 10^4 nm^3

The volume of a square pyramid is 1/3 a^2 h, = $1/3 \times (23 \text{ nm})^2 \times$ 1/3 x 23/2 = 0.675 x 10^3 nm^3 (here h = edge length /2 and 1/3 term comes from {310} step atom density.

The volume of a concave nanocube is (1.21 x 10^4 nm^3- 6 x 0.675 x 10^3 nm^3) = 0.805 x 10^4 nm^3.

The number of Pd atoms in a single Pd concave nanocube = (0.805 x 10^4 nm^3/ 0.0589) x 4 = 5.4 x 10^5

b. Number of Pd atoms on the surface of a concave nanocube (~ 23 nm)

The atomic density of {310} planes is 1/3of that of {100} planes. Considering a cube of 23 nm in edge length, the total surface area of the cube is 6a^2= $(23 \text{ nm})^2 \times 6$ = 3.17 x 10^3 nm^2.

The total number of Pd atoms on the {310} facets of a single concave nanocube = total surface area of the nanocube/surface area of single fcc Pd lattice x 2 x 1/3

(3.17 x 10^3 nm^2/0.151) x 2 x 1/3=1.39 x 10^4 Pd atoms

c. Number of surface Pd atoms/particle/volume of the concave nanocube

For a 23 nm concave nanocube the number of surface Pd atoms/particle/volume of the concave nanocube = 1.39 x 10^4/0.805 x 10^4 nm^3 = 1.72 Pd atoms /nm^3

d. Total number of Pd atoms on the surface of concave nanocubes in the reaction

The total number of Pd atoms in the catalytic reaction is 5.66×10^{17}. The number of Pd concave nanocubes in the catalytic reaction is calculated as follows:

The total number of Pd atoms in 0.1 mg of the catalyst = (10^{-4} g/106.42 g/mol (molar mass of Pd)) x 6.02 x 10^{23} g/mol = 5.66×10^{17} Pd atoms.

Total number of Pd concave nanocubes involved in the catalytic reaction = 5.66×10^{17} Pd atoms /5.4 x 10^5 = 1.04 x 10^{12}

The total number of Pd atoms on the surface of concave nanocubes in the catalytic reaction is Total number of Pd concave nanocubes x No of surface Pd atoms in a single concave nanocube = 1.04 x 10^{12} x 1.39 x 10^4 = 1.44 x 10^{16} Pd atoms = 0.239 x 10^{-4} mmoles.

By this value TOF can be calculated as mentioned above.

95 x 1 mmol /0.239 x 10^{-4} mmoles x 3600 s = 11 x 10^2 s^{-1}

3. Calculation for the Number of step atoms for Palladium concave nanocube of edge length 23 nm

Edge length=23 nm

Pd-Pd bond distance=0.27 nm

No. of Palladium atoms along the edge=23/0.27 nm=85 atoms

{310} facets consist of 3 atom wide {100} terrace followed by monoatomic {111} step.

So no. of step atoms along a edge of length 23 nm=21step atoms

Each face of the concave cube has 4 edges and there are total of 6 faces

So the number of step atoms along the edges on the face of the concave nanocube per particle = 21 x 4 x 6 = 504

Catalyst	Conversion[a] (%)	TOF (s⁻¹)	Conversion[b] (%)	TOF (s⁻¹)
Pd Concave cube (23 nm)	95	22.5	76	18
Pd Concave cube (37 nm)	96	22.7	80	18.9
Pd Concave cube (47 nm)	97	23	84	19.9
Pd nano Flower (100 nm)	99	23.5	85	20.1
a – Suzuki Coupling				
b – Heck Coupling				

Table 3.2.: Table showing the % conversion and TOF value taking the whole Pd catalyst into account: for Suzuki coupling and Heck coupling done with different palladium catalysts.

The amount of Pd in 10 mM H_2PdCl_4 solution is 0.106 g of Pd in 100 mL,The amount added for synthesising nanoflowers and Concave nanocubes is about 125 μL which contains around 0.125 mg of Pd if complete seperation can be achieved.

The calculated amount of Pd after the final growth step in our catalyst is around 0.125 mg, if complete separation is achieved.This was then dispersed in ethanol to make it reactant miscible to 100 μL and was added to reactant mixture.

So amount of Pd is 0.125 mg which is used for reaction

1 mole of Pd = 106 g

0.125 mg of Palladium = 1 X 0.125/106 x 1000

$$= 11.7 \text{ x } 10^{-7} \text{moles} = 11.7 \text{ x } 10^{-4} \text{mmoles.}$$

So in case of Pd nanoflowers, for Suzuki reaction, TOF = 99 x 1 mmol/11.7 x 10^{-4} mmol x 3600 (sec) = 23.5 s^{-1}.

2) CO oxidation

Calculation of Turnover frequency of Pd nanostructures

Calculation of total number of surface Pd atoms in the reaction for a concave cube

1. Volume of a single Pd concave nanocube (37 nm)

The Pd concave nanocube has an average edge length of 37 nm

The volume of a cube = $(37 \text{ nm})^3 = 5.06 \text{ x } 10^4 \text{ nm}^3$

The volume of a square pyramid is 1/3 a^2 h, = 1/3 $\times$ $(37 \text{ nm})^2 \times$ 1/3 x 37/2 = 2.81 x10^3 nm^3 (here h = edge length /2 and 1/3 term comes from {310} step atom density).

The volume of a concave nanocube is $(5.06 \text{ x } 10^4 \text{ nm}^3$- 6 x 2.81 x 10^3 nm$^3) = 3.38 \text{ x } 10^4$ nm^3.

The number of Pd atoms in a single Pd concave nanocube = $(3.38 \text{ x } 10^4$ nm^3/0.0589) x 4 = 22.9 x 10^5 Pd atoms (lattice parameter of Pd is 0.388 nm).

2. Number of Pd atoms on the surface of a concave nanocube

The atomic density of {310} planes is 1/3of that of {110} planes. Considering a cube of 37 nm in edge length, the total surface area of the cube is 6a^2 = $(37 \text{ nm})^2 \times 6 = 8.21 \text{ x } 10^3$ nm^2.

The total number of Pd atoms on the {310} facets of a single concave nanocube = total surface area of the nanocube/surface area of single fcc Pd lattice x 2 x 1/3

$(8.21 \text{ x } 10^3$ nm^2/0.151) x 2 x 1/3 = 3.62 x 10^4 Pd atoms

3. Total number of Pd atoms on the surface of concave nanocubes in the reaction

The total number of Pd atoms in the catalytic reaction is 5.66×10^{18}. The number of Pd Concave nanocubes in the catalytic reaction is calculated as follows:

The total number of Pd atoms in 100 mg of the catalyst with 1 wt% Pd loading = (10^{-3} g/106.42 g/mol (molar mass of Pd)) x 6.02 x 10^{23} g/mol = 5.66×10^{18} Pd atoms.

Total number of Pd concave nanocubes involved in the catalytic reaction = 5.66×10^{18} Pd atoms /22.9 x 10^{5} = 0.24 x 10^{13}

The total number of Pd atoms on the surface of concave nanocubes in the catalytic reaction = Total number of Pd concave nanocubes x No of surface Pd atoms in a single concave nanocube = 0.24 x 10^{13} x 3.62 x 10^{4} = 0.84 x 10^{18} Pd atoms = 0.116 x 10^{-3} mmoles.

Similarly for a cube and spherical particles the total number of surface Pd atoms can be calculated taking morphological factors into account.

The volume% of CO in gas feed is approximately 4 mL which corresponds to 0.178 mmoles.The ramping rate of the temperature is 2°/min and the reaction is kept at a particular temperature for 10 mins before injection to GC. So the reaction time is 10 mins = 600 secs

TOF @a particular temperature can be calculated

For example,

TOF @ 473 K for Pd concave cube (47 nm)/MgO can be calculated as follows

At 473 K, % conversion = 100%

Therefore TOF = 1 X 0.178 mmoles CO/0.116 x 10^{-3} mmoles of surface Pd atoms x 600 s

= 2.55 s^{-1}

Similarly the TOF for cubes and spherical particles of similar size can be calculated taking their morphology into account.

About the Author

Sreedhala S was born on 17th September, 1987 in Palakkad, Kerala. After completing her secondary school in 2005, she started her Bachelors in Pure Chemistry in Union Christian College Aluva, Kerala (2005-2008). Following her post graduation degree with Organic Chemistry specialization from School of Chemical Sciences, Mahatma Gandhi University, Kottayam, Kerala (2008-2010), she was awarded Junior Research Fellowship in 2011 by Council of Scientific and Industrial Research (CSIR). She then joined National Chemical Laboratory, Pune in August 2011 for her Ph D studies under the supervision of Dr. Vinod C. Prabhakaran, Catalysis and Inorganic Chemistry Division. Her research interests include synthesis of shape controlled nanoparticle and their potential application as nanocatalysts. Her thesis work describes the elucidation of active sites on structured nanoparticle surfaces which were used to catalyse chemical reactions of environmental and industrial importance.